UNIVERSITY OF OKLAHOMA

GRADUATE COLLEGE

CREATION OF HYPER-DOPED CRYSTALLINE TITANIA THIN FILMS BY THE KINETIC DOPING METHOD FOR SOLAR CELL ANODE MATERIAL

A DISSERTATION

SUBMITTED TO THE GRADUATE FACULTY

in partial fulfillment of the requirements for the

Degree of

DOCTOR OF PHILOSOPHY

By

ALLY FAIRMAN

Norman, Oklahoma

2022

CREATION OF HYPER-DOPED CRYSTALLINE TITANIA THIN FILMS BY THE KINETIC DOPING METHOD FOR SOLAR CELL ANODE MATERIAL

A DISSERTATION APPROVED FOR THE

DEPARTMENT OF CHEMISTRY AND BIOCHEMISTRY

BY THE COMMITTEE CONSISTING OF

Dr. Wai Tak Yip, Chair

Dr. Charles V. Rice

Dr. Ulrich H.E. Hansmann

Dr. Daniel T. Glatzhofer

Dr. Lloyd A. Bumm

© Copyright by ALLY FAIRMAN 2022

All Rights Reserved.

Table of Contents

List of Tables

List of Figures

Abstract

This work outlines the general process of kinetic doping and how its benefits have been expanded from silica-based applications to use in titania thin films. While this has potential for many applications, the utilization focused on in this work is as a novel approach to the fabrication of anode material in dye-sensitized solar cells (DSSCs).

Chapter 1 discusses the general pathways of the sol-gel process and various methods of guest molecule loading. This includes the kinetic doping method which will be utilized in this work. Chapter 2 will go into further detail on the research field of dye-sensitized solar cells (DSSCs) and how this work may be a benefit to the field. Chapter 3 is a record of the various materials, instrumentation, and methods utilized to accomplish the experiments in this work.

The main work of creating the hyper-doped TiO_2 thin films for utilization as a DSSC anode material is discussed in chapters 4-6. The general steps to accomplish the prototype DSSC based on our intended anode material are:

(i) to establish kinetic doping in TiO_2 thin films

(ii) to broaden the wavelength range of light absorbed by loading multiple dyes at once

(iii) to crystallize the amorphous dye-doped TiO_2 thin films while minimizing the damage to dye molecules caused by thermal degradation

(iv) to create and evaluated the performance of prototype DSSCs using the material established in the first three steps.

Chapter 4 will discuss the challenges and results of steps (i) and (ii), establishing the protocols for creating hyper-doped amorphous TiO_2 thin films and one-pot loading of multiple dyes. In

theory, since the hydrolysis and condensation chemistry taking place in silica sol-gels and titania sol-gels is inherently very similar, kinetic doping in titania sol-gels is expected to follow the same general pathway as silica sol-gels. However, since the titanium dioxide precursor is more reactive than the silicon dioxide precursor, kinetic doping in titania sol-gels will clearly not be identical to kinetic doping in silica sol-gels. Concentrations as high as 0.7 - 1.9 M in thin films from 120-250 nm thick are achieved for various dyes from a 1 mM loading solution. Up to four dyes are loaded in a single-step loading process, resulting in an absorption range from 300 – 700 nm.

Step (iii), crystallization of the amorphous dye-doped TiO_2 thin films is also important. The amorphous thin films may work in a prototype but would almost certainly be more effective in a crystalline form. As the traditional crystallization process of heating at high temperatures is expected to degrade the loaded organic dye molecules, a lower temperature crystallization process will likely be needed. Chapter 5 describes this low-temperature method of TiO_2 thin film crystallization, and the challenges associated with establishing the protocol. The final protocol results in an 85% dye retention rate, which allows the advantage of kinetic doping to be manifested in the final crystallized thin film. Multilayer thin films are created and undergo crystal transformation in a single step, indicating a high degree of tunability for the final thickness of a DSSC anode made from this material.

The final step, (iv), the creation of a prototype, is discussed in Chapter 6. Creating a prototype is a fundamental part of establishing whether these hyper-doped TiO_2 thin films have the potential to produce high efficiency anode materials for DSSC. The prototype power conversion efficiency achieved ranges in efficiency from 0.001-0.008%, which is on par with the literature efficiency of DSSCs utilizing analogous dyes and redox electrolyte solution. It is even within an

order of magnitude of DSSCs that use the same analogous electrolyte and high-efficiency dyes. Avenues for further improvement to the prototype DSSCs are also discussed.

1. Sol-gel Chemistry

1.1 The Sol-Gel Process

Sol-gel reactions are particularly useful because they allow us to create glass or other oxide materials at room temperature. The first silica sol-gels (for the creation of glass at room temperature) were created in the mid-19th century, and the research field expanded over the following years to include many varieties of oxide materials.[1] The "sol-gel" reaction is named directly after the two main stages – the first is initial solution of various reagents, one of which is an $M(OR)_4$ precursor. After the solution is allowed to age and undergo gelation, colloidal particles continue to react and form a three-dimensional network and a solid gel.[2, 3]

The aging process allows the sol-gel to undergo a series of hydrolysis and condensation steps.

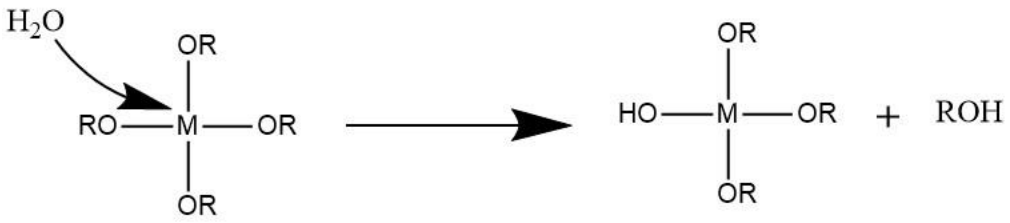

Figure 1.1 Hydrolysis, first step of the sol-gel reaction

The hydrolysis step prepares the alkoxide precursor to undergo condensation, which allows the precursor molecules to build a polymeric chain, fiber, or branched network.

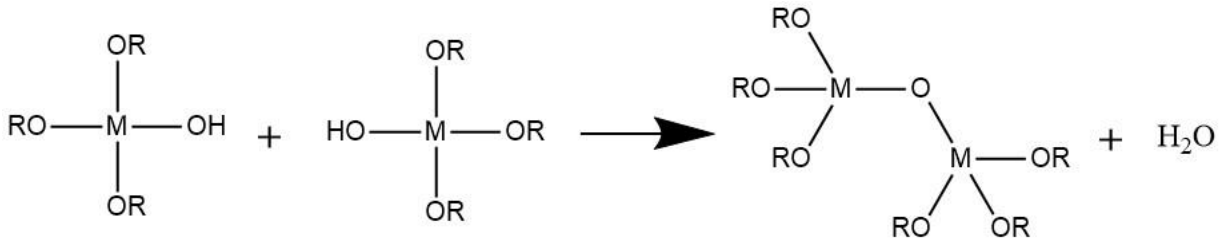

Figure 1.2 Condensation, second step of the sol-gel reaction

These steps repeat continuously during the gelation process, creating the suspension of three-dimensional polymeric networks that increase the viscosity of the solution until it eventually becomes a gel.

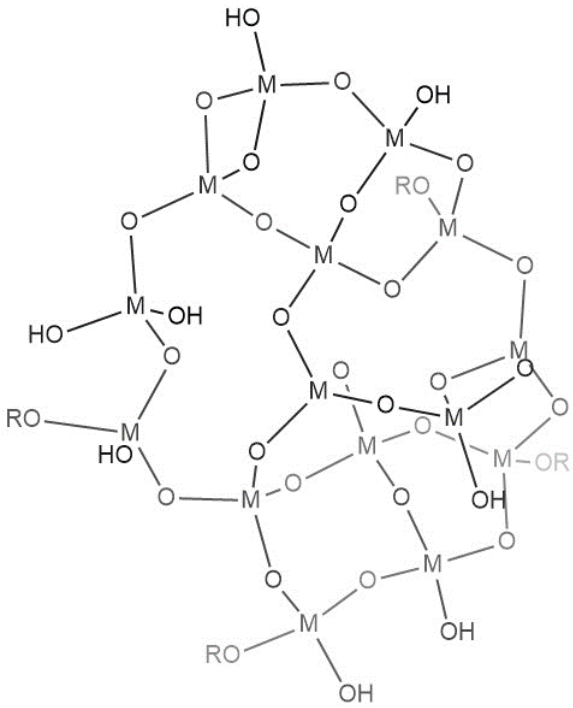

Figure 1.3 Representation of a 3D polymeric network produced by sol-gel chemistry

If the sol-gel is allowed to continue aging indefinitely, it will eventually form a solid monolith. It can also be utilized after an appropriate aging time to create a final thin film material or aggregation of nanoparticles. The final material is typically amorphous in nature as illustrated in Figure 1.3, where the network is random and disordered. This random network produces open pores and channels throughout the final amorphous material, which allows guest molecule trapping within the metal oxide matrix.

The sol-gel reaction can be catalyzed by addition of either an acid or a base. Basic catalysis of the sol-gel reaction is famously known as the Stöber process. In this form, the condensation step

has a much faster rate of reaction than the hydrolysis step, which causes the polymeric network to grow into multiple branched particles that do not entangle with the other branched particles, remaining distinct in both the sol-gel and the final dried material. Therefore, the Stöber process is primarily used for metal oxide nanoparticle formation. The general reaction pathway for the Stöber process is shown in Figure 1.4. [4-7]

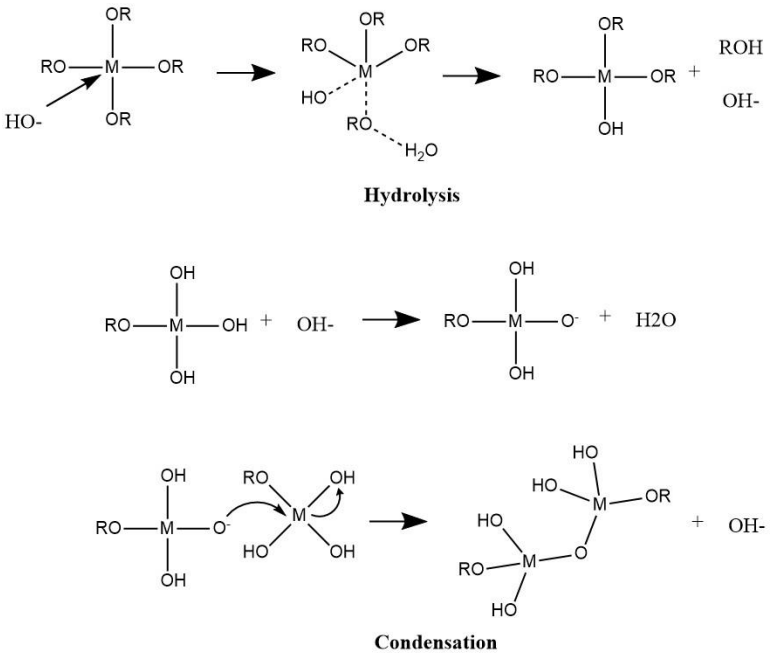

Figure 1.4 General base-catalyzed sol-gel reaction pathway

When the sol-gel solution is catalyzed by acid, the hydrolysis and condensation steps take on the general reaction pathway displayed in Figure 1.5. In the acid catalyzed reaction, these steps are slower than in the base-catalyzed reaction, promoting the large, interconnected branched polymer networks instead of individual aggregates. The final product of an acid-catalyzed sol-gel reaction is an interconnected metal oxide network with pores and channels throughout it.[6, 8, 9] The sol-gels created in this work will utilize an acidic catalyst.

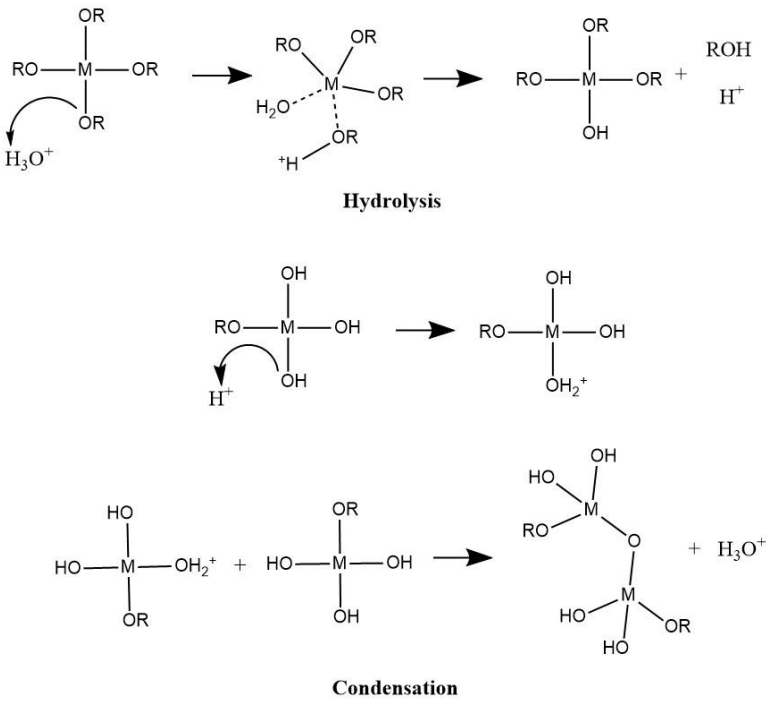

Figure 1.5 General acid catalyzed sol-gel reaction pathway

The second main categorization of sol-gels is the differentiation between alcogels and hydrogels. Alcogels are sol-gels with an alcohol as the primary solvent, used to allow both the water and metal alkoxide to dissolve and react. Hydrogels are less common, but more biocompatible. Hydrogels are based on using water as the primary solvent.[9-13] For this work, all sol-gels created will be done using alcogel solutions.

The final categorization of sol-gels has more to do with the method of removing the residual solvent and drying the sol-gel to its final stage. Either the sol-gel will be allowed to dry naturally through evaporation, creating a xerogel, or it will be forced through a supercritical drying process, creating an aerogel. Aerogels show a lower degree of shrinkage and pore collapse in the amorphous network, but are more difficult to produce.[3, 9] The thin films created from sol-gels in this work will be treated through a xerogel process.

1.2 Introducing Dopant Molecules to the Sol-Gel Matrix

Sol-gel materials formed by any of these methods have proven to be incredibly useful due to the tunability of their material properties. The reactions generally take place under mild STP conditions. The materials formed are largely chemically inert, thermally stable, mechanically strong, and relatively immune to photodegradation. Many of the properties of the polymer matrix can be tuned by adjusting the composition of the reagent solution and processing, but sol-gel materials can also be functionalized by encapsulating guest molecules.[14-16] One of the first experiments concerning this was by Dickey in 1949 using a sodium silicate based sol-gel to encapsulate four different dyes from solution.[17] Guest molecule loading was further explored by Avnir et al. in 1984, when the lab first managed to load Rhodamine 6G into a monolithic sol-gel matrix.[18] Successful dye loading subsequently expanded to functionalizing monoliths with enzymes. Enzyme-functionalized sol-gel materials allowed low-molecular weight substrates to enter the porous polymer matrix and react with the trapped, still-active enzyme. Once the reaction took place, the product could then diffuse back through the matrix into solution.[19-21]

It is generally accepted that the guest molecules are contained within the pores of the polymer matrix, which means that the loading of useful guest molecules is highly dependent on being able to tune the size of the pores.[22-26] Conditions like the pH, precursor, ratio of initial reactants, the presence of an additional guest molecule or the time the sol-gel has been aged all affect the pore size, allowing researchers to design sol-gels to produce materials with pore sizes from 1 nm – 200 nm[16, 27-30].[15, 26-29] In pores that are sufficiently larger than the loaded guest molecules, the guest molecules display similar functional behavior to being free in solution. If the pores are smaller, some functions of the guest molecule may be inhibited by the restricted space of the pore[31-35]. In some cases, the functionality of the guest molecule is modified when loaded into the

amorphous metal oxide material. In these cases, it is theorized that this modification of properties may result from being physically embedded in the pore wall, hydrogen bonding interactions, or electrostatic interactions between the guest molecule and the pore wall.[24, 30, 33-39] In sol-gel materials where the pore size is significantly larger than the guest molecules, properties of the solvent like viscosity, polarity, pH, and composition play the most critical role in determining the environment of the guest molecule.[36-42]

Loading guest molecules in a sol-gel matrix is beneficial because it provides the guest molecule with a form of chemical and thermal stability. The matrix protects the guest molecule from harsh conditions that they would ordinarily be unable to tolerate in free solution.[3, 21, 43-47] Assuming that the guest molecules are firmly lodged in the pore channels, the functionalized matrix will also be easy to reuse.

1.3 Methods For Loading Guest Molecules Within Sol-Gel Materials

1.3.1 Pre-Doping

As the name implies, pre-doping a sol-gel matrix involves adding the guest molecule to the initial liquid reactant solution.[18, 48-50] Since the guest molecule is added to the initial reactant solution, the concentration is limited by the fact that the concentration cannot be so high that it will disrupt the sol-gel hydrolysis and condensation reactions. The guest molecules must also be compatible with the solvent used in the sol-gel reaction. For example, one ought not pre-dope an alcogel solution with an enzyme and expect the enzyme to remain functional. Even with those restrictions, this method generally allows for a higher concentration of dopant than the second traditional method and is therefore more popular in applications where high dopant concentration is essential.[51] It is worth pointing out that a sol-gel material remains amorphous in the pre-doping method. As most crystallization process require thermal treatment, crystallization of this material

can result in the degradation of the encapsulated guest molecules.[52, 53] With the limitations of pre-doping (solvent compatibility, amorphous final form) preventing the creation of specific loaded metal oxide materials, it is not surprising that there is a second, equally popular method of guest molecule loading.

1.3.2 Post-Doping

Post-doping is the second traditional method of loading guest molecules to sol-gel derived oxide materials. This method of loading guest molecules does not include the dopant in the initial reactant solution. The material is fully processed into its final form (amorphous film, crystallized film, crystalline nanoparticles, etc.) prior to its introduction to a guest molecule loading solution.[54-56] This method assures that guest molecules will not be affected by either the solvent compatibility or degradation during crystallization processes.

While post-doping allows for greater variety in the guest molecules and in the structure of the oxide material matrix, there is an even more stringent limit to the concentration of dopant molecules than is seen in pre-doping. Only molecules that can adsorb to the surface or diffuse in through any remaining pores of the material created will stay in the matrix. This results in even lower concentrations across the final material. A second issue with post-doping is that any pore channels which contain guest molecules have to be large enough for the guest molecules to seep in to the material, which means the guest molecules are also more prone to leaching out relative to pre doping.[57]

1.3.3 Kinetic Doping

In recent years, a dynamic alternative method of loading guest molecules was developed by Dr. Yip's lab at the University of Oklahoma. This process has been named "Kinetic Doping"

because it takes advantage of the reaction kinetics of the sol-gel process to increase the effective loading of guest molecules in a thin film. Because the increased guest molecule loading from this method is limited to a thin layer of material, this method is of limited use outside of thin film processes. When loading guest molecules in a thin film, much higher concentrations can be achieved than by either of the other traditional methods.

The general process of kinetic doping starts out very similar to the post-doping process. There is no dopant added to the original reactant solution, which is aged before processing. A thin film without the guest molecule is created on substrate through either a spin-coating or dip coating method. This is the point where the process begins to differ from post-doping. After just a short post coat delay to allow the film to react sufficiently to be mechanically stable on the substrate, the film is introduced to an aqueous guest molecule loading solution. Unlike post-doping, this film is still mutable and undergoing hydrolysis and condensation continuously. Since the film has not yet fully condensed, the guest molecules are drawn into the pores of the evolving matrix while the reaction continues. This results in trapping high concentrations of guest molecules within the matrix as the pores are forming. Once the film is removed and dried, the film condenses fully, becoming a stable, optically clear thin film. Concentration of dye molecules trapped within an amorphous silica sol-gel matrix utilizing this method could reach as high as 1.1 M from doping in a 1.0 mM aqueous dye solution for an hour, compared to literature pre-doping concentrations of around 0.01 M.[58, 59] However, kinetic doping, like pre-doping, results in guest molecules trapped in an amorphous sol-gel matrix.

1.4 The Goals for Kinetic Doping in Titania Sol-Gel Thin Films

Previous work with kinetic doping by members of the Yip lab at the University of Oklahoma has focused on introducing guest molecules into silica sol-gels from a tetraethyl orthosilicate

precursor.[21, 60-64] While great strides have been made in that direction and there is much left to achieve, more can be accomplished by further diversifying kinetic doping applications in other metal oxide sol-gel materials. For instance, a film comprised of a semiconductor material such as titanium dioxide would allow for applications in the area of electrochemistry.

One of those potential applications would be in the fabrication of dye-sensitized solar cells (DSSCs), which is the primary focus of this work using titania-based sol-gel materials. The motivation behind this work is based on the expectation that the hyper-doped films produced by kinetic doping will have the potential to impact two potential areas for improvement in the efficiency of the solar cells, the concentration of dye molecules in direct contact with the semiconducting anode material, and the optimal thickness of the anode material.[65, 66] In order to accomplish this, kinetic doping will first have to be achieved in TiO_2 thin films. To expand the potential utilization of these thin films, one-pot multiple dye loading will need to be established. The doped TiO_2 thin films will then need to be transformed into a crystalline form without losing the high dye loading advantage. Finally, prototype DSSCs will be created using anodes made from various numbers of layers of the doped, crystalline thin film material, to properly evaluate the potential of this material in future DSSC development.

1.5 References

1. Robinson, A. L., A Chemical Route to Advanced Ceramics: The secret to improving a ceramic material is to control its structure at very small length scales in an early stage of fabrication; chemistry may be the way to achieve this goal. (0036-8075 (Print)).

2. Kumar, A.; Yadav, N.; Bhatt, M.; Mishra, N.; Chaudhary, P.; Singh, R., Sol-Gel Derived Nanomaterials and It's Applications: A Review. *Research Journal of Chemical Sciences* **2015,** *5*, 1-6.

3. Ciriminna, R.; Fidalgo, A.; Pandarus, V.; Béland, F.; Ilharco, L. M.; Pagliaro, M., The Sol–Gel Route to Advanced Silica-Based Materials and Recent Applications. *Chemical Reviews* **2013,** *113* (8), 6592-6620.

4. Stöber, W.; Fink, A.; Bohn, E., Controlled growth of monodisperse silica spheres in the micron size range. *Journal of Colloid and Interface Science* **1968,** *26* (1), 62-69.

5. Livage, J.; Sanchez, C., Sol-gel chemistry. *Journal of Non-Crystalline Solids* **1992,** *145*, 11-19.

6. Hench, L. L.; West, J. K., The sol-gel process. *Chemical Reviews* **1990,** *90* (1), 33-72.

7. Ghimire, P. P.; Jaroniec, M., Renaissance of Stöber method for synthesis of colloidal particles: New developments and opportunities. *Journal of Colloid and Interface Science* **2021,** *584*, 838-865.

8. Buckley, A. M.; Greenblatt, M., THE SOL-GEL PREPARATION OF SILICA GELS. *Journal of Chemical Education* **1994,** *71*, 599-602.

9. C. Jefferey Brinker, G. W. S., *Sol-Gel Science: The Physics and Chemistry of Sol-Gel Processing*. ACADEMIC PRESS, INC: United States, 1990; p 908.

10. Avnir, D.; Kaufman, V. R., Alcohol is an unnecessary additive in the silicon alkoxide sol-gel process. *Journal of Non-Crystalline Solids* **1987,** *92* (1), 180-182.

11. Ferrer, M. L.; Monte, F.; Levy, D., A Novel and Simple Alcohol-Free Sol−Gel Route for Encapsulation of Labile Proteins. *Chemistry of Materials - CHEM MATER* **2002,** *14*.

12. Avnir, D.; Coradin, T.; Lev, O.; Livage, J., Recent bio-applications of sol–gel materials. *Journal of Materials Chemistry* **2006,** *16* (11), 1013-1030.

13. Khurana, B.; Gierlich, P.; Meindl, A.; Gomes-da-Silva, L. C.; Senge, M. O., Hydrogels: soft matters in photomedicine. *Photochemical & Photobiological Sciences* **2019,** *18* (11), 2613-2656.

14. Glaves, C. L.; Brinker, C. J.; Smith, D. M.; Davis, P. J., In situ pore structure studies of xerogel drying. *Chemistry of Materials* **1989,** *1* (1), 34-40.

15. Deshpande, R.; Hua, D.-W.; Smith, D. M.; Brinker, C. J., Pore structure evolution in silica gel during aging/drying. III. Effects of surface tension. *Journal of Non-Crystalline Solids* **1992,** *144*, 32-44.

16. Davis, P. J.; Deshpande, R.; Smith, D. M.; Brinker, C. J.; Assink, R. A., Pore structure evolution in silica gel during aging/drying. IV. Varying pore fluid pH. *Journal of Non-Crystalline Solids* **1994,** *167* (3), 295-306.

17. Dickey, F. H., The Preparation of Specific Adsorbents. *Proc Natl Acad Sci U S A* **1949,** *35* (5), 227-229.

18. Avnir, D.; Levy, D.; Reisfeld, R., The nature of the silica cage as reflected by spectral changes and enhanced photostability of trapped Rhodamine 6G. *The Journal of Physical Chemistry* **1984,** *88* (24), 5956-5959.

19. Venton, D. L.; Cheesman, K. L.; Chatterton, R. T.; Anderson, T. L., Entrapment of a highly specific antiprogesterone antiserum using polysiloxane copolymers. *Biochimica et Biophysica Acta (BBA) - General Subjects* **1984,** *797* (3), 343-347.

20. Glad, M.; Norrlöw, O.; Sellergren, B.; Siegbahn, N.; Mosbach, K., Use of silane monomers for molecular imprinting and enzyme entrapment in polysiloxane-coated porous silica. *Journal of Chromatography A* **1985,** *347*, 11-23.

21. Crosley, M. S.; Yip, W. T., Silica Sol–Gel Optical Biosensors: Ultrahigh Enzyme Loading Capacity on Thin Films via Kinetic Doping. *The Journal of Physical Chemistry B* **2017,** *121* (9), 2121-2126.

22. Pouxviel, J. C.; Dunn, B.; Zink, J. I., Fluorescence study of aluminosilicate sols and gels doped with hydroxy trisulfonated pyrene. *The Journal of Physical Chemistry* **1989,** *93* (5), 2134-2139.

23. Kaufman, V. R.; Avnir, D.; Pines-Rojanski, D.; Huppert, D., Water consumption during the early stages of the sol-gel tetramethylorthosilicate polymerization as probed by excited state proton transfer. *Journal of Non-Crystalline Solids* **1988,** *99* (2), 379-386.

24. Zhou, Y.; Yip, W. T., Balance between Coulombic Interactions and Physical Confinement in Silica Hydrogel Encapsulation. *The Journal of Physical Chemistry B* **2009,** *113* (17), 5720-5727.

25. Dunn, B.; Zink, J. I., Probes of Pore Environment and Molecule−Matrix Interactions in Sol−Gel Materials. *Chemistry of Materials* **1997,** *9* (11), 2280-2291.

26. Daiko, Y.; Kasuga, T.; Nogami, M., Pore size effect on proton transfer in sol–gel porous silica glasses. *Microporous and Mesoporous Materials* **2004,** *69* (3), 149-155.

27. Davis, P. J.; Jeffrey Brinker, C.; Smith, D. M.; Assink, R. A., Pore structure evolution in silica gel during aging/drying II. Effect of pore fluids. *Journal of Non-Crystalline Solids* **1992,** *142*, 197-207.

28. Davis, P. J.; Jeffrey Brinker, C.; Smith, D. M., Pore structure evolution in silica gel during aging/drying I. Temporal and thermal aging. *Journal of Non-Crystalline Solids* **1992,** *142*, 189-196.

29. Smith, D. M.; Deshpande, R.; Brinker, C. J.; Earl, W. L.; Ewing, B.; Davis, P. J., In-situ pore structure characterization during sol-gel synthesis of controlled porosity materials. *Catalysis Today* **1992,** *14* (2), 293-303.

30. Kato, M.; Sakai-Kato, K.; Toyo'Oka, T., Silica sol-gel monolithic materials and their use in a variety of applications. *J. sep. sci. (print)* **2005,** *28* (15), 1893-1908.

31. Dave, B. C.; Soyez, H.; Miller, J. M.; Dunn, B.; Valentine, J. S.; Zink, J. I., Synthesis of Protein-Doped Sol-Gel SiO2 Thin Films: Evidence for Rotational Mobility of Encapsulated Cytochrome c. *Chemistry of Materials* **1995,** *7* (8), 1431-1434.

32. Hüsing, N.; Reisler, E.; Zink, J. I., Allosteric Regulation of Enzymatic Reactions in a Transparent Inorganic Sol-Gel Material. *Journal of Sol-Gel Science and Technology* **1999,** *15* (1), 57-62.

33. Brennan, J. D., Using Intrinsic Fluorescence to Investigate Proteins Entrapped in Sol-Gel Derived Materials. *Applied Spectroscopy* **1999,** *53* (3), 106A-121A.

34. Hartnett, A. M.; Ingersoll, C. M.; Baker, G. A.; Bright, F. V., Kinetics and Thermodynamics of Free Flavins and the Flavin-Based Redox Active Site within Glucose Oxidase Dissolved in Solution or Sequestered within a Sol−Gel-Derived Glass. *Analytical Chemistry* **1999,** *71* (6), 1215-1224.

35. Edmiston, P. L.; Wambolt, C. L.; Smith, M. K.; Saavedra, S. S., Spectroscopic Characterization of Albumin and Myoglobin Entrapped in Bulk Sol-Gel Glasses. *Journal of Colloid and Interface Science* **1994,** *163* (2), 395-406.

36. Nishida, F.; McKiernan, J. M.; Dunn, B.; Zink, J. I.; Brinker, C. J.; Hurd, A. J., In Situ Fluorescence Probing of the Chemical Changes during Sol–Gel Thin Film Formation. *Journal of the American Ceramic Society* **1995,** *78* (6), 1640-1648.

37. Dunn, B.; Zink, J. I., Optical properties of sol–gel glasses doped with organic molecules. *Journal of Materials Chemistry* **1991,** *1* (6), 903-913.

38. Gilliland, J. W.; Yokoyama, K.; Yip, W. T., Effect of Coulombic Interactions on Rotational Mobility of Guests in Sol−Gel Silicate Thin Films. *Chemistry of Materials* **2004,** *16* (20), 3949-3954.

39. Upvan, N.; Run, W.; Prasad, P. N.; Bright, F. V., Effects of aging on the dynamics of rhodamine 6G in tetramethyl orthosilicate-derived sol-gels. *J. phys. chem. (1952)* **1994,** *98* (1), 17-22.

40. Narang, U.; Jordan, J. D.; Bright, F. V.; Prasad, P. N., Probing the Cybotactic Region of Prodan in Tetramethyl Orthosilicate-Derived Sol-Gels. *J. Phys. Chem.* **1994,** *98* (33), 8101-8107.

41. Gilliland, J. W.; Yokoyama, K.; Yip, W. T., Solvent Effect on Mobility and Photostability of Organic Dyes Embedded inside Silica Sol−Gel Thin Films. *Chemistry of Materials* **2005,** *17* (26), 6702-6712.

42. Rottman, C.; Grader, G. S.; De Hazan, Y.; Avnir, D., Sol−Gel Entrapment of ET(30) in Ormosils. Interfacial Polarity−Fractality Correlation. *Langmuir* **1996,** *12* (23), 5505-5508.

43. Bhatia, R. B.; Brinker, C. J.; Gupta, A. K.; Singh, A. K., Aqueous Sol−Gel Process for Protein Encapsulation. *Chemistry of Materials* **2000,** *12* (8), 2434-2441.

44. Gill, I.; Ballesteros, A., Encapsulation of Biologicals within Silicate, Siloxane, and Hybrid Sol−Gel Polymers: An Efficient and Generic Approach. *Journal of the American Chemical Society* **1998,** *120* (34), 8587-8598.

45. Ryu, Y. H.; Yeo, K. B.; Ki, M.-R.; Kim, Y. J.; Pack, S. P., Improved stability and reusability of endoglucanase from Clostridium thermocellum by a biosilica-based auto-encapsulation method. *Biochemical Engineering Journal* **2016,** *105*, 144-149.

46. Jerónimo, P. C. A.; Araújo, A. N.; Conceição B.S.M. Montenegro, M., Optical sensors and biosensors based on sol–gel films. *Talanta* **2007,** *72* (1), 13-27.

47. Zhang, F.; Wang, M.; Liang, C.; Jiang, H.; Shen, J.; Li, H., Thin-Layer Polymer Wrapped Enzymes Encapsulated in Hierarchically Mesoporous Silica with High Activity and Enhanced Stability. *Scientific Reports* **2014,** *4* (1), 4421.

48. Nishikiori, H.; Setiawan, R. A.; Kawamoto, S.; Takagi, S.; Teshima, K.; Fujii, T., Dimerization of xanthene dyes in sol–gel titania films. *Catalysis Science & Technology* **2013,** *3* (10), 2786-2792.

49. Banet, P.; Legagneux, L.; Hesemann, P.; Moreau, J. J. E.; Nicole, L.; Quach, A.; Sanchez, C.; Tran-Thi, T. H., Hybrid mesostructured thin films functionalized with DBM as new selective sensors of BF3. *Sensors and Actuators B: Chemical* **2008,** *130* (1), 1-8.

50. Reisfeld, R.; Zigansky, E.; Saraidarov, T., Steady state spectroscopy and stability of tris(8-hydroxy quinoline) aluminum and ruthenium tris bipyridile chloride in sol–gel glasses. *Optical Materials* **2008,** *30* (11), 1706-1709.

51. Mackenzie, J. D., Sol-Gel Research—Achievements Since 1981 and Prospects for the Future. *Journal of Sol-Gel Science and Technology* **2003,** *26* (1), 23-27.

52. Khan, M. I.; Bhatti, K. A.; Qindeel, R.; Althobaiti, H. S.; Alonizan, N., Structural, electrical and optical properties of multilayer TiO2 thin films deposited by sol–gel spin coating. *Results in Physics* **2017,** *7*, 1437-1439.

53. Kumar, A.; Mondal, S.; Kumar, S. G.; Koteswara Rao, K. S. R., High performance sol–gel spin-coated titanium dioxide dielectric based MOS structures. *Materials Science in Semiconductor Processing* **2015,** *40*, 77-83.

54. Reisfeld, R.; Manor, N.; Avnir, D., Transparent high surface area porous supports as new materials for luminescent solar concentrators. *Solar Energy Materials* **1983,** *8* (4), 399-409.

55. Guo, D.; Xiao, S.; Fan, K.; Yu, J., Hierarchical TiO2 Submicrorods Improve the Photovoltaic Performance of Dye-Sensitized Solar Cells. *ACS Sustainable Chemistry & Engineering* **2017,** *5* (2), 1315-1321.

56. Nonomura, K.; Vlachopoulos, N.; Unger, E.; Häggman, L.; Hagfeldt, A.; Boschloo, G., Blocking the Charge Recombination with Diiodide Radicals by TiO2 Compact Layer in Dye-Sensitized Solar Cells. *Journal of The Electrochemical Society* **2019,** *166* (9), B3203-B3208.

57. Czarnobaj, K.; Łukasiak, J., In Vitro Release of Cisplatin from Sol-Gel Processed Porous Silica Xerogels. *Drug Delivery* **2004,** *11* (6), 341-344.

58. Campbell, A. L. O.; Lei, Q.; Tak Yip, W., Kinetic approach to hyper-doped optical quality thin films. *Chemical Communications* **2014,** *50* (66), 9321-9324.

59. Nishikiori, H.; Uesugi, Y.; Takami, S.; Setiawan, R. A.; Fujii, T.; Qian, W.; El-Sayed, M. A., Influence of Steam Treatment on Dye−Titania Complex Formation and Photoelectric Conversion Property of Dye-Doped Titania Gel. *The Journal of Physical Chemistry C* **2011,** *115* (6), 2880-2887.

60. Lei, Q.; Yip, W. T., Probing the Effect of Post-Synthesis Grafting on Guest−Host Interactions in Sol−Gel Silica with Single-Molecule Mobility and Photostability. *The Journal of Physical Chemistry C* **2009,** *113* (50), 21130-21138.

61. Jensen, J. M.; Yip, W. T., Amine Functionalization of Silica Sol–Gel Thin Films via Kinetic Doping: A Novel, Green Approach. *ACS Omega* **2019,** *4* (20), 18545-18554.

62. Jensen, J. M.; Yip, W. T., Enzyme Loading in Internally-Coated Capillary Tubes Via Kinetic Doping. *Coatings* **2020,** *10* (6), 532.

63. Crosley, M. S.; Yip, W. T., Multienzyme, Multistep Biosensor Produced through Kinetic Doping. *The Journal of Physical Chemistry B* **2019,** *123* (18), 3962-3967.

64. Crosley, M. S.; Yip, W. T., Kinetically Doped Silica Sol–Gel Optical Biosensors: Expanding Potential Through Dip-Coating. *ACS Omega* **2018,** *3* (7), 7971-7978.

65. O'Regan, B.; Grätzel, M., A low-cost, high-efficiency solar cell based on dye-sensitized colloidal TiO2 films. *Nature* **1991,** *353* (6346), 737-740.

66. Taleb, A.; Mesguich, F.; Hérissan, A.; Colbeau-Justin, C.; Yanpeng, X.; Dubot, P., Optimized TiO2 nanoparticle packing for DSSC photovoltaic applications. *Solar Energy Materials and Solar Cells* **2016,** *148*, 52-59.

2. Dye Sensitized Solar Cells

2.1 The Grätzel Cell

While there were a few earlier attempts at creating solar cells with dye loaded to absorb light that contributed to their ideas, Brian O'Regan and Michael Grätzel co-invented a prototype solar cell that became the basis of the majority of dye sensitized solar cells (DSSCs) today.[1, 2] This prototype DSSC technology was revolutionary in that it was one of the first alternative solar cell designs to exhibit a comparable light conversion efficiency to some of the early silicon solar cells.[3]

The most fundamental difference between DSSCs and other solar cells is the separation of the light-harvesting and charge-carrying functions. Light strikes the solar cell, and the dye molecule absorbs a photon to excite the molecule and inject an electron into the charge-carrier material. A semiconductor material such as TiO_2 is used as the charge-carrier. To complete the cycle, a redox electrolyte within the cell will reduce the dye back to its neutral form. A diagram of a generic DSSC is displayed in Figure 2.1.

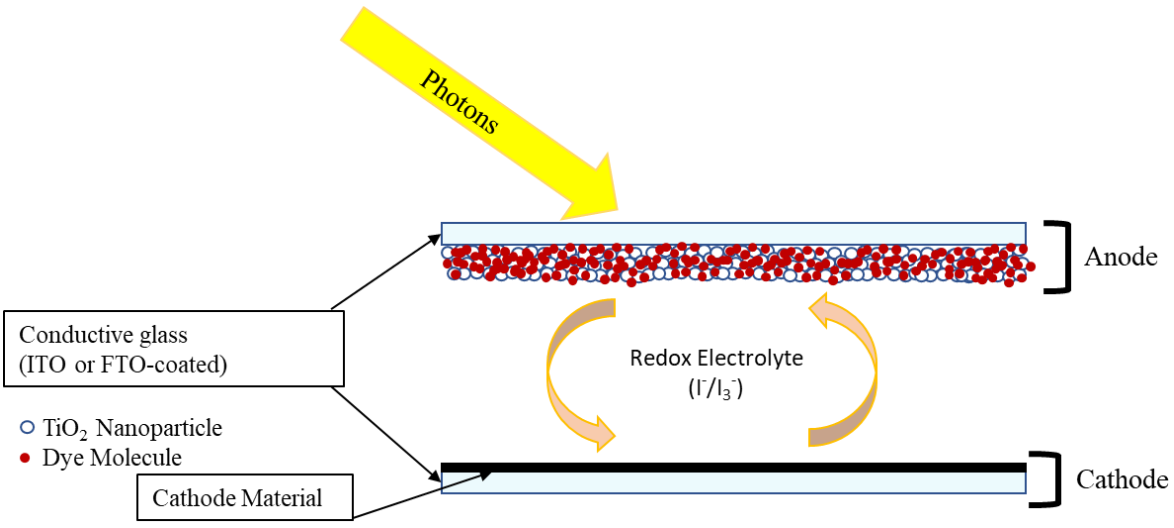

Figure 2.1 Diagram of a generic DSSC

2.2 Evaluating Solar Cell Efficiency

To standardize the evaluation of solar cell efficiency, the American Society for Testing and Materials have determined a set of specific lighting conditions to represent the average distribution of solar irradiance across the light spectrum. While some efficiency measurements are made using the extraterrestrial reference spectrum of AM0, most are performed using the AM1.5 terrestrial reference spectrum. The AM1.5 reference spectrum was developed from the average conditions that would be expected across the contiguous United States.[4] This is also generally done using an irradiance power density of 1000 $\frac{W}{m^2}$.

Under these defined lighting conditions, there are three main methods to evaluate solar cell performance. The most comprehensive and easily measured method is Power Conversion Efficiency (PCE)(η(%)). PCE is essentially the ratio of useful power out of the solar cell to the power of incident light. The following equations demonstrate how PCE is calculated, utilizing the fill factor (*FF(%)*), the open-circuit voltage (V_{oc}), and the short-circuit current (I_{sc}) to calculate the maximum power output (P_{out}).[3, 5] V_{max} is the voltage and I_{max} is the current of the largest rectangular area under the *I-V* curve.[6] The power of the incident light (P_{in}) is calculated by multiplying the incident power density by the active area of the solar cell.

$$FF(\%) = \left(\frac{V_{max} \times I_{max}}{V_{oc} \times I_{sc}}\right) \times 100\% \rightarrow \frac{FF(\%)}{100\%} = \frac{V_{max} \times I_{max}}{V_{oc} \times I_{sc}}$$

$$\rightarrow FF \times V_{oc} \times I_{sc} = V_{max} \times I_{max}$$

$$\eta(\%) = \left(\frac{V_{oc} \times I_{sc} \times FF}{P_{in}}\right) \times 100\% = \left(\frac{P_{out}}{P_{in}}\right) \times 100\%$$

The second main method is referred to as either Incident Photon to Current Efficiency (IPCE), or External Quantum Efficiency (EQE). What EQE measures is the ratio of the number of electrons

induced per number of incident photons measured at individual wavelengths. Thus, EQE is wavelength specific. The equation used to calculate EQE is as follows:

$$EQE(\lambda) = \frac{hcI_\lambda}{P_\lambda Ae\lambda}$$

Where h is Planck's constant, c is the speed of light, I_λ is the current produced while illuminated under the specific wavelength λ, P_λ is the power density of the incident light at the specific excitation wavelength λ, A is the active area of the solar cell, and e is the electronic charge.[7, 8] This method is particularly beneficial for determining at which wavelengths light is absorbed in a useful capacity.

The third common method is Internal Quantum Efficiency, or IQE. EQE and IQE differ only in which incident photons they count as part of the denominator. Where EQE uses the full incident power density at the measured wavelength, IQE only includes photons that are actually absorbed by the material. IQE is essentially the EQE divided by the fraction of light absorbed by the material at the wavelength in question.[9, 10] The fraction of light absorbed is calculated by measuring the light that is reflected off (R) or transmitted through (T) the material.

$$IQE(\lambda) = \frac{EQE(\lambda)}{(1 - R - T)}$$

As a result, IQE will always be greater than EQE.

At low power outputs, PCE is the more reliable measure of efficiency as the other two methods measure how individual wavelengths are absorbed and utilized, which requires the power output of the solar cell to be high enough to produce a measurable signal at individual wavelengths.

2.3 Current Research in DSSCs

The initial DSSC had an overall PCE of 7.1% under standard AM1.5, 1000 $\frac{W}{m^2}$ conditions.[3] Since that first achievement in 1991, many researchers have taken on the challenge to improve it further. Each component of the cell has been explored with the goal to increase efficiency or improve overall fabrication feasibility.

2.3.1 The Redox Electrolyte

One of the main components, the redox electrolyte, is a solution containing the solvent, the redox couple, and any other additives. The ideal electrolyte would have long-term stability within the cell and would not corrode the cell components. It would be able to produce efficient dye regeneration and contact between the two working electrodes. To be particularly effective, it also cannot overlap with the absorption spectra of the light sensitizer used.[6, 11] Based on these criteria, various avenues of research have emerged to try and improve the redox electrolyte. The research distills into two main categories – the redox couple, and the solvent, which includes additives beyond the redox couple itself. Both aspects are critical to the function of the overall solar cell.

The solvent used for the electrolyte solution has a wide variety of recipes, every aspect of which is going to affect the effectiveness of the electrolyte solution. Examining different reviews that collect the solvent information, it's clear that the ideal solvent mixture is far from settled.[12-14] One aspect of the solvent that has been generally agreed upon is that while an aqueous solvent would be ideal from a green perspective, purely aqueous solvents are less efficient than organic solvents.[15-17]

While the I^-/I_3^- redox couples is traditional, it can cause dye degradation and has a destructive effect on glass, titanium dioxide, and platinum.[6] Redox couples such as Co^{3+}/Co^{2+} or Cu^{2+}/Cu^{+} have recently become more popular and have been successfully used in solar cells with PCE

efficiency values as high as 13.6% for cobalt ion electrolyte pairs or 13.1% using copper ion electrolytes.[18-25]

2.3.2 The Cathode

Using new redox couples requires research into more effective cathode material. Platinum was considered the most efficient cathode material for the I^-/I_3^- redox couple, even with the destructive effect, but that may not be true for the Co^{3+}/Co^{2+} and Cu^{2+}/Cu^+ redox couples. Platinum is also expensive, driving up the cost of fabrication. To lower the cost of producing DSSCs, cathode materials with a lower fabrication cost would be useful.[6] Some such counter electrodes are poly(3,4-ethylenedioxythiophene) (PEDOT), CoSe nanoparticle structures, or various forms of carbon.[18, 19, 22, 26, 27] The CoSe nanoparticle structures have even demonstrated a PCE of 9.29% under AM1.5 conditions using an I^-/I_3^- electrolyte.[22] Coating an FTO plate with carbon black using a spin-coating method, described by Liu et al, is one of the lowest cost cathode materials, and has demonstrated a PCE of up to 7% when paired with a Co^{3+}/Co^{2+} redox couple.[18] Pairing a Cu^{2+}/Cu^+ redox couple with a PEDOT counter electrode has resulted in cells with a PCE of 13.1%.[25]

2.3.3 The Anode

Regarding the anode material, which is the primary focus of this work, research has mainly focused on changing the identity of the semiconductor material, altering its nanostructure, or improving the light-harvesting molecules used.

The identity of the metal oxide material used for the anode will obviously play a role in the overall efficiency of the solar cell. The primary job of the metal oxide is to act as a charge-carrier material, therefore how well it transports electrons is paramount. While this work will utilize

TiO_2 as the metal oxide material, similar to the initial Grätzel cell, many different metal oxides have been explored in DSSC research. Some of these metal oxides which have shown promise are SnO_2 and ZnO.[28-30] Another way that the semiconductor material is adapted to increase PCE is by doping it with nitrogen or various metals such as gold, silver, sulfur, tin, lithium, tantalum or gallium.[31-37]

Generally, the primary purpose of altering the nanostructure of the metal oxide material is to either achieve a more efficient crystal structure or to increase the dye absorption by increasing the open surface area of the semiconductor material. If the metal oxide material in question has multiple crystal forms, determining which is the most effective in DSSCs is worth looking into. For example, TiO_2 has three main crystal organizations, anatase, rutile and brookite. A TiO_2 anode material can be constructed from any of the three crystal structures individually, or a mixture of them.[33, 38-43] To increase the surface area, the oxide material is generally formed into an array of nanoparticles, nanofibers, nanorods, nanotubes, nanoleaves, or nanoflowers (nanorods organized into urchin-like structures).[29, 33, 36, 37, 44-49]

Improving the light harvesting molecules can be accomplished by using dye molecules that will absorb a greater range of light on their own, utilizing a mixture of dyes as the sensitizers, or using carbon nanodots as light-harvesters instead of organic dyes.[20, 21, 50-53] With high-efficiency dyes such as the one created by Zhang et al, it was possible to produce solar cells with up to 13.6% efficiency under standard AM1.5 conditions.[20] Co-sensitization, meaning multiple dyes are used as the sensitizers instead of a single dye, has been proven to significantly increase the efficiency of a solar cell which is otherwise identically created.[52, 54]

2.4 The Potential Benefits of Kinetic Doping in a DSSC Anode Material

As previously discussed, there are many areas of focus in DSSC research, but this work will focus on utilizing kinetic doping to construct a smooth, hyper-doped anode layer for a prototype solar cell. The success with kinetic hyper-doping in silica sol-gel derived thin films achieved by the Yip lab sparked an interest in the potential applications of kinetic doping in other metal oxide materials.[55-59] As other metal oxides like titanium dioxide thin films can similarly be created by the sol-gel process. The kinetic doping process should be similarly effective. After researching the general anode design in DSSCs, we came to believe there was great potential for hyper-doped TiO_2 thin films in developing an efficient anode material for a DSSC.

2.4.1 Kinetic Doping Provides an Instant Increase in Dye Concentration

It is an accepted fact that only light-harvesting molecules in direct contact with the semiconductor material will inject useful electrons to the circuit. Therefore, it is a common goal when focused on the anode material to increase the surface area available to adsorb the light-harvesting molecules. This is generally accomplished by forming an anode structure made of nanoparticles or nanotubes instead of smooth films. Unfortunately, this approach causes an increase in electron scattering and recombination loss across grain boundaries. Nevertheless, this is still considered a viable approach because the number of electrons injected based on the increase in active surface area far outpaces the loss. Kinetic doping has proven in silica films to create a contiguous film with unprecedented concentrations of loaded dye within the pores.[55] If similar dye loading capacity can be achieved in a smooth titanium dioxide thin film, it should increase light harvesting efficiency while substantially limiting the presence of grain boundaries that cause electron scattering loss.

2.4.2 Kinetic Doping Allows for Tunability of Thickness

A second popular method of increasing the surface area associated with dye-semiconductor interactions is increasing the thickness of the active layer. Although increasing the thickness increases the individual photon's likelihood of being absorbed, the distance that an injected electron needs to travel before entering the external circuit also increases. Therefore, the probability that an individual electron will undergo recombination rather than travel through the circuit also increases.[60] For any given material, there should be an optimal thickness above which the increase in recombination begins to negatively affect the efficiency. Increasing the thickness up until that point will result in a higher overall efficiency, as the increased thickness will result in increased photon absorption.[61] Because the highest efficiency will be achieved at an optimal thickness, it is a reasonably common practice to create a variety of anode thicknesses and compare the measured efficiency.[62, 63]

Our proposed material would allow for a higher concentration of dye molecules, as discussed in 2.4.1, within a thin layer of TiO_2 film. Since the spin-coating process allows for the creation of individually spun thin films with consistent thicknesses, it should be possible to optimize the DSSC efficiency in a controlled manner by layering the films. As most anode layers reported in the literature range from 2-20 μm thick, this should allow a great amount of control while establishing the optimal thickness for our anode material.[21, 43, 47, 64, 65]

2.4.3 Kinetic Doping Allows for Simple Cosensitization of Anode Material

A universal goal necessary for increasing solar cell efficiency is to absorb and utilize photons across as much of the solar spectrum as possible. While research in DSSCs is being done with organic dyes as sensitizers due to their availability and low environmental impact, each dye can only utilize light within a narrow bandwidth. Therefore, cosensitization of DSSC material is a

popular area of research to raise the overall PCE.[16, 52, 54, 66, 67] Kinetic doping has proven the ability to load multiple proteins simultaneously in silica thin films, indicating the very real potential of loading multiple dyes in a single step to absorb across a much broader bandwidth.[57]

2.5 References

1. Matsumura, M.; Nomura, Y.; Tsubomura, H., Dye-sensitization on the Photocurrent at Zinc Oxide Electrode in Aqueous Electrolyte Solution. *Bulletin of the Chemical Society of Japan* **1977,** *50* (10), 2533-2537.

2. Willig, F.; Eichberger, R.; Sundaresan, N. S.; Parkinson, B. A., Experimental time scale of Gerischer's distribution curves for electron-transfer reactions at semiconductor electrodes. *Journal of the American Chemical Society* **1990,** *112* (7), 2702-2707.

3. O'Regan, B.; Grätzel, M., A low-cost, high-efficiency solar cell based on dye-sensitized colloidal TiO2 films. *Nature* **1991,** *353* (6346), 737-740.

4. Reference Air Mass 1.5 Spectra https://www.nrel.gov/grid/solar-resource/spectra-am1.5.html (accessed 4/14).

5. Slooff, L. H.; Veenstra, S. C.; Kroon, J. M.; Moet, D. J. D.; Sweelssen, J.; Koetse, M. M., Determining the internal quantum efficiency of highly efficient polymer solar cells through optical modeling. *Applied Physics Letters* **2007,** *90* (14), 143506.

6. Sharma, K.; Sharma, V.; Sharma, S. S., Dye-Sensitized Solar Cells: Fundamentals and Current Status. *Nanoscale Research Letters* **2018,** *13* (1), 381.

7. Yin, W.; Yang, J.; Zhao, K.; Cui, A.; Zhou, J.; Tian, W.; Li, W.; Hu, Z.; Chu, J., High Responsivity and External Quantum Efficiency Photodetectors Based on Solution-Processed Ni-Doped CuO Films. *ACS Applied Materials & Interfaces* **2020,** *12* (10), 11797-11805.

8. Sahatiya, P.; Reddy K, C. S.; Badhulika, S., Discretely distributed 1D V2O5 nanowires over 2D MoS2 nanoflakes for an enhanced broadband flexible photodetector covering the ultraviolet to near infrared region. *Journal of Materials Chemistry C* **2017,** *5* (48), 12728-12736.

9. Armin, A.; Kassal, I.; Shaw, P. E.; Hambsch, M.; Stolterfoht, M.; Lyons, D. M.; Li, J.; Shi, Z.; Burn, P. L.; Meredith, P., Spectral Dependence of the Internal Quantum Efficiency of Organic Solar Cells: Effect of Charge Generation Pathways. *Journal of the American Chemical Society* **2014,** *136* (32), 11465-11472.

10. Dennler, G.; Forberich, K.; Scharber, M. C.; Brabec, C. J.; Tomiš, I.; Hingerl, K.; Fromherz, T., Angle dependence of external and internal quantum efficiencies in bulk-heterojunction organic solar cells. *Journal of Applied Physics* **2007,** *102* (5), 054516.

11. Wu, J.; Lan, Z.; Hao, S.; Li, P.; Lin, J.; Huang, M.; Fang, L.; Huang, Y., Progress on the electrolytes for dye-sensitized solar cells. *Pure and Applied Chemistry* **2008,** *80* (11), 2241-2258.

12. Kokkonen, M.; Talebi, P.; Zhou, J.; Asgari, S.; Soomro, S. A.; Elsehrawy, F.; Halme, J.; Ahmad, S.; Hagfeldt, A.; Hashmi, S. G., Advanced research trends in dye-sensitized solar cells. *Journal of Materials Chemistry A* **2021,** *9* (17), 10527-10545.

13. Abu Talip, R. A.; Yahya, W. Z.; Bustam, M. A., Ionic Liquids Roles and Perspectives in Electrolyte for Dye-Sensitized Solar Cells. *Sustainability* **2020,** *12* (18).

14. Venkatesan, S.; Lee, Y.-L., Nanofillers in the electrolytes of dye-sensitized solar cells – A short review. *Coordination Chemistry Reviews* **2017,** *353*, 58-112.

15. Law, C.; Pathirana, S. C.; Li, X.; Anderson, A. Y.; Barnes, P. R.; Listorti, A.; Ghaddar, T. H.; O′ Regan, B. C., Water‐based electrolytes for dye‐sensitized solar cells. *Advanced Materials* **2010,** *22* (40), 4505-4509.

16. Kim, J.-H.; Kim, D.-H.; So, J.-H.; Koo, H.-J., Toward Eco-Friendly Dye-Sensitized Solar Cells (DSSCs): Natural Dyes and Aqueous Electrolytes. *Energies* **2022,** *15* (1).

17. Iftikhar, H.; Sonai, G. G.; Hashmi, S. G.; Nogueira, A. F.; Lund, P. D., Progress on Electrolytes Development in Dye-Sensitized Solar Cells. *Materials* **2019,** *12* (12).

18. Liu, I. P.; Hou, Y.-C.; Li, C.-W.; Lee, Y.-L., Highly electrocatalytic counter electrodes based on carbon black for cobalt(iii)/(ii)-mediated dye-sensitized solar cells. *Journal of Materials Chemistry A* **2017,** *5* (1), 240-249.

19. Tathavadekar, M.; Biswal, M.; Agarkar, S.; Giribabu, L.; Ogale, S., Electronically and Catalytically Functional Carbon Cloth as a Permeable and Flexible Counter Electrode for Dye Sensitized Solar Cell. *Electrochimica Acta* **2014,** *123,* 248-253.

20. Zhang, L.; Yang, X.; Wang, W.; Gurzadyan, G. G.; Li, J.; Li, X.; An, J.; Yu, Z.; Wang, H.; Cai, B.; Hagfeldt, A.; Sun, L., 13.6% Efficient Organic Dye-Sensitized Solar Cells by Minimizing Energy Losses of the Excited State. *ACS Energy Letters* **2019,** *4* (4), 943-951.

21. Ren, Y.; Sun, D.; Cao, Y.; Tsao, H. N.; Yuan, Y.; Zakeeruddin, S. M.; Wang, P.; Grätzel, M., A Stable Blue Photosensitizer for Color Palette of Dye-Sensitized Solar Cells Reaching 12.6% Efficiency. *Journal of the American Chemical Society* **2018,** *140* (7), 2405-2408.

22. Huang, Y.-J.; Chen, H.-T.; Ann, S.-B.; Li, C.-T.; Lin, J. T.; Lee, C.-P.; Ho, K.-C., Hierarchical urchin-like CoSe2/CoSeO3 electro-catalysts for dye-sensitized solar cells: up to 19% PCE under dim light illumination. *Journal of Materials Chemistry A* **2019,** *7* (45), 26089-26097.

23. Pradhan, S. C.; Velore, J.; Hagfeldt, A.; Soman, S., Probing photovoltaic performance in copper electrolyte dye-sensitized solar cells of variable TiO2 particle size using comprehensive interfacial analysis. *Journal of Materials Chemistry C* **2022,** *10* (10), 3929-3936.

24. Saygili, Y.; Söderberg, M.; Pellet, N.; Giordano, F.; Cao, Y.; Muñoz-García, A. B.; Zakeeruddin, S. M.; Vlachopoulos, N.; Pavone, M.; Boschloo, G.; Kavan, L.; Moser, J.-E.; Grätzel, M.; Hagfeldt, A.; Freitag, M., Copper Bipyridyl Redox Mediators for Dye-Sensitized Solar Cells with High Photovoltage. *Journal of the American Chemical Society* **2016,** *138* (45), 15087-15096.

25. Cao, Y.; Liu, Y.; Zakeeruddin, S. M.; Hagfeldt, A.; Grätzel, M., Direct Contact of Selective Charge Extraction Layers Enables High-Efficiency Molecular Photovoltaics. *Joule* **2018,** *2* (6), 1108-1117.

26. Pringle, J. M.; Armel, V.; MacFarlane, D. R., Electrodeposited PEDOT-on-plastic cathodes for dye-sensitized solar cells. *Chemical Communications* **2010,** *46* (29), 5367-5369.

27. Yue, G.; Wu, J.; Xiao, Y.; Lin, J.; Huang, M.; Fan, L.; Yao, Y., A dye-sensitized solar cell based on PEDOT:PSS counter electrode. *Chinese Science Bulletin* **2013,** *58* (4), 559-566.

28. Zainudin, S. N. F.; Abdullah, H.; Markom, M., Electrochemical studies of tin oxide based-dye-sensitized solar cells (DSSC): a review. *Journal of Materials Science: Materials in Electronics* **2019,** *30* (6), 5342-5356.

29. Aksoy, S.; Polat, O.; Gorgun, K.; Caglar, Y.; Caglar, M., Li doped ZnO based DSSC: Characterization and preparation of nanopowders and electrical performance of its DSSC. *Physica E: Low-dimensional Systems and Nanostructures* **2020,** *121*, 114127.

30. Lee, J.-H.; Park, N.-G.; Shin, Y.-J., Nano-grain SnO2 electrodes for high conversion efficiency SnO2–DSSC. *Solar Energy Materials and Solar Cells* **2011,** *95* (1), 179-183.

31. Muduli, S.; Game, O.; Dhas, V.; Vijayamohanan, K.; Bogle, K. A.; Valanoor, N.; Ogale, S. B., TiO2–Au plasmonic nanocomposite for enhanced dye-sensitized solar cell (DSSC) performance. *Solar Energy* **2012,** *86* (5), 1428-1434.

32. Ramarajan, R.; Purushothamreddy, N.; Dileep, R. K.; Kovendhan, M.; Veerappan, G.; Thangaraju, K.; Paul Joseph, D., Large-area spray deposited Ta-doped SnO2 thin film electrode for DSSC application. *Solar Energy* **2020,** *211*, 547-559.

33. Mahmoud, M. S.; Akhtar, M. S.; Mohamed, I. M. A.; Hamdan, R.; Dakka, Y. A.; Barakat, N. A. M., Demonstrated photons to electron activity of S-doped TiO2 nanofibers as photoanode in the DSSC. *Materials Letters* **2018,** *225*, 77-81.

34. Ako, R. T.; Ekanayake, P.; Young, D. J.; Hobley, J.; Chellappan, V.; Tan, A. L.; Gorelik, S.; Subramanian, G. S.; Lim, C. M., Evaluation of surface energy state distribution and bulk defect concentration in DSSC photoanodes based on Sn, Fe, and Cu doped TiO2. *Applied Surface Science* **2015,** *351*, 950-961.

35. Chae, J.; Kim, D. Y.; Kim, S.; Kang, M., Photovoltaic efficiency on dye-sensitized solar cells (DSSC) assembled using Ga-incorporated TiO2 materials. *Journal of Industrial and Engineering Chemistry* **2010,** *16* (6), 906-911.

36. Sakthivel, T.; Ashok Kumar, K.; Ramanathan, R.; Senthilselvan, J.; Jagannathan, K., Silver doped TiO₂nano crystallites for dye-sensitized solar cell (DSSC) applications. *Materials Research Express* **2017,** *4* (12), 126310.

37. Xiang, P.; Li, X.; Wang, H.; Liu, G.; Shu, T.; Zhou, Z.; Ku, Z.; Rong, Y.; Xu, M.; Liu, L.; Hu, M.; Yang, Y.; Chen, W.; Liu, T.; Zhang, M.; Han, H., Mesoporous nitrogen-doped TiO2 sphere applied for quasi-solid-state dye-sensitized solar cell. *Nanoscale Research Letters* **2011,** *6* (1), 606.

38. https://g2voptics.com/products/pico-solar-simulator/?utm_medium=cpc&utm_source=bing&utm_term=AM1.5%20solar%20spectrum&utm_campaign=Bing:SS+SolarSimulator-Search&utm_content=ad__matchtype=e-network=o-

device=c-adgroupid=1349102132888625&msclkid=f520083597d01fa046106a542e6d266d (accessed 4-22).

39. Panepinto, A.; Michiels, M.; Dürrschnabel, M. T.; Molina-Luna, L.; Bittencourt, C.; Cormier, P. A.; Snyders, R., Synthesis of Anatase (Core)/Rutile (Shell) Nanostructured TiO2 Thin Films by Magnetron Sputtering Methods for Dye-Sensitized Solar Cell Applications. *ACS Applied Energy Materials* **2020,** *3* (1), 759-767.

40. Chen, D.; Huang, F.; Cheng, Y.-B.; Caruso, R. A., Mesoporous Anatase TiO2 Beads with High Surface Areas and Controllable Pore Sizes: A Superior Candidate for High-Performance Dye-Sensitized Solar Cells. *Advanced Materials* **2009,** *21* (21), 2206-2210.

41. Jiang, K.-J.; Kitamura, T.; Yin, H.; Ito, S.; Yanagida, S., Dye-sensitized Solar Cells Using Brookite Nanoparticle TiO2 Films as Electrodes. *Chemistry Letters* **2002,** *31* (9), 872-873.

42. Magne, C.; Cassaignon, S.; Lancel, G.; Pauporté, T., Brookite TiO2 Nanoparticle Films for Dye-Sensitized Solar Cells. *ChemPhysChem* **2011,** *12* (13), 2461-2467.

43. Liu, B.; Aydil, E. S., Growth of Oriented Single-Crystalline Rutile TiO2 Nanorods on Transparent Conducting Substrates for Dye-Sensitized Solar Cells. *Journal of the American Chemical Society* **2009,** *131* (11), 3985-3990.

44. Madurai Ramakrishnan, V.; N, M.; P, B.; Pitchaiya, S.; Velauthapillai, D.; Pugazhendhi, A., Transformation of TiO2 nanoparticles to nanotubes by simple solvothermal route and its performance as dye-sensitized solar cell (DSSC) photoanode. *International Journal of Hydrogen Energy* **2020,** *45* (31), 15441-15452.

45. Lin, J.; Guo, M.; Yip, C. T.; Lu, W.; Zhang, G.; Liu, X.; Zhou, L.; Chen, X.; Huang, H., High Temperature Crystallization of Free-Standing Anatase TiO2 Nanotube Membranes for

High Efficiency Dye-Sensitized Solar Cells. *Advanced Functional Materials* **2013,** *23* (47), 5952-5960.

46. Park, J.-H.; Kim, J.-Y.; Kim, J.-H.; Choi, C.-J.; Kim, H.; Sung, Y.-E.; Ahn, K.-S., Enhanced efficiency of dye-sensitized solar cells through TiCl4-treated, nanoporous-layer-covered TiO2 nanotube arrays. *Journal of Power Sources* **2011,** *196* (20), 8904-8908.

47. Ma, T.; Akiyama, M.; Abe, E.; Imai, I., High-Efficiency Dye-Sensitized Solar Cell Based on a Nitrogen-Doped Nanostructured Titania Electrode. *Nano Letters* **2005,** *5* (12), 2543-2547.

48. Dhas, V.; Muduli, S.; Agarkar, S.; Rana, A.; Hannoyer, B.; Banerjee, R.; Ogale, S., Enhanced DSSC performance with high surface area thin anatase TiO2 nanoleaves. *Solar Energy* **2011,** *85* (6), 1213-1219.

49. Ye, M.; Liu, H.-Y.; Lin, C.; Lin, Z., Hierarchical Rutile TiO2 Flower Cluster-Based High Efficiency Dye-Sensitized Solar Cells via Direct Hydrothermal Growth on Conducting Substrates. *Small* **2013,** *9* (2), 312-321.

50. Godfroy, M.; Liotier, J.; Mwalukuku, V. M.; Joly, D.; Huaulmé, Q.; Cabau, L.; Aumaitre, C.; Kervella, Y.; Narbey, S.; Oswald, F.; Palomares, E.; González Flores, C. A.; Oskam, G.; Demadrille, R., Benzothiadiazole-based photosensitizers for efficient and stable dye-sensitized solar cells and 8.7% efficiency semi-transparent mini-modules. *Sustainable Energy & Fuels* **2021,** *5* (1), 144-153.

51. Shah, M. F.; Mirloup, A.; Chowdhury, T. H.; Sutter, A.; Hanbazazah, A. S.; Ahmed, A.; Lee, J.-J.; Abdel-Shakour, M.; Leclerc, N.; Kaneko, R.; Islam, A., Cross-conjugated BODIPY pigment for highly efficient dye sensitized solar cells. *Sustainable Energy & Fuels* **2020,** *4* (4), 1908-1914.

52. Reddy, K. S. K.; Chen, Y.-C.; Wu, C.-C.; Hsu, C.-W.; Chang, Y.-C.; Chen, C.-M.; Yeh, C.-Y., Cosensitization of Structurally Simple Porphyrin and Anthracene-Based Dye for Dye-Sensitized Solar Cells. *ACS Applied Materials & Interfaces* **2018,** *10* (3), 2391-2399.

53. Gao, N.; Huang, L.; Li, T.; Song, J.; Hu, H.; Liu, Y.; Ramakrishna, S., Application of carbon dots in dye-sensitized solar cells: A review. *Journal of Applied Polymer Science* **2020,** *137* (10), 48443.

54. Jia, H.-L.; Li, S.-S.; Gong, B.-Q.; Gu, L.; Bao, Z.-L.; Guan, M.-Y., Efficient cosensitization of new organic dyes containing bipyridine anchors with porphyrins for dye-sensitized solar cells. *Sustainable Energy & Fuels* **2020,** *4* (1), 347-353.

55. Campbell, A. L. O.; Lei, Q.; Tak Yip, W., Kinetic approach to hyper-doped optical quality thin films. *Chemical Communications* **2014,** *50* (66), 9321-9324.

56. Crosley, M. S.; Yip, W. T., Kinetically Doped Silica Sol–Gel Optical Biosensors: Expanding Potential Through Dip-Coating. *ACS Omega* **2018,** *3* (7), 7971-7978.

57. Crosley, M. S.; Yip, W. T., Multienzyme, Multistep Biosensor Produced through Kinetic Doping. *The Journal of Physical Chemistry B* **2019,** *123* (18), 3962-3967.

58. Crosley, M. S.; Yip, W. T., Silica Sol–Gel Optical Biosensors: Ultrahigh Enzyme Loading Capacity on Thin Films via Kinetic Doping. *The Journal of Physical Chemistry B* **2017,** *121* (9), 2121-2126.

59. Jensen, J. M.; Yip, W. T., Enzyme Loading in Internally-Coated Capillary Tubes Via Kinetic Doping. *Coatings* **2020,** *10* (6), 532.

60. Lee, H.; Kim, J.; Kim, D. Y.; Seo, Y., Co-sensitization of metal free organic dyes in flexible dye sensitized solar cells. *Organic Electronics* **2018,** *52*, 103-109.

61. Domtau, D. L.; Simiyu, J.; Ayieta, E. O.; Nyakiti, L. O.; Muthoka, B.; Mwabora, J. M., Effects of TiO₂ Film Thickness and Electrolyte Concentration on Photovoltaic Performance of Dye-Sensitized Solar Cell. *Surface Review and Letters* **2017,** *24*, 1750065.

62. Kao, M. C.; Chen, H. Z.; Young, S. L.; Kung, C. Y.; Lin, C. C., The effects of the thickness of TiO2 films on the performance of dye-sensitized solar cells. *Thin Solid Films* **2009,** *517* (17), 5096-5099.

63. Baglio, V.; Girolamo, M.; Antonucci, V.; Aricò, A., Influence of TiO2 film thickness on the electrochemical behaviour of dye-sensitized solar cells. *Int. J. Electrochem. Sci* **2011,** *6* (8), 3375-3384.

64. Galliano, S.; Bella, F.; Gerbaldi, C.; Falco, M.; Viscardi, G.; Grätzel, M.; Barolo, C., Photoanode/Electrolyte Interface Stability in Aqueous Dye-Sensitized Solar Cells. *Energy Technology* **2017,** *5* (2), 300-311.

65. Jose, R.; Kumar, A.; Thavasi, V.; Ramakrishna, S., Conversion efficiency versus sensitizer for electrospun TiO₂nanorod electrodes in dye-sensitized solar cells. *Nanotechnology* **2008,** *19* (42), 424004.

66. Cole, J. M.; Pepe, G.; Al Bahri, O. K.; Cooper, C. B., Cosensitization in Dye-Sensitized Solar Cells. *Chemical Reviews* **2019,** *119* (12), 7279-7327.

67. Wu, Z.-S.; Song, X.-C.; Liu, Y.-D.; Zhang, J.; Wang, H.-S.; Chen, Z.-J.; Liu, S.; Weng, Q.; An, Z.-W.; Guo, W.-J., New organic dyes with varied arylamine donors as effective co-sensitizers for ruthenium complex N719 in dye sensitized solar cells. *Journal of Power Sources* **2020,** *451*, 227776.

3. Materials, Techniques, and Instrumentation

3.1 Materials

Titanium (IV) isopropoxide (97%) was purchased from Sigma Aldrich and used as received. Ethanol (100%) was purchased from Pharmco and used as received. Concentrated nitric acid (70%) was purchased from Macron and used as received. Glass coverslips (25 mm × 25 mm, premium grade) were purchased from Fisher Scientific and cleaned prior to use.

Several organic dyes were used in the loading solutions. Dyes purchased from Sigma Aldrich were Rhodamine 6G, (95%), Tris(2,2'-bipyridyl)dichlororuthenium(II) hexahydrate at (99.95%), Auramine O (85%), Nile Blue Chloride (85%), Eosin B (90%), Bromophenol Blue, and Rhodamine B. Fluorescein was purchased from Eastman Organic Chemicals.

The 100 mM phosphate buffer solution used to create dye loading solutions and the initial 10 mM phosphate buffer rinse solution was prepared using sodium phosphate monobasic from Mallinckrodt, balanced with dilute sodium hydroxide solution and if necessary, dilute phosphoric acid to adjust the buffer pH. The sodium hydroxide pellets used to create a dilute solution were from Macron and the phosphoric acid was from Merck.

In the solar cell experiments, ITO plates (10 Ohm/sq, 25 mm × 25 mm) were purchased from Nanocs and used as received. For each solar cell created, a second ITO plate was coated with graphite using a woodless graphite pencil (2B) to use as the cathode. Potassium iodide from Fischer and iodine crystals from Macron were used to create an aqueous redox electrolyte solution that contains 0.55 M potassium iodide and 5 mM iodine.

3.2 Preparation of Glass Coverslips

To remove residual contaminants, the glass coverslips were sonicated in an acetone bath for 30 minutes. Coverslips were then rinsed three times with Millipore water and sonicated for 5 minutes. After this, they were switched to a clean container and sonicated in 10% NaOH for 30 minutes. Finally, the glass coverslips were again rinsed three times in Millipore water and sonicated for a final 30 minutes. Once the cleansing process is complete, the coverslips were stored in Millipore water and covered until use.[1]

3.3 Preparation of Titania Sol-Gel for Spin-Coating

The general reagents and reagent ratio of the sol-gel solution was adapted from the published recipe reported by Nishikiori et al.[2, 3] Precursor solution was prepared in 1.5 mL microcentrifuge tubes by adding 1120 µL of 99% ethanol, then 224 µL of titanium (IV) isopropoxide. After mixing by vortex for 30 seconds, 21 µL of 70% nitric acid was added and mixed into the solution before finally adding 28 µL of Millipore water. Once the precursor solution was created, the microcentrifuge tube was capped and then sealed with parafilm before allowing it to age for 19-24 hours prior to use. It is important to note that changing the order of reagent addition may result in immediate precipitation of TiO_2 particles, rendering the sol-gel solution useless as shown on the left in Figure 3.1. The sol-gel solution on the right is representative of a solution with the chemical reagents added in the correct order.

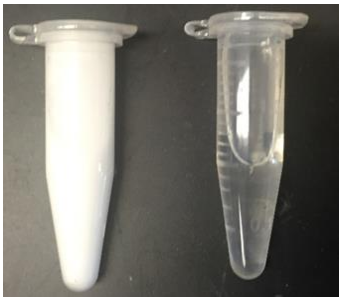

Figure 3.1 A comparison of sol-gel solutions when reagents are added in the incorrect(left) or correct (right) order.

It is worth noting that this preparation procedure for TiO_2 sol-gel creation represents a significant simplification over other known methods. Most preparation methods reported in literature indicate the need to add the titanium precursor in a dropwise manner over a much longer course of time, with constant stirring, or under conditions more extreme than simply mixing at room temperature[4-9]. With this reagent ratio and preparation procedure, as long as reagent addition is done in the correct order, sol-gel solution can be made quickly and repeatably in less than 5 minutes with minimal effort.

3.4 Preparation of Dye Loading Solutions

All dye loading solutions were prepared at ~1 mM concentration. For multi-dye solution tests, solutions of either ~1 mM total dye or ~1 mM of each individual dye were prepared.

Most dye solutions were prepared by measuring out the mass of solid dye needed and creating the ~1 mM solution in a single dilution. After placing the solid dye in the volumetric flask, 100 mM phosphate buffer would be added to the volumetric flask in the amount of $1/10^{th}$ of the final volume to create a final 10 mM phosphate buffer concentration in the dye loading solution. Millipore water was then used to dilute to the final volume. While a secondary dilution would be preferable to account for some of the inaccuracy of the mass measurements, this was only really feasible for R6G.

As R6G was most commonly used and is highly soluble, ~10 mM solutions of R6G in 10 mM phosphate buffer were prepared as a stock solution. To prepare the R6G loading solution, the stock solution would be diluted in a 10× dilution with 10 mM phosphate buffer as needed to make 1 mM R6G in 10 mM phosphate buffer.

Most individual dye loading solutions were adjusted to pH 7.3, as were all multi-dye loading solutions. Individual dye loading solutions of Tris(2,2'-bipyridyl)dichlororuthenium(II) hexahydrate and Nile Blue Chloride were adjusted to pH 8.9 in order to increase the mechanical stability of the resultant films.

3.5 Thin Film Deposition Via Spin-Coating

A clean coverslip was purge dried thoroughly using compressed air and placed in a spin-coater (Laurell Technologies Model WS-400A-6NPP/LITE) under ambient conditions. Vacuum was used to hold the coverslip in place and 120 μL of aged titania sol-gel solution was pipetted onto the coverslip and spun at 6100 RPM for 70 seconds. After a pre-determined post spin-coat delay, the nascent titania thin films used for kinetic doping were quickly submerged in 20 mL of the intended dye loading solution and left in the solution for 1 hour. After an hour, films were rinsed twice, first in 10 mM phosphate buffer, and subsequently in Millipore water. Immediately after rinsing, films were purge dried under compressed air. The film is fairly fragile before it fully sets after drying. To protect the film, it was necessary to aim the compressed air perpendicular to the film and purge the film surface gently. Blank control films without dye doping were allowed to condense in open air after spin-coating.

3.6 UV-Vis Spectroscopy

UV-Vis spectroscopy was used to measure dye concentration in TiO_2 thin films loaded through kinetic doping. The absorption spectra used in this work were all taken using the parallel double-beam configuration of a Shimadzu UV-2101PC UV-Vis scanning spectrometer. Most determination of dye concentration was done directly from the solid films on the 25 mm × 25 mm glass coverslip substrates. Since these coverslips cannot fit into a standard spectrometer sample compartment, a custom stand specifically created for the work with silica thin films was

used to hold the coverslips directly in the path of the sample beam. A clean coverslip coated with a blank film was used as the reference for the double-beam spectrometer.

3.7 Scanning Electron Microscopy (SEM)

SEM imaging of thin film samples were collected with help from Dr. Preston Larson at the Samuel Roberts Noble Microscopy Laboratory, the core imaging facility of the University of Oklahoma. Cross-sectional SEM images were used to measure film thickness and offer a glimpse of the morphology of the thin films. A JEOL JSM-880 scanning electron microscope was used to obtain the images of the films at 20,000-100,000 X magnification after the application of a 5 nm Au-Pd sputter-coat layer.

3.8 X-Ray Diffraction Spectroscopy (XRD)

All XRD spectra obtained for this work were recorded using a Rigaku Miniflex600 Benchtop X-Ray Diffractometer. Access to the diffractometer was generously provided by Dr. Bayram Saparov of the Chemistry and Biochemistry department at the University of Oklahoma. All samples measured were affixed to a zero-background plate with the thin film facing up.

3.9 Thermal Annealing

High-temperature crystallization of thin films was performed by placing the thin films into a Thermolyne 47900 adjustable furnace at a temperature of 400°C for a period of 24 hours. The furnace was then turned off and allowed to fully cool to room temperature with the door closed before the films would be removed. No significant differences in crystallization were observed if the heating time was extended beyond 24 hours.

3.10 Hydrothermal Annealing

Hydrothermal annealing of thin films was based on the temperature and pressure requirements for hydrothermal annealing reported by Nishikiori et al.[2] The exact method used in this work utilizes a 6-quart Instant Pot® Max set on high pressure for 8 hours with automatic venting. 1000 mL of Millipore water was used for hydrothermal annealing. This kept the films under pressurized steam at a temperature of 118 ± 1 °C. Before hydrothermal annealing, the films were first annealed at 150 °C in the Thermolyne 47900 adjustable furnace for 1 hour and allowed to cool to room temperature with the door closed. This step was essential to reduce dye leaching during the hydrothermal annealing process.

3.11 Solar Cell Efficiency Measurements

To qualitatively evaluate the performance of the prototype solar cells, voltage and current data was measured under direct solar irradiance using a handheld digital multimeter. For quantitative measurements, a Kiethly source meter and Newport solar simulator belonging to Dr. Ian Sellers of the Physics department at the University of Oklahoma were used under AM1.5 and 1000 $\frac{W}{m^2}$ conditions to measure power conversion efficiency.

3.12 References

1. Crosley, M. S.; Yip, W. T., Silica Sol–Gel Optical Biosensors: Ultrahigh Enzyme Loading Capacity on Thin Films via Kinetic Doping. *The Journal of Physical Chemistry B* **2017,** *121* (9), 2121-2126.

2. Nishikiori, H.; Uesugi, Y.; Takami, S.; Setiawan, R. A.; Fujii, T.; Qian, W.; El-Sayed, M. A., Influence of Steam Treatment on Dye−Titania Complex Formation and Photoelectric Conversion Property of Dye-Doped Titania Gel. *The Journal of Physical Chemistry C* **2011,** *115* (6), 2880-2887.

3. Nishikiori, H.; Setiawan, R. A.; Kawamoto, S.; Takagi, S.; Teshima, K.; Fujii, T., Dimerization of xanthene dyes in sol–gel titania films. *Catalysis Science & Technology* **2013,** *3* (10), 2786-2792.

4. Macwan, D. P.; Dave, P. N.; Chaturvedi, S., A review on nano-TiO2 sol–gel type syntheses and its applications. *Journal of Materials Science* **2011,** *46* (11), 3669-3686.

5. Anderson, C.; Bard, A. J., An improved photocatalyst of TiO2/SiO2 prepared by a sol-gel synthesis. *The Journal of Physical Chemistry* **1995,** *99* (24), 9882-9885.

6. Mutuma, B. K.; Shao, G. N.; Kim, W. D.; Kim, H. T., Sol–gel synthesis of mesoporous anatase–brookite and anatase–brookite–rutile TiO2 nanoparticles and their photocatalytic properties. *Journal of Colloid and Interface Science* **2015,** *442*, 1-7.

7. Behnajady, M. A.; Eskandarloo, H.; Modirshahla, N.; Shokri, M., Investigation of the effect of sol–gel synthesis variables on structural and photocatalytic properties of TiO2 nanoparticles. *Desalination* **2011,** *278* (1), 10-17.

8. Montoya, I. A.; Viveros, T.; Domínguez, J. M.; Canales, L. A.; Schifter, I., On the effects of the sol-gel synthesis parameters on textural and structural characteristics of TiO2. *Catalysis Letters* **1992,** *15* (1), 207-217.

9. Kao, L.-H.; Hsu, T.-C.; Lu, H.-Y., Sol–gel synthesis and morphological control of nanocrystalline TiO2 via urea treatment. *Journal of Colloid and Interface Science* **2007,** *316* (1), 160-167.

4. Establishing Kinetic Doping in TiO_2 Thin Films with Multiple Dye Loading

4.1 Kinetically Doped TiO_2 Sol-gel Thin Films and the Primary Differences from SiO_2 Thin Films

All previous exploration of kinetic doping has utilized silica sol-gels. Even though silica (SiO_2) and titania (TiO_2) sol-gels are created through similar reaction mechanisms, it should not be surprising that the reactions based on central atoms of the metalloid silicon and transition metal titanium need to be approached differently.

The titanium dioxide sol-gel precursor, titanium isopropoxide, is extremely reactive, with the hydrolysis and condensation steps happening very quickly, requiring an acidic modifier to allow it to form a gel rather than nanoparticles aggregates. Without the presence of acid in the solution, the hydrolysis and condensation reactions will start to happen instantly in the presence of water, resulting in immediate precipitation as seen in section 3.3. The level of oligomerization is also dependent on concentration in the alcoholic solvent used, which means the ratio of precursor to ethanol will be critical. The molarity of the water in the sol-gel solution will also be critical, as the high reactivity with water means the ratio will affect the final oligomerization of the precursor molecules.[1-3]

Comparatively speaking, tetraethyl orthosilicate is less reactive – the hydrolysis and condensation reactions are much slower, and no precipitate will happen immediately without the acid in solution. As the acid is just used to catalyze the reaction and not to prevent flocculation, the acid used is much less concentrated, and the water has a much higher volumetric ratio in solution than in the titania sol-gels. This ratio is also necessary to encourage the silicon precursor to react, as the silicon center is less likely to increase its coordination than the titanium center.[1]

Based primarily on this difference in reactivity with water, many aspects of the kinetic doping process needed to be altered. While these differences caused some challenges along the way, they were all eventually overcome.

4.1.1 Preparing the Sol-Gel

In all sol-gels, the aging time is the amount of time that the reactant solution has been left to undergo hydrolysis and condensation prior to use, which results in a difference in the extent of oligomer formation at the time of spin-coating. In our recipe, how much time is required for the optimal degree of gelation prior to film creation is dependent on the amount of nitric acid catalyst present. It was clear from the beginning that the sol-gel preparation process would be a little more involved than with silica sol-gels, as the titanium isopropoxide precursor is very reactive under ambient humidity and needed to be kept in an environment without water vapor. The literature sol-gel preparations for TiO_2 sol-gels were also much more complex and involved than the general silica sol-gel preparation, where the reactants are simply mixed and left to age. Initial tests were performed using a ratio published by Nishikiori et al[4], though the ratio needed to be adjusted experimentally to result in a final solution that produced an optically clear thin film after an 18-24 hour aging time. The ultimate recipe used for this result was as follows in Table 4-1.

Table 4-1 Reagent ratio for TiO_2 sol-gel solution

Component	Amount
99.5% Ethanol	1120 μL
Titanium (IV) Isopropoxide	224 μL
70% Nitric Acid	21 μL
Millipore Water	28 μL

Each component in the recipe was added via micropipette in the order listed, mixing everything in the microtube using a vortex for 30 seconds after each addition. Solutions of up to 10× the original recipe volume were also created successfully. This TiO_2 sol-gel synthesis method is novel and efficient compared to other methods described in the literature, which require dropwise addition of the precursor under constant stirring for anywhere from 15 minutes to twelve hours.[3, 5, 6] Originally, the procedure was directly adapted from the literature and used a dropwise addition approach over the course of an hour. As the sol-gel preparation experiments continued, alterations were performed to determine if anything could be done to simplify the mixing process without causing particles to crash out in solution. Through much experimentation, it was eventually determined that as long as the reagents were added in the correct order as listed in Table 4-1 and mixed thoroughly between additions, precipitation of TiO_2 nanoparticles could be avoided without spending hours performing a dropwise addition procedure. In this process, the order the reagents are added in is critical – if the water is added before the acid, or the water and acid are already mixed into the ethanol before titanium isopropoxide is added, precipitate will crash out from the solution and render the sol-gel useless. While the recipe is very specific, the standard TiO_2 sol-gel used in this work require only five minutes of active contribution from the researcher before the aging time.

4.1.2 Dye Loading Protocols in TiO_2 Thin Films

Because the titanium isopropoxide precursor is more reactive than tetraethyl orthosilicate, it will react more quickly in ambient air. Due to this difference, the protocols for doping of silica thin films could not be directly applied to titania thin films. In silica thin films, coverslips were coated with the aged sol-gel and dropped with the nascent thin film facing up into a 50 mL beaker containing 5 mL of 1 mM dye loading solution. The beaker was then briefly shaken in a

circular motion to overcome surface tension and allow the dye solution to cover the film. The film would settle on the bottom of the beaker for the hour of loading time. When this same procedure was used for titania thin films, the irregular air-liquid interface on the surface of the film created during the swirling motion resulted in inhomogeneous loading as seen in Figure 4.1.

Figure 4.1 Image of an amorphous TiO_2 thin film loaded following SiO_2 thin film loading protocol

The slow immersion process used for silica thin films was obviously not going to produce consistent, optical-quality TiO_2 thin films. Attempts were made to float the coverslips on the surface of the dye solution with the thin films facing down, but the results were inconsistent and prone to producing substandard films. Often air bubbles would be trapped between the dye solution and the coverslip, resulting in spots the shape of the air bubble with no dye loading. For films that did not end up with air bubbles, the coverslip often sank in the beaker due to unanticipated disturbances, destroying the fragile film on the bottom of the beaker.

What the TiO_2 thin films really needed was a way to enter the dye solution rapidly, limiting the time available for the undesirable air-liquid interface reaction. This was solved by reorienting the film vertically to reduce the resistance of the surface tension. Instead of positioning the thin films horizontally in a 50 mL beaker, films were dropped vertically into a 20 mL beaker filled with

solution and allowed to load while resting at an angle. This method proved successful at limiting the presence of any air-liquid interface on the surface of the film. The difference in these two immersion methods is illustrated using pieces of colored paper of approximately the same size as coverslips for a visual reference in Figure 4.2.

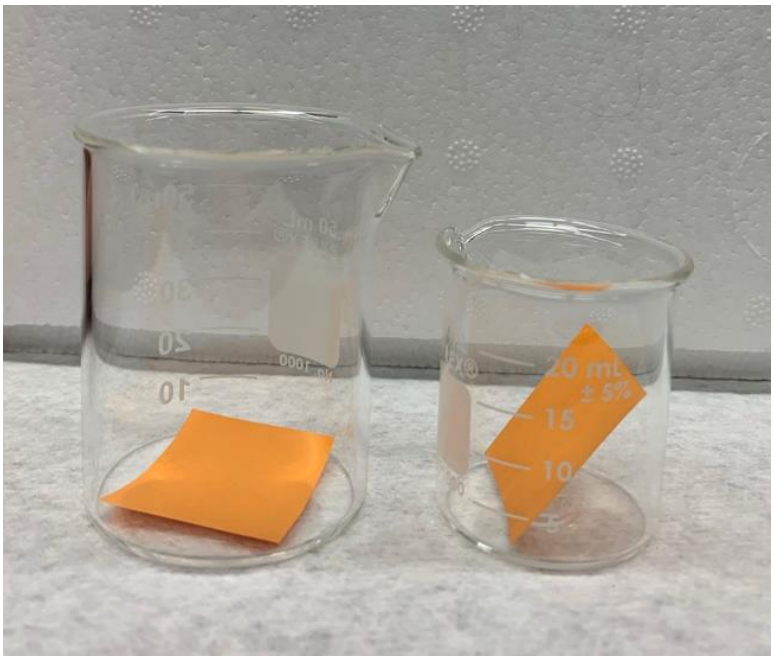

Figure 4.2 Difference in loading position between SiO_2 thin films (left) and TiO_2 thin films (right).

During experimentation, a small percentage of samples would get caught on the beaker if dropped at an incorrect angle. When this occurred, it consistently left a clean line break across the film, exemplifying the detrimental effect of the air-liquid interface in TiO_2 kinetic doping. An example of this defect is shown in Figure 4.3. Samples with known defects of this type were not used for quantitative analysis.

Figure 4.3 Example break in thin film caused by an extended moment of liquid-air interface

4.1.3 Effects of Ambient Humidity on Thin Films

Due to the known effect of ambient humidity while spin-coating that was discovered in silica-based thin films[7], attempts were initially made to control the humidity of the spin-coating chamber while the TiO_2 thin films were being spun. This was accomplished by pumping air at a set relative humidity of 50% into the spin chamber. When the films were spun using this method, the sudden change of humidity caused the thin films to crack as the films were removed from the humidity-controlled spin-coating chamber to open air before transferring to the dye loading solution. To eliminate the shock of sudden humidity change, it was determined that all TiO_2 thin films would be prepared in open air under ambient conditions.

Through kinetic doping experiments performed at recorded open-air humidity levels, it was established that for all humidity levels between 0-50% RH, most films produced were optically clear and mechanically stable.

4.1.4 Determination of Optimal Post Spin-Coat Delay

The post spin-coat delay is defined as the time between the end of spin-coating and immersing the film in a dye loading solution. Depending on the humidity, dye loading efficiency in SiO_2 thin films were strongly influenced by post spin-coat delays needed to ensure the mechanical stability of the film.[7] After the experience with SiO_2 thin films, it was uncertain as to how the TiO_2 sol-gel's higher reactivity would affect the need for a post spin-coat delay. Therefore, TiO_2 thin films were spun from aged sol-gel and allowed to set under different ambient conditions for various post spin-coat delays to establish the best delay for doping in titania films. A representative set of samples at 38% humidity is displayed Figure 4.4.

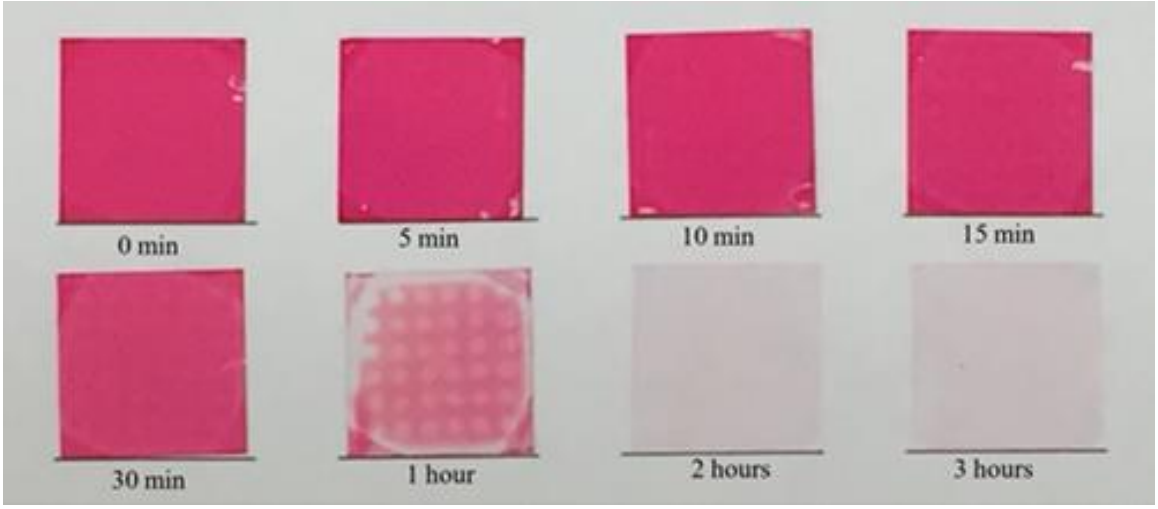

Figure 4.4 Visually apparent loading of R6G in TiO_2 thin films with varied post spin-coat delay at 38% humidity

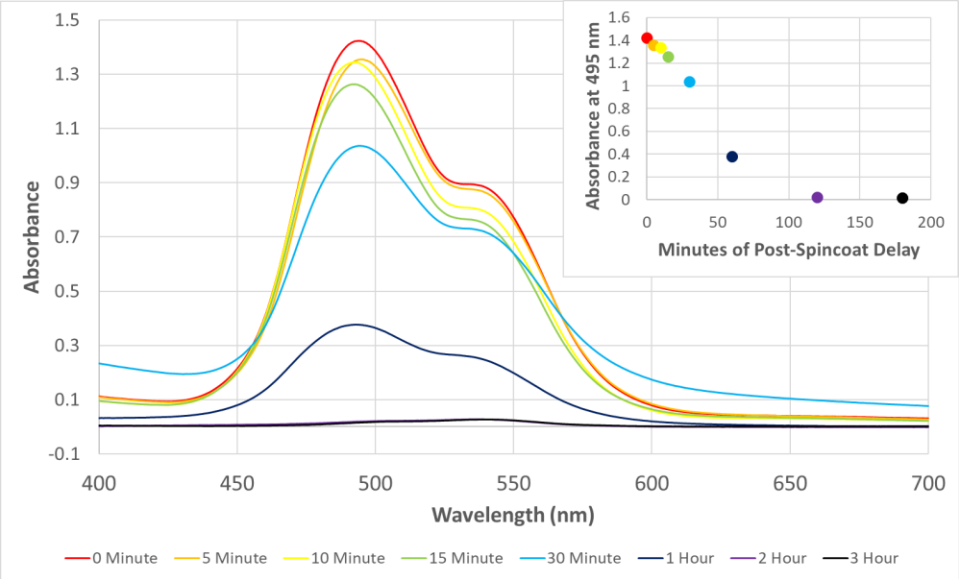

Figure 4.5 UV-Vis absorption spectra of R6G-doped TiO_2 thin films with various post spin-coat delays at 38% humidity. Inset graph contains absorbance at 495 nm vs. minutes of post spin-coat delay

Figure 4.5 displays the UV-Vis absorption spectra of the same films shown in Figure 4.4, and the inset reveals the general trend for kinetic doping of R6G in titania thin films. Films with zero post spin-coat delay consistently resulted in the highest R6G loading efficiency, whereas final dye concentration decreased steadily with increasing post spin coat delay time. This trend is consistent with our current understanding of kinetic doping. As the nascent film is given more time to condense in open air before immersing in the loading solution, the film will be in an increasingly matured stage and therefore less capable of dye loading. Based on the current model of kinetic doping, more dye will be trapped in the portion of the film that is still actively evolving when it is introduced to the loading solution. As a 0-minute post spin-coat delay continued to produce films with the highest absorbance regardless of humidity, all other experiments were performed using a 0-minute post spin-coat delay.

4.1.5 Phosphate Buffer Dependence

Previous work in our lab has established that the phosphate buffer is not required in kinetic doping of sol-gel silica film; and is used with silica films mainly to maintain a consistent neutral doping pH. After determining that unlike with silica thin films, TiO_2 thin films were not mechanically stable in pure water, experiments were performed to see whether it was the presence of phosphate buffer specifically that allowed stable kinetic doping, or the presence of ions in general. To determine whether TiO_2 thin films could be loaded in ionic solution without phosphate buffer, 1 mM R6G loading solutions in both 10 mM phosphate buffer and 10 mM NaCl were prepared at a range of pH values to compare the loading and mechanical stability of the resultant films.

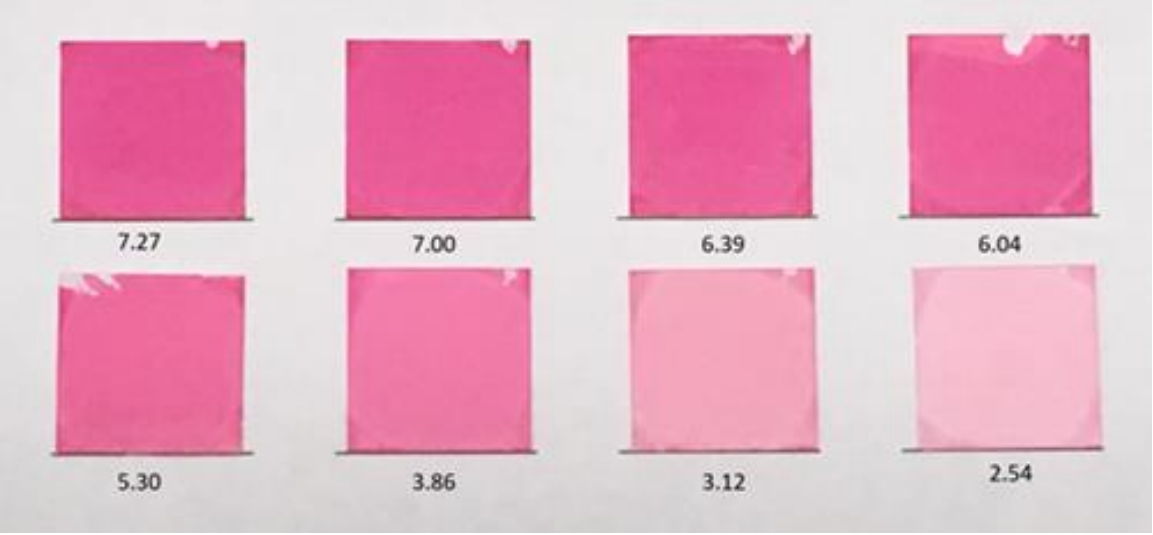

Figure 4.6 TiO_2 thin films loaded with 1 mM R6G in 10 mM phosphate buffer at 0-minute post spin-coat delay at varied pH

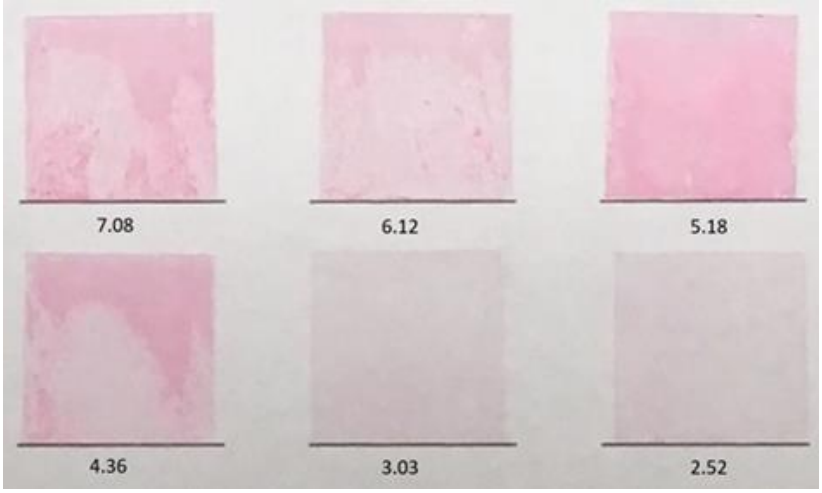

Figure 4.7 TiO_2 Thin Films Loaded with 1 mM R6G in 10 mM NaCl at 0 Minute Post Spin-Coat Delay at Varied pH

Figure 4.6 demonstrates that the films prepared in 10 mM phosphate buffer loading solution were mechanically stable and all successfully load R6G, though the amount loaded decreased with decreasing pH. The films prepared in 10 mM NaCl solution, displayed in Figure 4.7, were not mechanically stable at pH 4.36 or above. Even though the films at pH 3.03 and below appear stable, they display even less loading than the unstable films from the NaCl solutions at higher pH levels.

A brief experiment was also performed in Millipore water alone, illustrating that the ions are not responsible for the lackluster doping of films. As displayed in Figure 4.8, even at higher concentrations of R6G, the thin films only kinetically dope well with the presence of the phosphate buffer. The two films in the top left corner of this image are a film doped in 10 mM phosphate buffer and a film doped in pure water. While this cannot be seen very clearly in the figure as TiO_2 film without dye is optically transparent, neither of these films were mechanically stable. While the film in the phosphate buffer was more stable than a film left in pure Millipore water, approximately half of the samples tested in 10 mM phosphate buffer without dye present

broke apart during the rinsing and drying process. The film in 10 mM phosphate buffer with 1 mM R6G was mechanically stable and well-loaded. None of the films loaded in dye solution without the phosphate buffer loaded well. While there was a slight increase in loading and stability with increasing R6G concentration, even the 10 mM R6G displayed low, inhomogeneous dye loading. Since attempts to load film "blanks" in 10 mM phosphate buffer without dye resulted in less stable TiO_2 thin films, the working hypothesis is that the dyes and the phosphate buffer both help strengthen the film. This synergistic effect between the dopant and the sol-gel matrix appears to be less critical in SiO_2 thin films, perhaps because the silica sol-gel is less prone to flocculation.

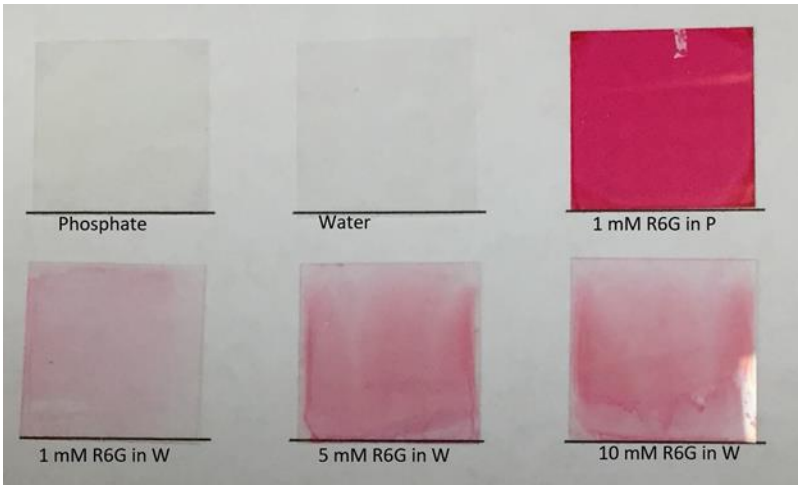

Figure 4.8 TiO_2 thin films loaded in phosphate buffer and TiO_2 thin films loaded in aqueous solution with varying concentrations of R6G. "in P" stands for in 10 mM phosphate buffer, while "in W" stands for in Millipore water.

This experiment demonstrated that the presence of the phosphate buffer is critical to kinetic doping in titania films. In view of this, all subsequent doping was performed in 10 mM phosphate buffer.

4.2 Individual Dye Loading Summary

The primary dye used to determine kinetic doping parameters is Rhodamine 6G (R6G). After kinetic doping parameters were established, experiments to load Auramine O (AO), Fluorescein, Eosin B, Bromophenol Blue, Tris(2,2'-bipyridyl)dichlororuthenium(II) Hexahydrate (Ru2), Rhodamine B, and Nile Blue were also performed.

Quantification of R6G concentration in TiO_2 thin films was done by assessing the H-type dimer peak at approximately 490 nm and the monomer/J-type dimer peak at approximately 541 nm. Because the monomer and J-type dimer peaks overlap[8], all concentration calculations are based on the assumption that the 541 nm peak is entirely from the monomer. Assuming that some J-type dimer is likely present, this should result in calculating the minimum concentration of R6G in the thin film. To allow a more accurate estimate on individual peak intensity, UV-Vis spectra were deconvoluted into separate Gaussian peak components that correspond to the monomer and H-type dimer. The literature molar extinction coefficient used to calculate the concentration of the monomer peak was 78000 $cm^{-1}M^{-1}$, and for the H-type dimer peak was 94000 $cm^{-1}M^{-1}$.[9]

Quantification of Ru2 concentration was done using the strongest absorption peak at 460 nm. The literature molar extinction coefficient of 13,700 $cm^{-1}M^{-1}$ at 460 nm, was used to calculate the overall concentration.[10]

AO doped in TiO_2 films had a distinctly different absorption spectrum when compared to the spectrum of AO in a free solvent. Due to this anomaly, it is obvious that the extinction coefficient of AO in a free solvent cannot be used to estimate its concentration in a TiO_2 film. Instead of measuring absorbance directly from thin films, ethanol was used to extract as much AO as possible from the thin film after four days of extraction. A Beer's law plot for AO in

ethanol was created using the strongest absorption peak at 430 nm for four known concentrations, allowing for the determination of the molar extinction coefficient in ethanol at 41,000 $cm^{-1}M^{-1}$.

Due to either poor loading efficiency or mechanical stability, concentration of fluorescein, eosin B, rhodamine B, bromophenol blue, and Nile blue in TiO2 film was not individually quantified.

4.2.1 Rhodamine 6G (R6G)

The primary dye used for the development of parameters for kinetic doping in titania thin films is R6G, the structure of which is shown in Figure 4.9. There are several benefits to beginning with this dye, apart from it being one of the dyes with established success in kinetic doping in silica thin films[7]. Firstly, R6G is positively charged at or above a neutral pH, which is a characteristic consistent with the previous dopants that have demonstrated successful kinetic doping. Secondly, the molar extinction coefficient of R6G is very high, resulting in high light absorption. This had a side benefit of allowing for rapid qualitative assessment of successful loading in thin films. Finally, while far from being the most efficient dye for DSSC applications, R6G has proven to successfully inject electrons into the semiconductor anode in reported literature[11].

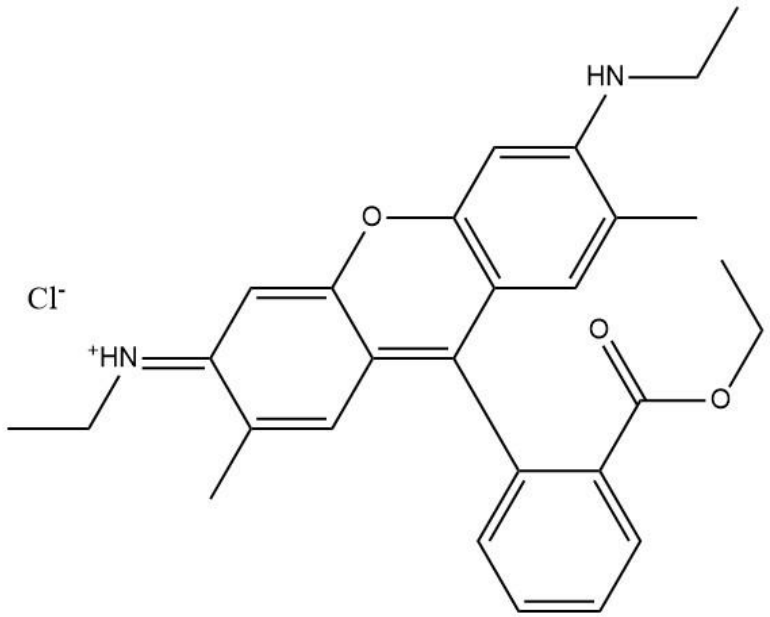

Figure 4.9 Structure of R6G above pH 7.0

Utilizing 6 replicates at a 0-minute post spin-coat delay, the average of the UV-Vis absorption spectra of films was taken and deconvoluted into two gaussian peaks (Figure 4.10) to estimate the concentration of R6G molecules within the thin film. Both peaks were allowed to float to accommodate the possibility of minor peak shifts from different films. With this regard, the H-type dimer peak is allowed to float around 500 nm and the monomer/J-type dimer peak was allowed to float around 530 nm. Since the absorption peak of the monomer and that of the J-type dimer overlap and are therefore indistinguishable in this experiment, all absorption at 530 nm will be processed as though the peak is entirely attributed to the monomer. This assumption is made to avoid overstating the increase in concentration made possible by using the kinetic doping method. The black line in Figure 4.10 is the experimental average spectrum, the navy line is the gaussian peak associated with the H-type dimer, the light blue line is the gaussian peak associated with the monomer, and the red line is theoretical spectrum generated from the sum of the two gaussian peaks. Deconvolution was performed from 450 – 700 nm.

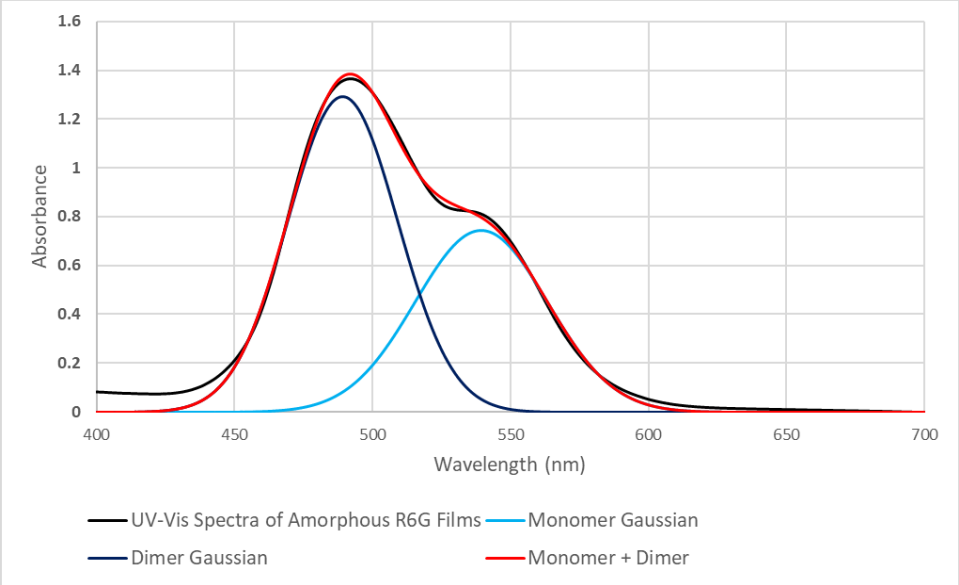

Figure 4.10 Average UV-Vis absorption spectra of 6 single-layer TiO_2 thin films loaded with R6G at 0-minute post spin-coat delay.

Multiple SEM images were taken at 50,000× magnification to determine an average thickness using the cross section of a given amorphous R6G loaded thin film at different areas of the sample. An example of the SEM images taken is included below in Figure 4.11. This and other similar SEM images were used to determine the average thickness of amorphous R6G loaded thin films to be 250 ± 30 nm.

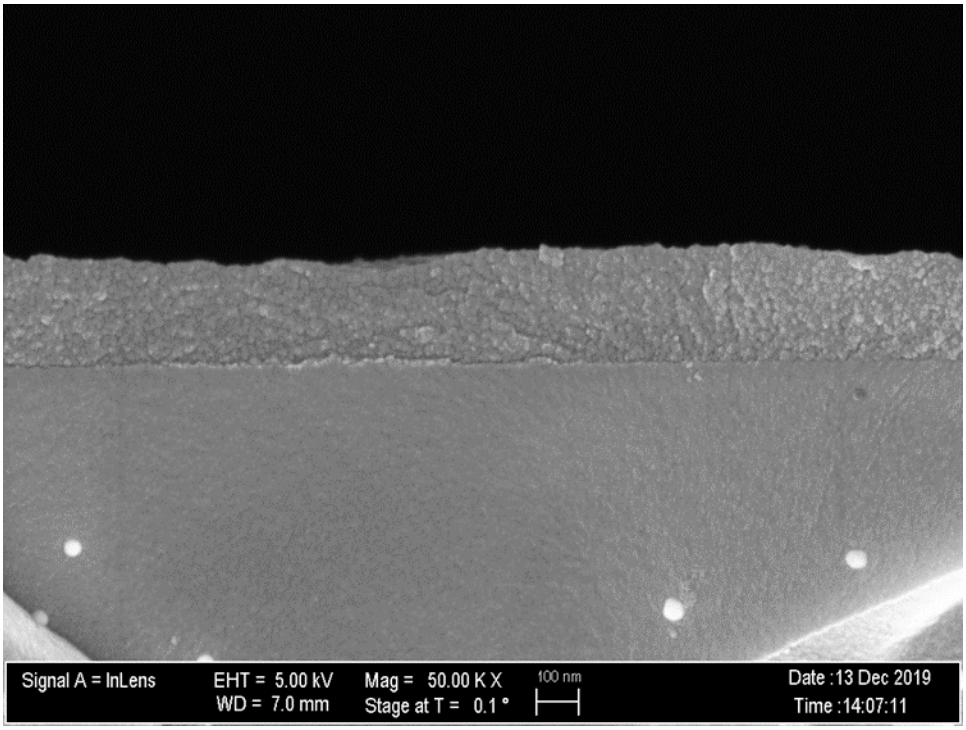

Figure 4.11 SEM image of R6G loaded amorphous TiO_2 thin film

Table 4-2 Summary of data used to calculate the concentration of R6G in individual amorphous TiO_2 thin films.

Monomer Peak Values		Dimer Peak Values	
$\lambda_{monomer}$	539.4 nm	$\lambda_{H\text{-type dimer}}$	489.2 nm
$A_{monomer}$	0.74 ± 0.02	$A_{H\text{-type dimer}}$	1.29 ± 0.03
$\varepsilon_{monomer\ (531)}$[9]	78000 ± 1000 $cm^{-1}M^{-1}$	$\varepsilon_{H\text{-type dimer}(500)}$[9]	94000 ± 1000 $cm^{-1}M^{-1}$
b	250 ± 30 nm		

Utilizing Beer's law and the deconvoluted absorption spectrum, the concentration of R6G was then determined. Using the individual peak information summarized in Table 4-2, and average thickness of the films from the SEM images, concentration of R6G in an amorphous titania film at a post spin-coat delay of 0 minutes is estimated to be 1.5 ± 0.1 M, approximately 1500× the

concentration of the initial 1 mM loading solution and 15-20× the concentration achievable by other traditional loading methods.

$$c_{monomer} = \frac{A}{\varepsilon b} = \frac{0.74}{(78000\ M^{-1}cm^{-1})(2.50 * 10^{-5}cm)} = 0.38\ \pm 0.05\ M$$

$$c_{dimer} = \frac{A}{\varepsilon b} = \frac{1.29}{(94000\ M^{-1}cm^{-1})(2.50 * 10^{-5}cm)} = 0.55 \pm 0.07\ M$$

$$c_{total} = c_{monomer} + 2c_{dimer} = 0.38\ M + 2(0.55\ M) = 1.5\ \pm 0.1\ M$$

Again, since the monomer absorbance and J-type dimer absorbance are indistinguishable at 530 nm, this estimate assumes that the peak around 530 nm is entirely attributed to monomer absorption. Therefore, the number calculated here represents the minimum concentration present in the thin film. The actual R6G concentration may be higher.

4.2.2 Auramine O

While primarily used as a fluorescent bacterial stain, AO was marked as a possible alternative guest molecule based on its high molar extinction coefficient and its positive charge at neutral or high pH.[12] AO was also selected as a secondary dye based on its absorbance in a different section of the solar spectrum from R6G. Assuming it could be kinetically doped, co-loading both dyes would expand the bandwidth of light absorbed by the thin film. Though AO is not commonly used as a photosensitizer in dye-sensitized solar cells, it is not entirely unprecedented.[13] The structure of AO is shown in Figure 4.12.

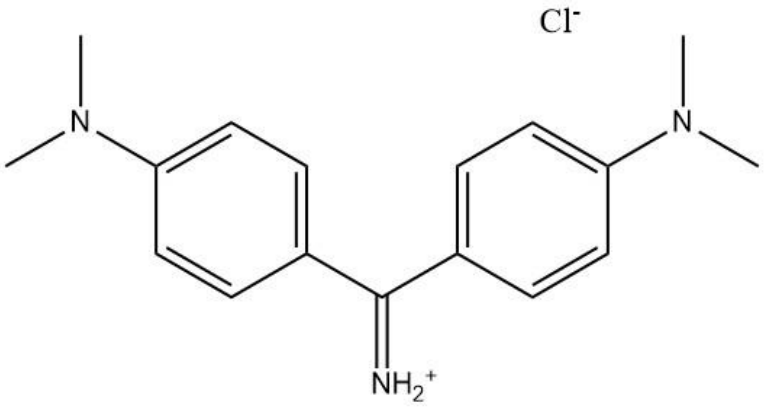

Figure 4.12 Structure of Auramine O

AO immediately loaded favorably under kinetic doping conditions with a solution of 1 mM AO in 10 mM phosphate buffer solution at pH 7.3, practically identical to the conditions originally developed for R6G. The films were slightly less mechanically stable than the R6G loaded thin films. Due to this slight instability, purge drying needed to be performed more gently in order to protect the films. Otherwise, the loading conditions were identical. An image of three identically prepared AO-doped thin films is displayed in Figure 4.13.

Figure 4.13 Image of 3 replicate AO-doped TiO_2 thin films

While the loading method was nearly identical, the method of measuring the concentration in the thin film needed to be adjusted. The UV-Vis absorption peaks of AO in the solid film, shown in

Figure 4.14, exhibit a significant blue shift compared to the spectra of AO in various liquid solvents.

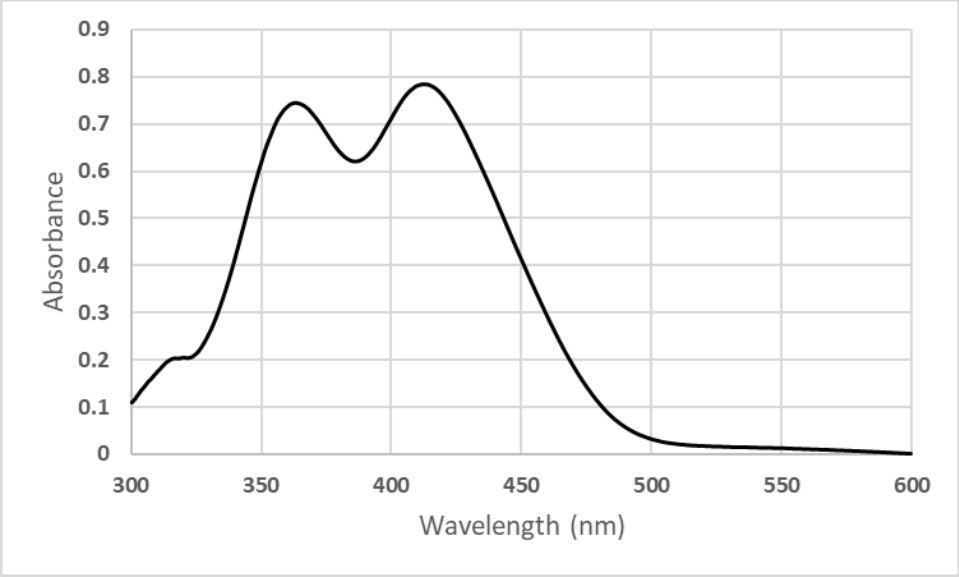

Figure 4.14 Average UV-Vis absorption spectra of 6 AO-doped TiO_2 thin films

This blue shift meant the concentration could not be confidently determined using the absorbance measured directly from the film. To circumvent this restriction, as much AO as possible was extracted from the kinetically doped thin films into ethanol over the course of four days. A Beer's law plot was created using four known concentrations of Auramine O in ethanol to determine the exact molar extinction coefficient of 41,000 $\frac{1}{Mcm}$ at 430 nm used in this work. The data used to establish this molar extinction coefficient is displayed in Figures 4.15-4.16.

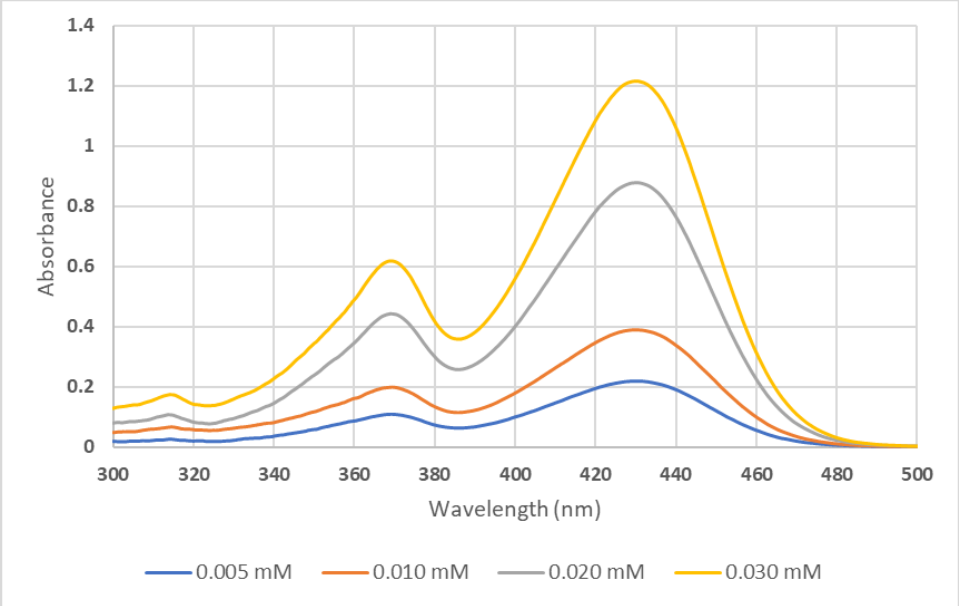

Figure 4.15 UV-Vis absorption spectra of AO in ethanol at various concentrations

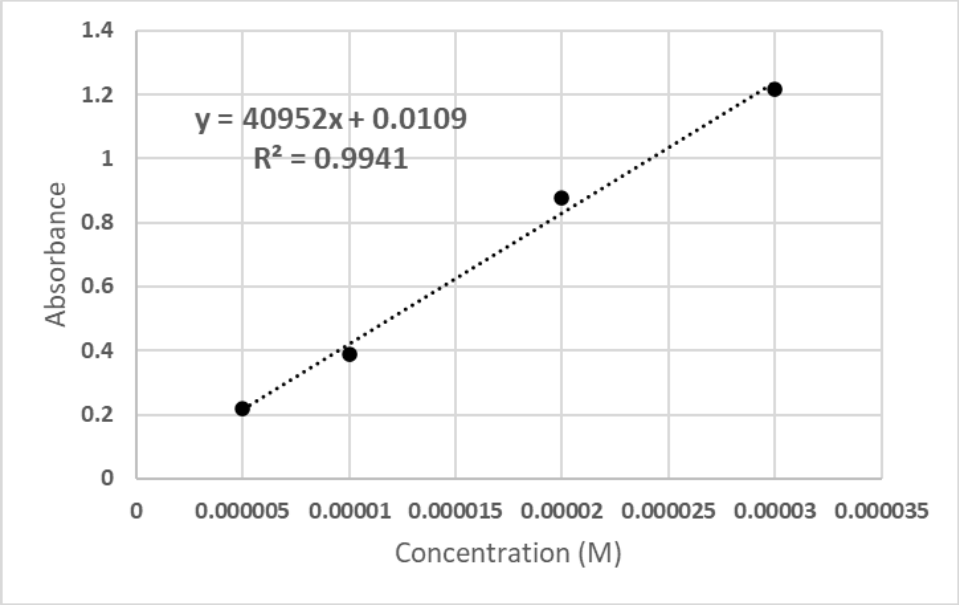

Figure 4.16 Absorbance of AO in ethanol at 430 nm vs. concentration

Individual single-layer films loaded with AO were each placed in 12.0 mL of ethanol to extract the dye from the film for four days. After dye extraction, the average absorbance of the dye extraction solution was measured. This UV-Vis spectrum is displayed in Figure 4.17.

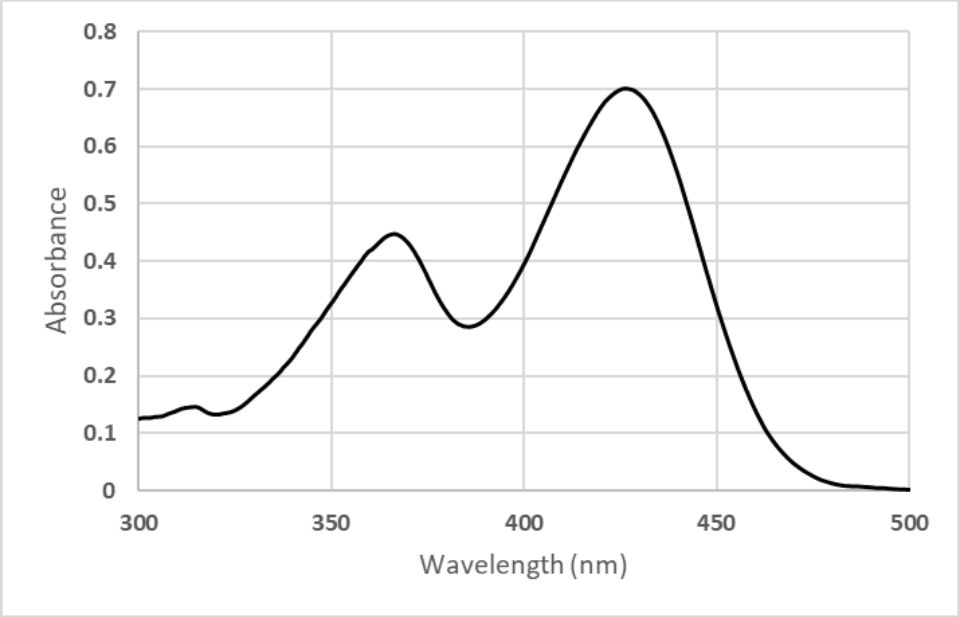

Figure 4.17 Average absorption spectrum of the 12 mL ethanol solution after four days of dye extraction from an AO-doped TiO_2 thin film.

Once the AO was extracted from the thin film into ethanol, it was possible to back-calculate the concentration in the film based on the measurable concentration in the solution and the known volumes of the solution and the film. The volume of the film was calculated from the SEM-measured average thickness of 170 nm and surface area of 625 mm^2.

Table 4-3 Summary of the values needed to determine AO concentration in individual amorphous TiO_2 thin films

λ	430 nm
$A_{430\ nm}$	0.69 ± 0.02
$\varepsilon_{430\ nm}$	41,000 ± 2,000 $cm^{-1}M^{-1}$
b	1.00 ± 0.01 cm
V_{ext}	12.0 ± 0.3 mL
V_{film}	1.1 ± 0.1 * 10^{-4} cm^3

$$c_{ext} = \frac{A}{\varepsilon b} = \frac{0.69}{(1\ cm)\left(41000\ \frac{1}{Mcm}\right)} = 1.7\ \pm 0.1 *\ 10^{-5}\ M$$

$$c_{film} = \frac{c_{ext}V_{ext}}{V_{film}} = \frac{(1.68 *\ 10^{-5}\ M)(12.0\ cm^3)}{1.1 * 10^{-4} cm^3} = 1.9\ \pm 0.2\ M$$

At 1.9 M, AO has the highest concentration of any dye successfully loaded into amorphous TiO_2 thin films. This does logically align with the knowledge that it is the smallest of the dyes loaded. If the pores are approximately the same size across the amorphous TiO_2 thin films, which they ought to be, more of the smaller dye will fit within the space that accommodates the larger dyes.

4.2.3 Tris(2,2'-bipyridyl)dichlororuthenium(II) hexahydrate (Ru2)

Tris(2,2'-bipyridyl)dichlororuthenium(II) hexahydrate (Ru2) was selected as a solar cell test dye due to its slightly richer history of use in dye sensitized solar cell literature[14] compared to the others, and some previous success in the ability to kinetically dope it to silica thin films. Successful kinetic doping of this ruthenium dye would perhaps also provide a precedent for the kinetic doping of the more complex ruthenium-based dyes that are popular for their higher efficiency, such as N3 or N719[15-19]. Figure 4.18 shows the general structure of the dye. Like AO and R6G, Ru2 is positively charged, though it has a +2 charge instead of an overall +1 charge.

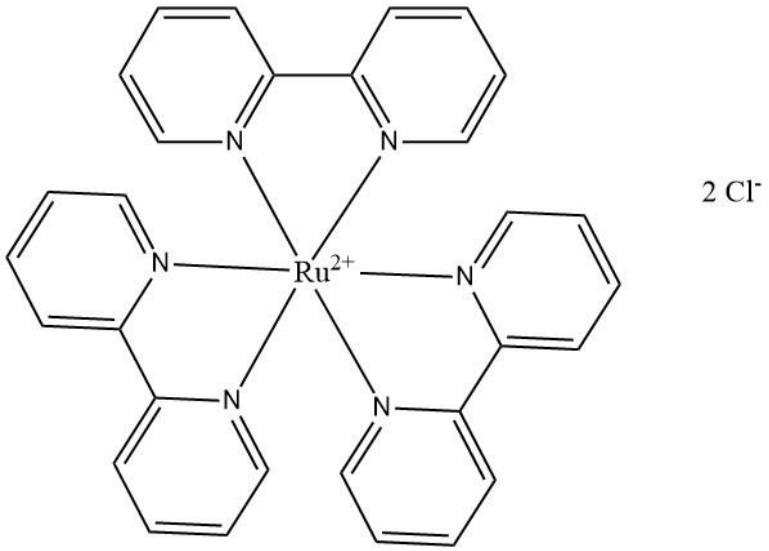

Figure 4.18 Structure of tris(2,2'-bipyridyl)dichlororuthenium(II) hexahydrate (Ru2)

At the pH 7.3 loading conditions that work well for AO and R6G, the resultant kinetically loaded films were unable to withstand the rinsing and drying process for loaded films described in section 3.7. Replicates of these mechanically compromised Ru2-doped thin films are shown in Figure 4.19.

Figure 4.19 Replicate TiO_2 thin films doped with Ru2 at pH 7.3 at 0-minute post spin-coat delay

While this dye is larger and contains more aromatic rings than R6G and AO, the prior experience with silica thin films has established that the size of the dopant is not expected to play a significant role in the mechanical stability of the sol-gel film matrix. Kinetic doping experiments

with silica thin films done by Crosley and Jensen have proven that large proteins[20-22] or branched polyethylamines[23] can be doped kinetically without weakening the structural integrity of the film. It is unsure at this time what specifically caused the Ru2-doped thin films to be less mechanically stable than the others under identical loading conditions.

Even with this lack of stability, Ru2 did display significant loading using the kinetic doping method. Knowing that previous tests done with R6G had demonstrated an even greater mechanical stability when doped at higher pH levels, the Ru2 loading solution was adjusted from pH 7.3 to 8.9. This adjustment increased the mechanical stability of the thin films sufficiently to produce films of consistent optical quality and homogeneous loading as shown in Figure 4.20.

Figure 4.20 Replicates of TiO_2 thin films doped with Ru2 at pH 8.9 at 0-minute post spin-coat delay

While more stable than those loaded at pH 7.3, these films still require a gentler rinsing and purge drying process than the highly stable R6G loaded films in order to prevent cracking of the thin film. Thus, the coverslips need to be moved through the rinse solutions slowly, and the purge drying direction absolutely must be perpendicular to the film until the film is set upon drying. If the air flow is parallel to the film, the film will peel off from the coverslip and break. Moreover, the purge drying process is far more likely to result in a useable thin film if the air

flow rate is low, rather than the high air flow rate that R6G loaded thin films can tolerate. The average UV-Vis spectrum of replicate Ru2 films loaded at pH 8.9 is displayed in Figure 4.21

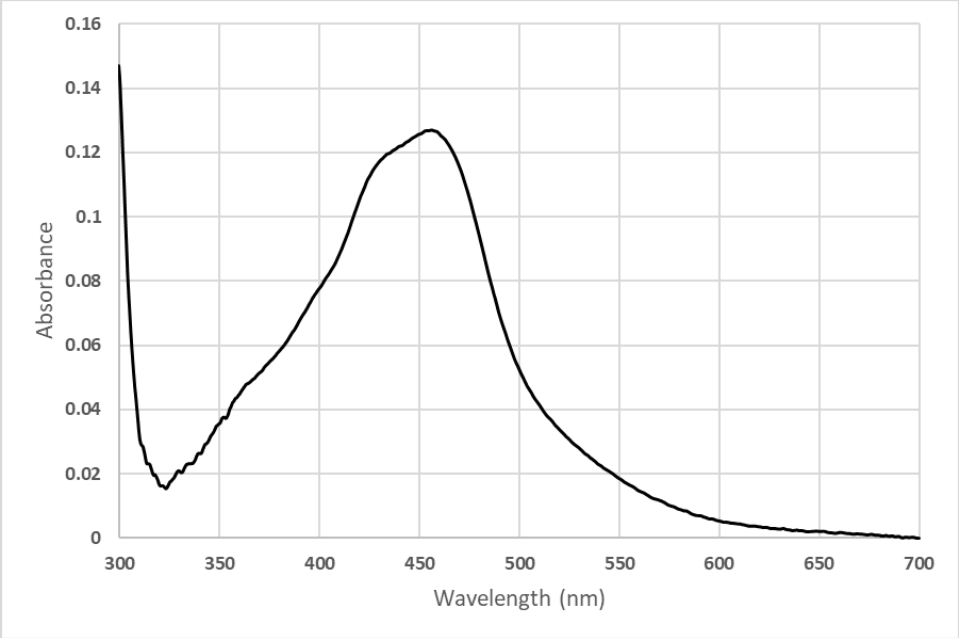

Figure 4.21 Average absorption spectrum of 3 Ru2-doped amorphous TiO_2 thin films

The absorbance measured in the TiO_2 thin films loaded with Ru2 is clearly much lower than either the primary absorbance peak in AO or the peaks in R6G. This is not truly a cause for concern of poor loading, as the molar extinction coefficient for Ru2 at 460 nm is 13,700 $\frac{1}{Mcm}$, about a third of the extinction coefficient for AO. The SEM imaging also confirmed that the loaded amorphous film containing Ru2 is significantly thinner than the other amorphous loaded films, measuring at 129 nm instead of 250 nm for R6G or 170 nm for AO. Since we are comparing the concentration of loaded dye within the film, the absorbance and thickness of the film are merely factors used to calculate that concentration and not of individual concern.

Table 4-4 Summary of data used to calculate the concentration of Ru2 in individual amorphous TiO_2 thin films

λ	460 nm
$A_{456.5}$	0.135 ± 0.002
$\varepsilon_{460\ nm}$[10]	13,700 ± 100 $cm^{-1}M^{-1}$
b	129 ± 8 nm

$$c = \frac{A}{\varepsilon b} = \frac{0.135}{(13{,}700)(1.29 * 10^{-5})} = 0.76 \pm 0.05\ M$$

After calculating the concentration of Ru2 in the 129 nm amorphous films, as shown above, Ru2 proved to load at concentrations about half that of R6G, and slightly less than half than the concentration of AO. Again, when comparing the sizes of the dye molecules loaded, this moderately smaller concentration makes sense.

4.2.4 Fluorescein, Bromophenol Blue, Eosin B, and Rhodamine B

Attempts were made to load other dyes such as Rhodamine B, Fluorescein, Eosin B, Bromophenol blue. Regardless of the loading parameters attempted for these dyes, kinetic doping could not be achieved. While the exact reason these dyes resist kinetic doping has not been determined, some experimentation and examination of the dye structures has allowed for the formation of educated hypotheses. The structures of these four molecules are displayed in Figure 4.22, and the hypotheses will be expanded on below.

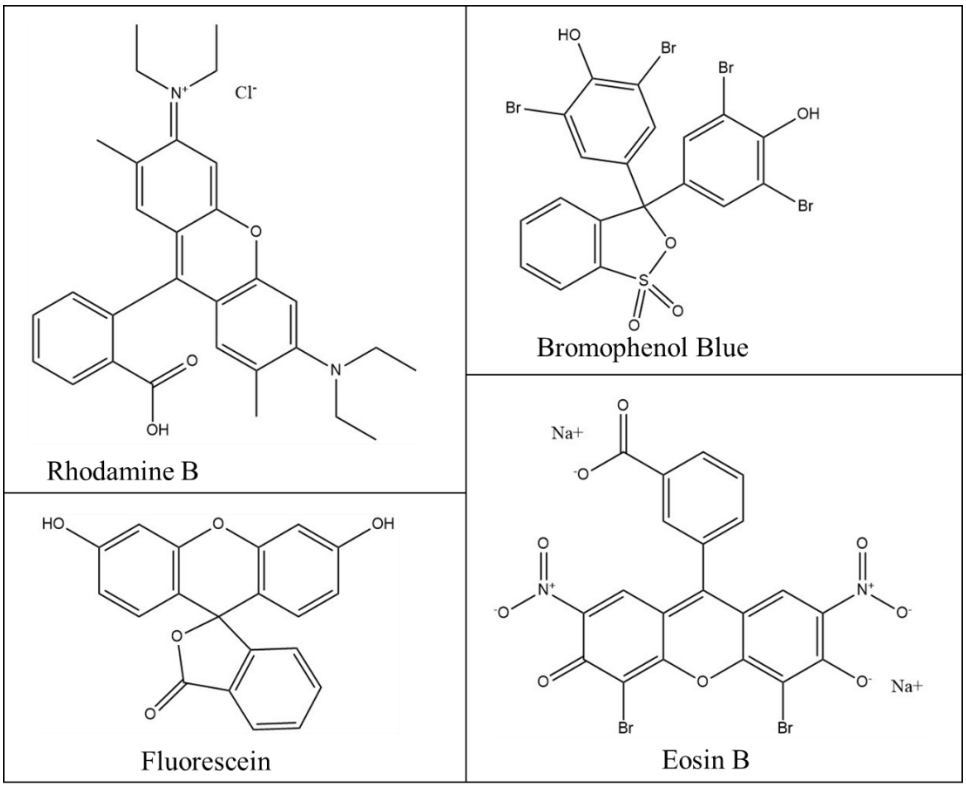

Figure 4.22 Structures of dyes which resist kinetic doping (rhodamine B, fluorescein, bromophenol blue, and eosin b)

Eosin B is perhaps the molecule with the easiest explanation. It is a zwitterion with an overall -2 charge. Even in the silica kinetic doping experiments performed, molecules with an overall negative charge do not load well. These negative charges may well prevent eosin B from being drawn into the evolving film matrix in the same manner as positively charged molecules. Fluorescein and bromophenol blue are neutral at low pH, and almost certainly negatively charged at the slightly basic pH generally used for kinetic doping – while it was disappointing that they could not be loaded into TiO_2 thin films, especially as fluorescein has a very high molar extinction coefficient, it is not overly surprising for the same reasons we expect Eosin B would not load. Since there are a few tests that indicate kinetic doping is possible (though lower) at a more acidic pH, attempts to load fluorescein at a slightly acidic pH may prove fruitful.

The fourth dye that will not load is Rhodamine B. Exactly why this dye would not load is still not certain, as it is very close in structure to R6G and had previously loaded well in kinetically doped SiO_2 thin films. While it is possible that the slightly basic pH of the loading solution would deprotonate the carboxyl group and leave the molecule a neutral zwitterion, a test was performed to determine whether rhodamine B loaded at pH 6.6 or 5.8 and did not result in significant loading at either acidic pH. If the rhodamine B is in the neutral zwitterionic form, it may be that the positive charge is simply more necessary in kinetic loading in TiO_2 than in SiO_2.

So far, the majority of guest molecules loaded into either silica or titania contain iminium ions, the most obvious exception here being Ru2, a positively charged heavy metal chelated with bipyridine. While the presence of an iminium ion does not guarantee loading, as exemplified by rhodamine B's resistance to loading, it does provide a more specific place to start with other dyes, rather than testing any and all positively charged water soluble dyes to see what may work.

4.2.5 Nile Blue Chloride

With this knowledge, Nile blue chloride was selected as a dye that may possibly load well using the kinetic doping method. Nile blue is a positively charged dye that contains both an amine and an iminium ion. Based on that structure, displayed in Figure 4.23, it would support our current hypothesis if this dye displays significant loading. As Nile blue also has a high molar extinction coefficient with the maximum absorbance at a wavelength of 627.5 nm, it would also absorb in a distinct area of visible light from the dyes that have previously loaded successfully. Like AO and R6G, it is most commonly used as a fluorescent biological stain; but has been used in the recent past as a photosensitizer in dye sensitized solar cells.[24, 25]

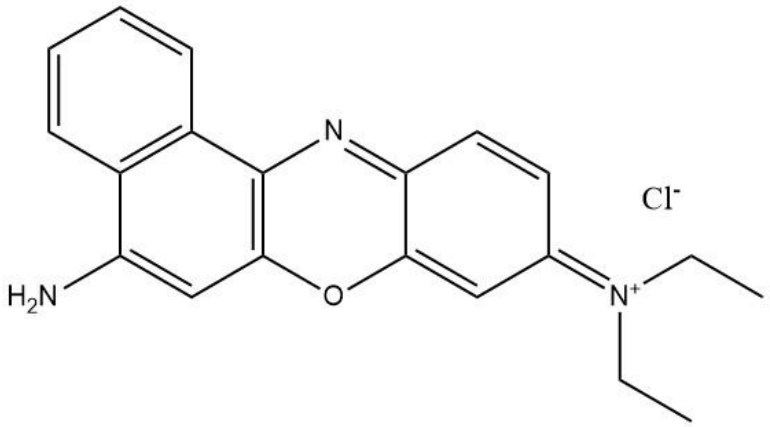

Figure 4.23 Structure of Nile blue chloride

Gratifyingly, the results of attempts to load Nile blue seem to affirm the hypothesis. When dye loading solutions were at pH 7.3, the TiO_2 thin films had clearly loaded dye, but were even less mechanically stable than the Ru2 loaded thin films. Raising the loading solution pH to 8.9 resulted in an optically clear film that was mechanically stable enough for a film to mostly survive the rinsing and drying process. Replicates of these films are displayed in Figure 4.24.

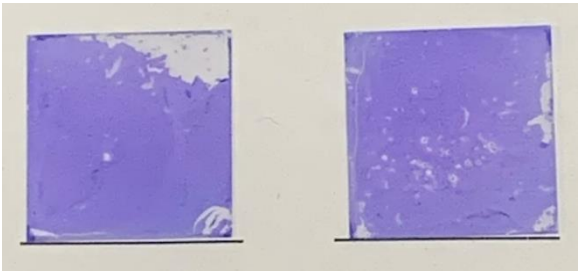

Figure 4.24 Replicate films doped with Nile blue at pH 8.9 with 0-minute post spin-coat delay

At this time, films kinetically doped with Nile blue are not consistently mechanically stable enough to fully quantify the concentration within the film. To measure the concentration in individually doped films, the pH of the loading solution may need to be increased further for sufficient mechanical stability.

4.3 One-Pot Multiple Dye Loading

DSSCs are more effective when they can utilize a wider bandwidth of the solar spectrum – the wider the range of photon absorption, the more energy the material can absorb, since the solar spectrum and irradiance power remain constant. A popular method to accomplish this is to load multiple dyes at once.[26-28] In section 4.2, it was established that we could kinetically load several dyes individually in TiO_2 thin films. In previous work, our lab has demonstrated that it is possible to co-load multiple enzymes in a single step using kinetic doping in silica thin films.[21] Assuming this one-pot loading process will produce similar results with dyes in TiO_2 thin films, cosensitization of our semiconductor material should be rather straightforward.

4.3.1 Dual Dye Loading

Dual dye loading solutions of 1 mM total dye (0.5 mM of each dye) at pH 7.3 were created using combinations of the three dyes that loaded into a mechanically stable film individually. For all spectra presented in this section, the black line represents the actual average UV-Vis spectrum for the loaded films, and the red line represents the summation of individual peaks obtained from a gaussian deconvolution of the average UV-Vis spectrum.

The deconvolution of the UV-Vis spectrum for films containing a mixture of R6G and AO is displayed in Figure 4.25. Deconvolution was performed from 330 – 700 nm. The spectrum displays clear peaks in the expected general range for AO trapped within a film, at 352 nm and 408 nm, if slightly blue shifted from the 359 nm and 420 nm peaks present when AO alone was loaded in TiO_2 films. The R6G peaks also display strongly, though with a slight red shift at approximately 502 nm and 546 nm instead of at approximately 490 nm and 540 nm. In order to best-match the actual absorption spectrum with the theoretical spectrum, a broad gaussian background centered around 460 nm was required. The addition of this broad background near

460 nm was necessary to achieve satisfactory fitting to the experimental spectra for all films with multiple dyes, although the physical origin of this broad background remained unclear.

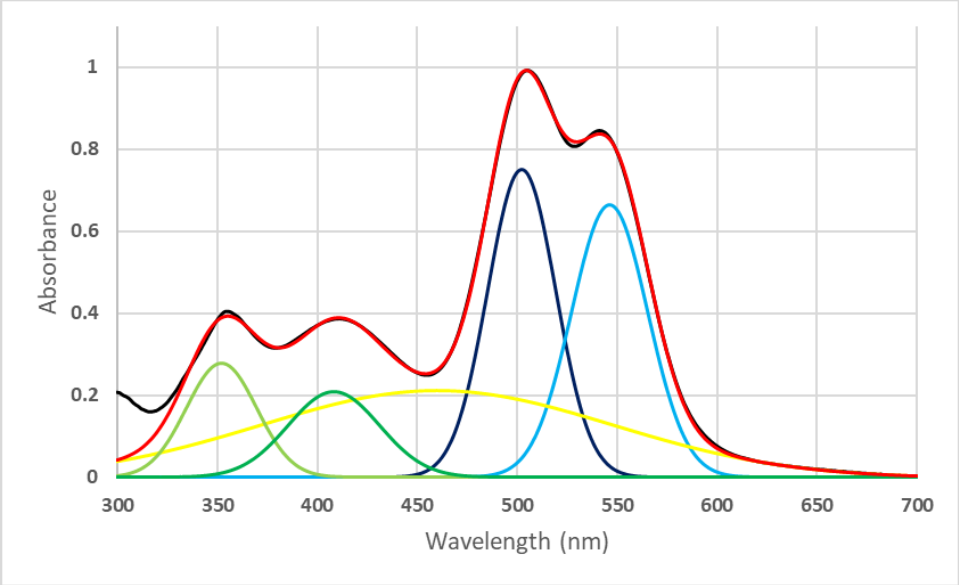

Figure 4.25 The average UV-Vis spectrum of TiO_2 thin films loaded in a 0.5 mM AO/0.5 mM R6G dye loading solution with deconvolution into gaussian peaks.

The black line represents the average UV-Vis spectra, while the red line represents the best-fit solution of five gaussian peaks from 330-700 nm, one of which is the broad peak found in all films created from dye mixtures (yellow line). The green lines are the peaks associated with AO, while the blue lines are the peaks associated with R6G. The X2 value for the fit displayed is 0.015.

The deconvolution of the UV-Vis spectrum for the mixture of Ru2 and R6G is displayed in Figure 4.26. Deconvolution was performed from 450 – 700 nm. The films with this mixture strongly display the expected R6G peaks, again slightly red shifted at 499 nm and 546 nm. As the molar extinction coefficient for Ru2 is much lower than for R6G, the peak associated with Ru2 at 460 nm is not distinguishable from the spectrum. What is even worse is the 460 nm broad background presence in all films overlap almost perfectly with the Ru2 peak, further obscuring the observation of any Ru2 trapped in the TiO_2 film. If the broad 460 nm background presence had not been required for the best-fit spectrum of the AO and R6G films which contained no Ru2, it would have been tempting to assign it to the Ru2 peak despite the distribution being so

much broader. However, as the background is present even when Ru2 is not, we can confidently state that background is not due to the Ru2 peak, though it does obscure our ability to measure it.

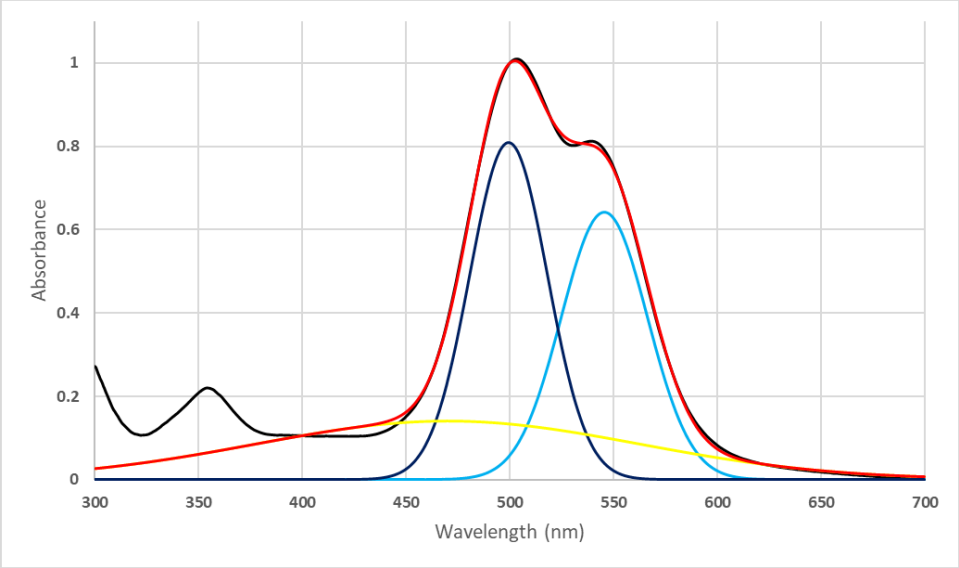

Figure 4.26 The average UV-Vis spectrum of TiO_2 thin films loaded in a 0.5 mM R6G/0.5 mM Ru2 dye loading solution deconvoluted into gaussian peaks.

The black line represents the average UV-Vis spectra, while the red line represents the best-fit solution of three gaussian peaks from 450-700 nm, one of which is the broad peak found in all films created from dye mixtures (yellow line). The blue lines are the R6G monomer and dimer peaks. The X2 value for the fit displayed is 0.017.

Both of the previous dye mixtures had UV-Vis spectra that aligned with expectations for the dyes loading into thin film without significant levels of dye interaction. Figure 4.27 displays the deconvolution of the UV-Vis spectrum for films loaded with a mixture of AO and Ru2. Deconvolution was performed from 330 – 700 nm. For the AO and Ru2 mixture doped films, a similar lack of reactivity was expected. Based on the individual peak locations and intensity, we would expect clear AO peaks around 370 and 430 nm if there was no dye interaction. The main peak for Ru2 loaded individually into films is at 460 with a shoulder at 425-430 nm, which may or may not display in the absorption spectra based on its comparatively low molar absorptivity. Examining Figure 4.27, the AO peaks are visible at 364 and 429 nm, which aligns with the

expected AO peaks. Contrarily, along with the broad 460 nm background presence, two new peaks appear at 497 nm and 551 nm that cannot be explained by the spectra of AO or Ru2 trapped in thin films individually. These peaks also do not exist in any diluted solution of AO/Ru2 dye mixture that produces a reasonably measurable absorbance spectrum.

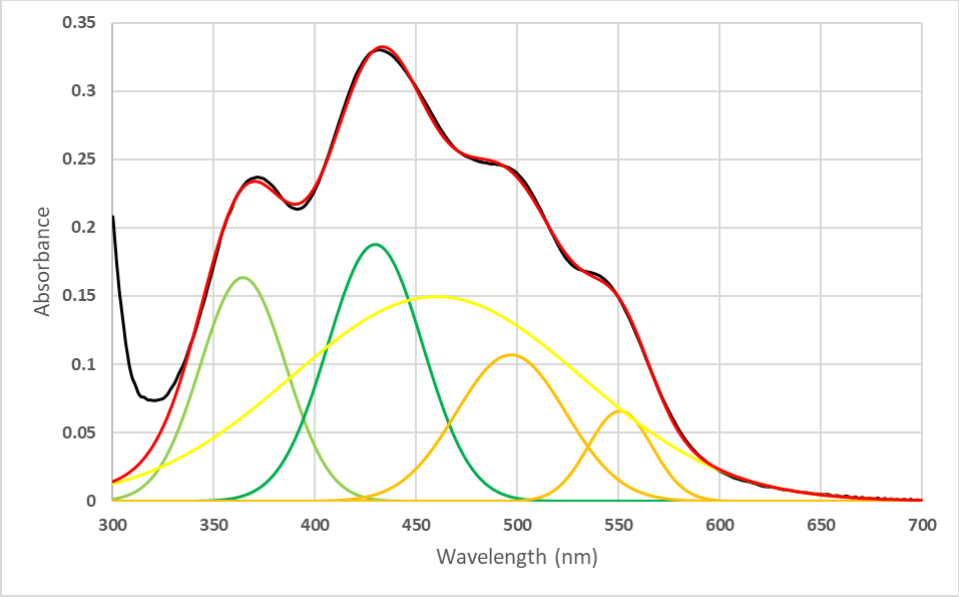

Figure 4.27 Deconvolution of the average UV-Vis spectra of TiO_2 thin films loaded in a 0.5 mM AO/0.5 mM Ru2 dye loading solution.
The black line represents the average UV-Vis spectra, while the red line represents the best-fit solution of five gaussian peaks from 330-700 nm, one of which is the broad peak found in all films created from dye mixtures (yellow line). The X^2 value for the fit displayed is 0.0036.

The nature of dye loading by kinetic doping results in a much higher concentration of dye than can be obtained in solution, trapping the dye molecules in mesoporous pockets within the film matrix. The current hypothesis for the occurrence of these new peaks is that the close proximity of the AO and Ru2 molecules in the film causes them to interact in a way that does not occur in solution when the dyes are much farther apart, resulting in the new shoulders at 497 and 551 nm. Since these new shoulders occur near the peak locations for R6G, an estimate of the exact concentrations of individual dyes within a film containing all three dyes will not be possible.

4.3.2 Triple Dye Loading

A one-pot loading of all three individually stable dyes was also achieved. Equal aliquots of 1 mM R6G, 1 mM AO, and 1 mM Ru2 loading solution at pH 7.3 were mixed to create 1 mM of total dye solution in 10 mM phosphate buffer. The deconvolution of the average UV-Vis spectrum of these films is shown in Figure 4.28. Deconvolution was performed from 330 – 700 nm.

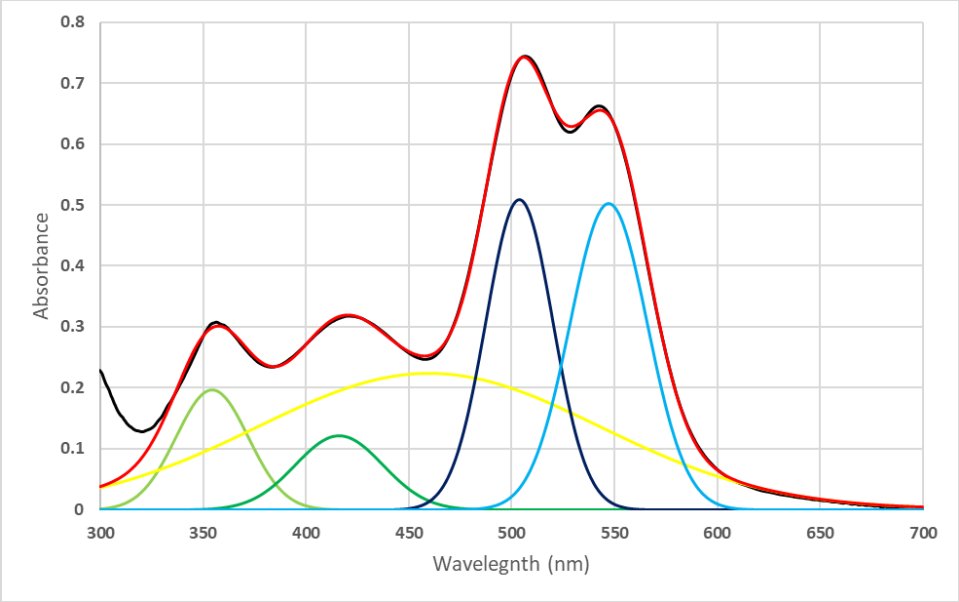

Figure 4.28 Deconvolution of the average UV-Vis spectra of TiO_2 thin films Loaded in a 0.33 mM R6G/0.33 mM AO/0.33 mM Ru2 dye loading solution.

The black line represents the average UV-Vis spectra, while the red line represents the best-fit solution of five gaussian peaks from 330-700 nm, one of which is the broad peak found in all films created from dye mixtures (yellow line). The X^2 value for the fit displayed is 0.0093.

The three-dye film contains strong peaks associated with the R6G at 503nm and 547 nm, displaying a similar red shift to the ones seen in the dual dye films. The AO peaks have shifted to 354 nm and 416 nm, a slight blue shift from the expected location of the AO peaks, but not as

significantly shifted as in the dual-dye mixture with R6G. The same broad gaussian background at 460 nm required to create the best-fit spectrum is also present, which prohibits the detection of Ru2.

A second mixture of the three main dyes that load kinetically into mechanically stable thin films on their own was created with a total concentration of 3 mM, and the average spectrum deconvoluted. The deconvolution of the average UV-Vis spectrum of these films is shown in Figure 4.29. Deconvolution was performed from 330 – 700 nm. While the four main peak locations of the deconvolution shifted minutely (~3 nm for each peak apart from the 416 nm peak, which shifted to 424 nm), the overall distribution of the spectrum was the same. The scale of the absorption spectra increased when loading in the 3 mM loading solution, indicating a significant increase in dye loading with the increase in concentration of loading solution.

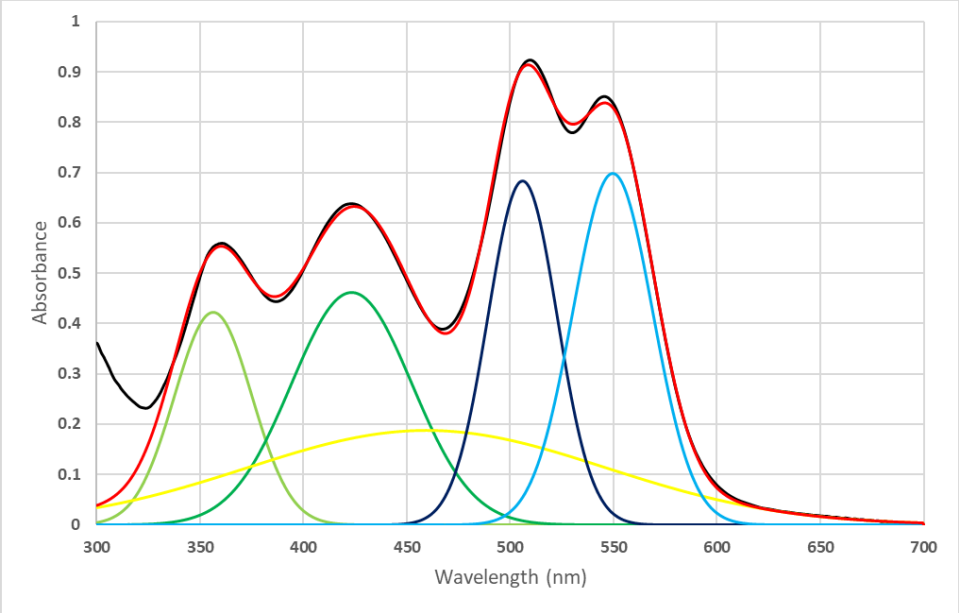

Figure 4.29 Deconvolution of the average UV-Vis spectra of TiO_2 thin films loaded in a 1 mM R6G/1 mM AO/1 mM Ru2 dye loading solution.

The black line represents the average UV-Vis spectra, while the red line represents the best-fit solution of five gaussian peaks from 330-700 nm, one of which is the broad peak found in all films created from dye mixtures (yellow line). The X^2 value for the fit displayed is 0.042.

In both the three-dye mixtures and the different dual dye mixtures it participates in, the R6G absorption peaks have shifted slightly to the red by 10-15 nm. This may or may not be significant, as the peak location was allowed to float to provide the best-fit theoretical spectra. If there is significance to it, since the monomer peak experiences a slightly larger shift than the dimer peak, it may have to do with a transition between the monomer and J-type dimer forms. The J-type dimer of R6G is calculated to have a slightly red shift from the monomer by an ab initio study[8], giving credence to the idea that perhaps some portion of the monomer concentration has transitioned to the J-type dimer upon mixing with the other dyes.

4.3.3 Quadruple Dye Loading

The dual dye and triple dye loading experiments demonstrated that the presence of R6G allowed for robust amorphous TiO_2 films at pH 7.3 even with the presence of the dyes which would ordinarily produce less mechanically stable thin films. In case this held true with Nile blue, 1 mM Nile blue was added to the dye mixture for a quadruple dye loading solution. Figure 4.30 displays the optically clear, mechanically stable thin films which were loaded in a 4 mM solution containing 1 mM concentrations of all four dyes.

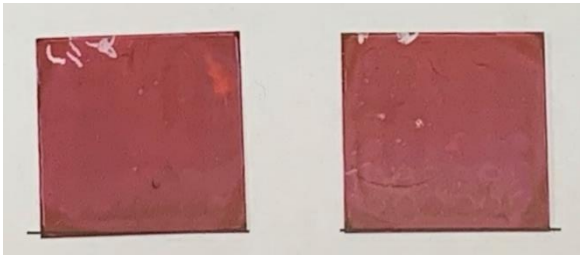

Figure 4.30 Film duplicates kinetically doped in 4mM dye loading solution of 1 mM each R6G, AO, Ru2, and Nile blue in 10 mM phosphate buffer at 0-minute post spin-coat delay

Figure 4.31 displays the average UV-Vis absorption spectra of the quadruple dye thin film from 400-700 nm. The AO peak within this range and the R6G peaks do not experience any major shifts from the triple dye thin films, but the quadruple dye film has a peak clearly associated with the Nile blue around 640 nm which allows for the absorption of light between 600-700 nm which is not attained in the triple dye thin films.

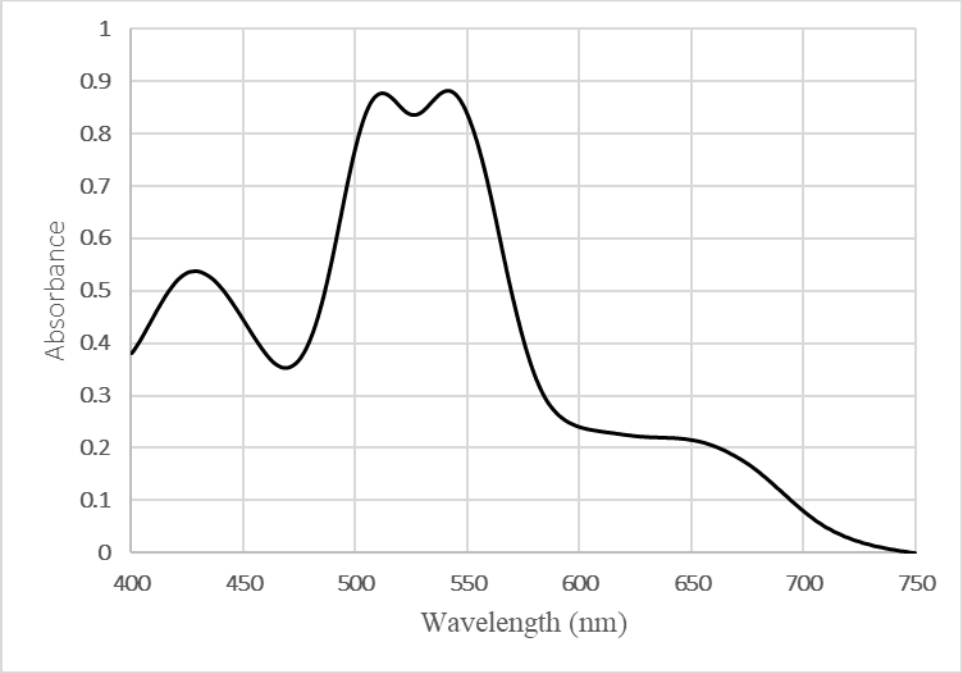

Figure 4.31 Average absorption spectra of TiO_2 thin films kinetically doped with loading solutions of 1 mM each R6G, AO, Ru2, and Nile blue in 10 mM phosphate buffer

With anatase titania absorbing at wavelengths below 380 nm[29], an anatase film with all of these dyes loaded should allow the prototype solar cell to absorb photons across the range of 300-700 nm. While the concentration of each dye in the film cannot be calculated due to overlapping peaks and molar extinction coefficient values on vastly different scales, kinetic doping has demonstrated the ability to sensitize the TiO_2 with multiple organic dyes at once, increasing the range of light absorption.

4.4 Conclusions

In this part of the work, a sol-gel synthesis method was established that resulted in an optically clear thin film in a sufficiently mutable state to kinetically dope multiple individual dyes under optimized loading conditions. It is established that the phosphate buffer loading solution is critical to stabilizing the TiO_2 thin films and encouraging kinetic doping. Concentrations of individual dyes in a loaded thin film ranged from 0.76 – 1.9 M depending on the dye loaded. Mixtures of up to four dyes were co-loaded into the thin films via kinetic doping, demonstrating the potential for these films to utilize a wide range of visible light. A hypothesis that guest molecules must be positively charged in the loading solution is expanded upon. A secondary hypothesis is suggested that molecules with an overall positive charge containing iminium ions are specifically likely to load well.

4.5 References

1. Guglielmi, M.; Carturan, G., Precursors for sol-gel preparations. *Journal of Non-Crystalline Solids* **1988,** *100* (1), 16-30.

2. Arnal, P.; Corriu, R. J. P.; Leclercq, D.; Mutin, P. H.; Vioux, A., A Solution Chemistry Study of Nonhydrolytic Sol−Gel Routes to Titania. *Chemistry of Materials* **1997,** *9* (3), 694-698.

3. Kamiya, K.; Tanimoto, K.; Yoko, T., Preparation of TiO2 fibres by hydrolysis and polycondensation of Ti(O—i-C3H7)4. *Journal of Materials Science Letters* **1986,** *5* (4), 402-404.

4. Nishikiori, H.; Setiawan, R. A.; Kawamoto, S.; Takagi, S.; Teshima, K.; Fujii, T., Dimerization of xanthene dyes in sol–gel titania films. *Catalysis Science & Technology* **2013,** *3* (10), 2786-2792.

5. Sharma, R.; Sarkar, A.; Jha, R.; Kumar Sharma, A.; Sharma, D., Sol-gel–mediated synthesis of TiO2 nanocrystals: Structural, optical, and electrochemical properties. *International Journal of Applied Ceramic Technology* **2020,** *17* (3), 1400-1409.

6. Liang, Y.; Sun, S.; Deng, T.; Ding, H.; Chen, W.; Chen, Y., The Preparation of TiO2 Film by the Sol-Gel Method and Evaluation of Its Self-Cleaning Property. *Materials* **2018,** *11* (3).

7. Campbell, A. L. O.; Lei, Q.; Tak Yip, W., Kinetic approach to hyper-doped optical quality thin films. *Chemical Communications* **2014,** *50* (66), 9321-9324.

8. Gavrilenko, V. I.; Noginov, M. A., Ab initio study of optical properties of rhodamine 6G molecular dimers. *The Journal of Chemical Physics* **2006,** *124* (4), 044301.

9. Avnir, D.; Kaufman, V. R.; Reisfeld, R., Organic fluorescent dyes trapped in silica and silica-titania thin films by the sol-gel method. Photophysical, film and cage properties. *Journal of Non-Crystalline Solids* **1985,** *74* (2), 395-406.

10. Prahl, S. Tris(2,2'-bipyridyl)ruthenium(II) in water https://omlc.org/spectra/PhotochemCAD/html/085.html (accessed 4/12/2020).

11. Perera, V. P. S.; Pitigala, P. K. D. D. P.; Jayaweera, P. V. V.; Bandaranayake, K. M. P.; Tennakone, K., Dye-Sensitized Solid-State Photovoltaic Cells Based on Dye Multilayer−Semiconductor Nanostructures. *The Journal of Physical Chemistry B* **2003,** *107* (50), 13758-13761.

12. Amdursky, N.; Huppert, D., Auramine-O as a Fluorescence Marker for the Detection of Amyloid Fibrils. *The Journal of Physical Chemistry B* **2012,** *116* (45), 13389-13395.

13. Manaf, M. A.; Kassim, A.; Desa, M. Z.; Ali, Y., STUDY OF AURAMINE O DYE-SENSITIZED PHOTOELECTROCHEMICAL SOLAR CELL. *Malaysian Journal of Analytical Sciences, Vol. 9, No. 3 (2005)* **2005,** *9* (3), 521.

14. Hurtado-Morales, M.; Pazos-Alonso, J. E.; Garcia-Fox, M. A.; Castarlenas, S.; Téllez, C.; Coronas, J. In *Structural characterization of Graphene Oxide and Reduced Graphene Oxide used as counter electrode in flexible DSSC*, 2018 IEEE 7th World Conference on Photovoltaic Energy Conversion (WCPEC) (A Joint Conference of 45th IEEE PVSC, 28th PVSEC & 34th EU PVSEC), 10-15 June 2018; 2018; pp 1116-1121.

15. Chou, T. P.; Zhang, Q.; Cao, G., Effects of Dye Loading Conditions on the Energy Conversion Efficiency of ZnO and TiO2 Dye-Sensitized Solar Cells. *The Journal of Physical Chemistry C* **2007,** *111* (50), 18804-18811.

16. Nazeeruddin, M. K.; Splivallo, R.; Liska, P.; Comte, P.; Grätzel, M., A swift dye uptake procedure for dye sensitized solar cells. *Chemical Communications* **2003,** (12), 1456-1457.

17. Mali, S. S.; Betty, C. A.; Bhosale, P. N.; Patil, P. S., Eosin-Y and N3-Dye sensitized solar cells (DSSCs) based on novel nanocoral TiO2: A comparative study. *Electrochimica Acta* **2012,** *59*, 113-120.

18. Kao, M. C.; Chen, H. Z.; Young, S. L.; Kung, C. Y.; Lin, C. C., The effects of the thickness of TiO2 films on the performance of dye-sensitized solar cells. *Thin Solid Films* **2009,** *517* (17), 5096-5099.

19. Baglio, V.; Girolamo, M.; Antonucci, V.; Aricò, A., Influence of TiO2 film thickness on the electrochemical behaviour of dye-sensitized solar cells. *Int. J. Electrochem. Sci* **2011,** *6* (8), 3375-3384.

20. Crosley, M. S.; Yip, W. T., Silica Sol–Gel Optical Biosensors: Ultrahigh Enzyme Loading Capacity on Thin Films via Kinetic Doping. *The Journal of Physical Chemistry B* **2017,** *121* (9), 2121-2126.

21. Crosley, M. S.; Yip, W. T., Multienzyme, Multistep Biosensor Produced through Kinetic Doping. *The Journal of Physical Chemistry B* **2019,** *123* (18), 3962-3967.

22. Jensen, J. M.; Yip, W. T., Enzyme Loading in Internally-Coated Capillary Tubes Via Kinetic Doping. *Coatings* **2020,** *10* (6), 532.

23. Jensen, J. M.; Yip, W. T., Amine Functionalization of Silica Sol–Gel Thin Films via Kinetic Doping: A Novel, Green Approach. *ACS Omega* **2019,** *4* (20), 18545-18554.

24. Siami, E.; Sabzi, R.; Rasouli, F.; Kheiri, F., Nile Blue and Nickel Organometallic Dyes Applied in Dye-sensitized Solar Cells. *Portugaliae Electrochimica Acta* **2015,** *33*, 23-33.

25. Kamat, P. V., Photoelectrochemistry in colloidal systems. Part 2.—A photogalvanic cell based on TiO2 semiconductor colloid. *Journal of the Chemical Society, Faraday Transactions 1: Physical Chemistry in Condensed Phases* **1985,** *81* (2), 509-518.

26. Cole, J. M.; Pepe, G.; Al Bahri, O. K.; Cooper, C. B., Cosensitization in Dye-Sensitized Solar Cells. *Chemical Reviews* **2019,** *119* (12), 7279-7327.

27. Reddy, K. S. K.; Chen, Y.-C.; Wu, C.-C.; Hsu, C.-W.; Chang, Y.-C.; Chen, C.-M.; Yeh, C.-Y., Cosensitization of Structurally Simple Porphyrin and Anthracene-Based Dye for Dye-Sensitized Solar Cells. *ACS Applied Materials & Interfaces* **2018,** *10* (3), 2391-2399.

28. Jia, H.-L.; Li, S.-S.; Gong, B.-Q.; Gu, L.; Bao, Z.-L.; Guan, M.-Y., Efficient cosensitization of new organic dyes containing bipyridine anchors with porphyrins for dye-sensitized solar cells. *Sustainable Energy & Fuels* **2020,** *4* (1), 347-353.

29. Fujishima, A.; Zhang, X., Titanium dioxide photocatalysis: present situation and future approaches. *Comptes Rendus Chimie* **2006,** *9* (5), 750-760.

5. Crystallization of Dye-Doped TiO_2 Thin Films

5.1 Introduction

The main reason most DSSCs are doped via post-doping methods is that semiconductors like titania are more effective in a crystallized form than an amorphous form. For titania, the rutile or anatase forms are most commonly used for DSSCs, since the brookite crystallized form is less thermodynamically stable. While both rutile and anatase titania are used, anatase titania is the slightly more efficient semiconductor due to its indirect band gap.[1, 2] This causes an obvious issue with pre-doping methods because the most traditional approach to achieve either crystallized form from a sol-gel film or nanoparticle paste is to heat the sample at high temperatures for an extended time[3, 4].

While the structure of the thin film can enhance the thermal stability of entrapped organic dyes, the dyes may still decompose at sufficiently high temperatures. For kinetic doping to produce a hyper-doped anode material with a crystalline film instead of an amorphous one, the dye needs to remain stable throughout the crystallization process. If the high-temperature annealing method proves unfeasible due to dye decomposition, a low-temperature annealing method will be needed.

One such method recently gaining ground is the hydrothermal annealing method[5, 6]. This method involves exposing the film to steam in a pressurized environment for an extended period. The presence of the pressurized steam lowers the temperature requirement of the transition of the amorphous matrix into a crystalline form. The lower temperature should minimize the dye degradation expected during high-temperature heat annealing.

5.2 Materials, Equipment, and Standard Protocols

Standard sol-gels created as described in section 3.5 and aged 19-24 hours were used in the experiments in this chapter, along with a standard 1 mM R6G, AO, loading solutions as described in section 3.6.1. Prior to undergoing hydrothermal annealing, amorphous films were heated in a standard furnace at 150 °C for one hour.

Glass coverslips (25 mm × 25 mm, premium grade) were purchased from Fisher Scientific and cleaned prior to use following the protocol listed in section 3.4.

Spincoating was done using a Laurell Technologies WS-400/500 Series Spin Processor.

All UV–Vis spectra were obtained using a Shimadzu UV-2101PC UV/Vis Spectrometer set using a parallel two-beam configuration.

All XRD spectra were obtained using a Rigaku Miniflex600 Benchtop X-Ray Diffractometer.

A JEOL JSM-880 scanning electron microscope was used to take the images of the films at up to 50,000× magnification after the application of a 5 nm Au-Pd sputter-coat layer. Film thicknesses were determined by taking the average of three thickness measurements from a single film at different locations on the sample.

A 6-quart Instant Pot ® Max set at “High” pressure was used to create the hydrothermal annealing conditions at 118 ± 1 °C. For all tests unless otherwise stated, 1000 mL of water was used to fill the Instant Pot ® Max. Hydrothermal annealing was set to run for 8 hours, venting automatically as soon as the programmed time ended.

Films were set up for hydrothermal annealing as pictured below in Figure 5.1. The films in Figure 5.1 are placed in such a way to prevent either the vent area or center of the lid from

dripping condensed water onto the samples during the annealing process. In order to achieve successful hydrothermal annealing, it is critical that the films are facing up and that no significant amount of "standing water" is collected on the films. It is also essential that the films are removed from the hydrothermal annealing chamber and dried as soon as pressure is released. An example of what can occur should the films be exposed to standing water during the annealing process is shown in Figure 5.2. The large, uneven patches of the film which appear to contain no dye or inhomogeneous loading are the areas that were directly covered by standing water when the annealing chamber was opened. These water droplets were colored and had clearly leached the dye from these portions of the film.

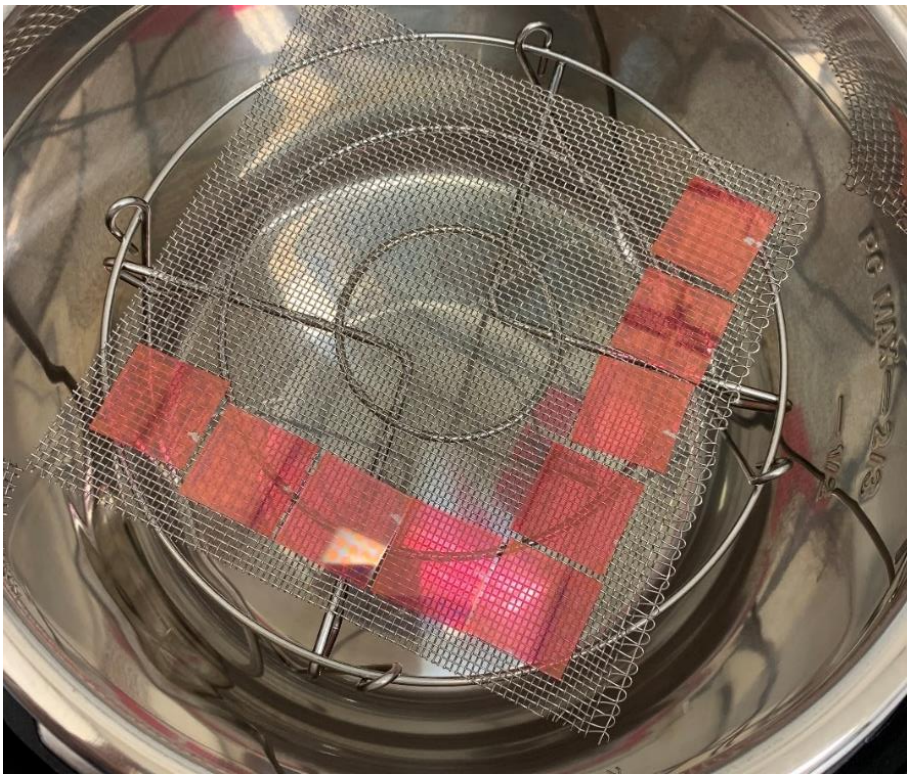

Figure 5.1 Most effective placement of thin films in the hydrothermal annealing chamber

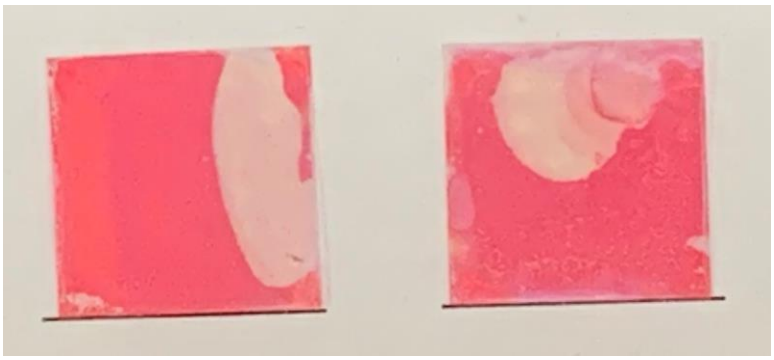

Figure 5.2 Examples of leaching damage caused by standing water during hydrothermal annealing

5.3 High-Temperature Annealing of Loaded Films

The traditional method of converting amorphous titanium dioxide to anatase titania is to anneal it at 400-600 °C for an extended period of time[3, 4, 7]. Therefore, initial tests established whether the expected XRD peaks could be obtained by the traditional methods in our sol-gel derived thin films. Undoped single layer films were treated with high-temperature heat annealing at 400 °C for 1-24 hours. The average for the XRD spectra of films in this annealed state is shown in Figure 5.3.

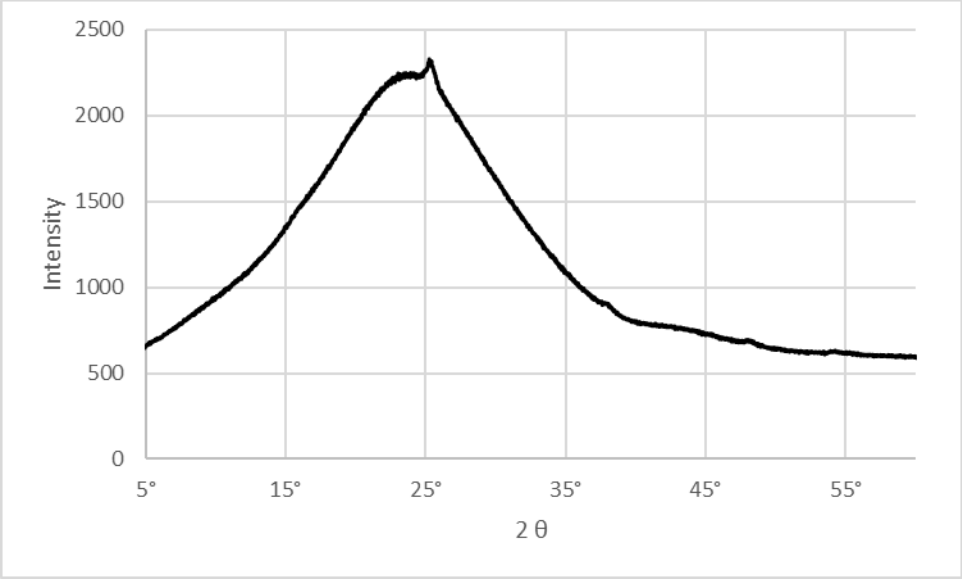

Figure 5.3 The XRD spectrum of a TiO_2 thin film heat-annealed at 400 °C for 24 hours

The XRD spectrum for a heat annealed film displayed a very broad signal with a few hard-to-distinguish sharper peaks. To quantify what appeared to be a background signal, the XRD spectra of both an amorphous thin film and a blank glass coverslip are shown below in Figure 5.4. The black line is the amorphous film on a coverslip, and the grey line represents the blank coverslip. It is obvious from this comparison that the amorphous TiO_2 film did not display any significant crystallization peaks. The broad background peak is almost certainly associated with the measurement of the amorphous glass coverslip.

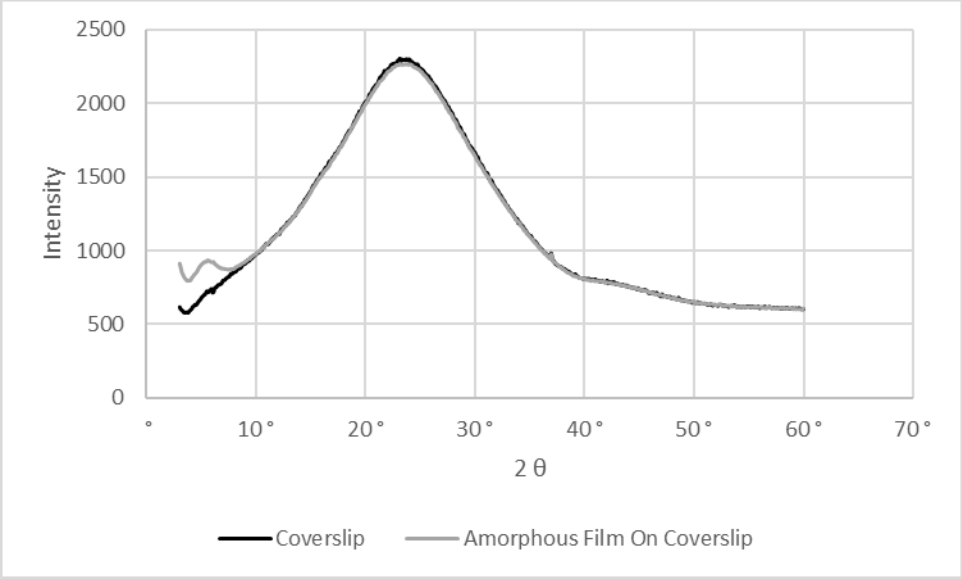

Figure 5.4 The XRD spectrum of an amorphous TiO_2 thin film on a coverslip (black) compared to the XRD spectrum of a blank glass coverslip (gray)

To remove the broad background contributed by the amorphous glass coverslip, the background signal was digitally subtracted to create a difference spectrum. For a blank amorphous TiO_2 thin film, the difference spectrum was obtained by subtracting the average XRD spectrum of clean glass coverslips. For the heat-annealed thin films, the difference spectrum was obtained by subtracting the average XRD spectrum of the amorphous films on coverslips before the annealing process.

As shown in Figure 5.5, after eliminating the background contributed by the amorphous glass coverslip with the amorphous film, the undoped thin films heated for 24 hours at 400 °C clearly display the characteristic crystallization peaks of anatase titania at 2θ = 25°, 38°, and minor peaks at 48° and 54°, which is the more effective crystal form of TiO_2 with regards to electron transfer.[1, 2, 8] No further change in crystallization peak intensity occurred after heat annealing for

an additional 24 hours (total of 48 hours). This was confirmed by the difference spectrum between the same sample that was annealed for 24 and 48 hours.

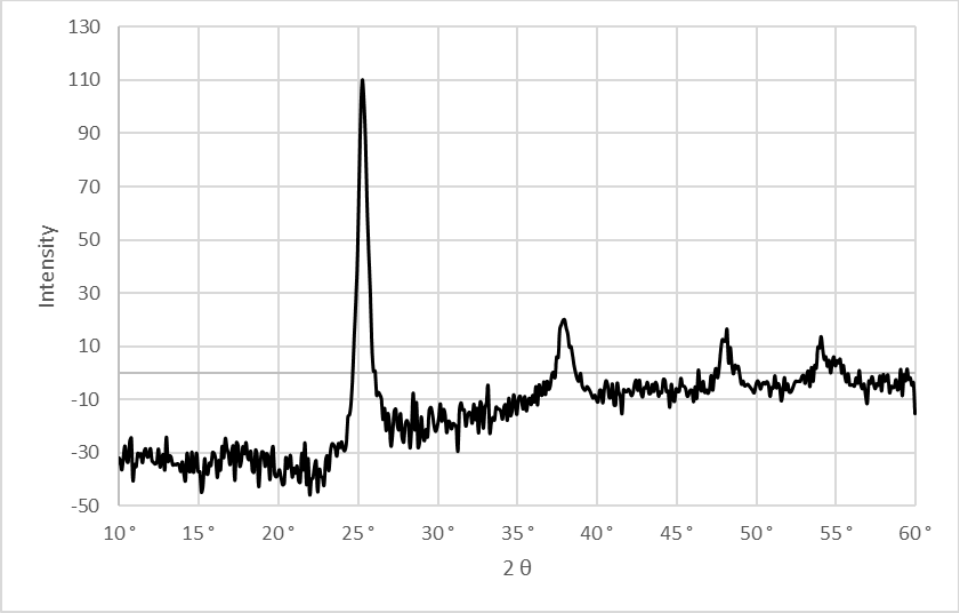

Figure 5.5 XRD difference spectrum of a single-layer TiO_2 thin film displaying anatase diffraction peaks after 24-hours of high-heat annealing at 400 °C

Based on the evidence of these experiments, undoped films heat annealed for 24 hours at 400 °C were judged to have reached the maximum state of anatase crystal transformation. However, the main challenge to overcome is that the kinetically doped thin films will only retain their advantage if the majority of the organic dye survives the high temperature annealing process.

Previous experiments with silica thin films had demonstrated that R6G was protected from dye degradation up to 150 °C for at least an hour. With that knowledge, TiO_2 thin films were heat annealed at 150 °C for extended periods of time to determine whether TiO_2 would also protect the dye from degradation at higher temperatures. Figure 5.6 illustrates the absorption spectra of these films.

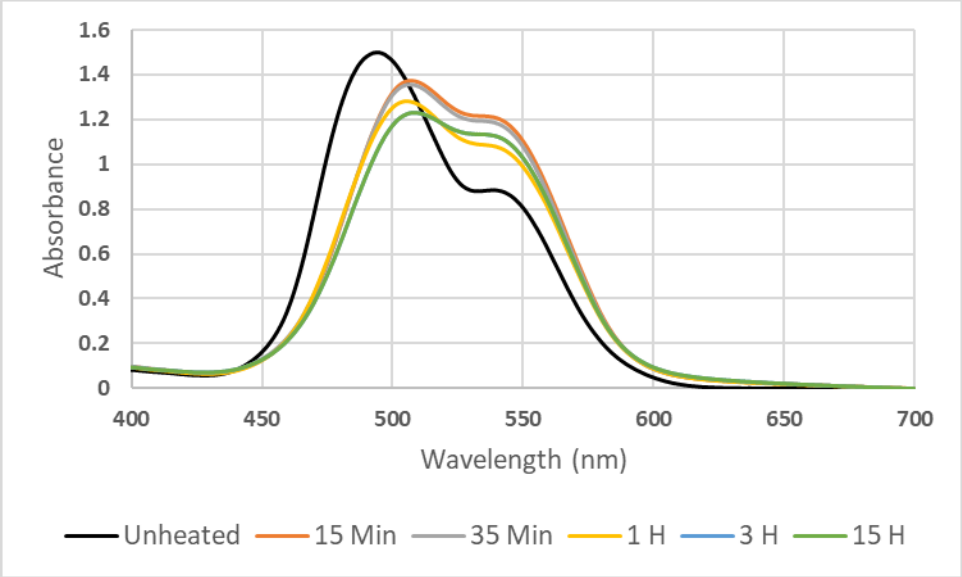

Figure 5.6 The UV-Vis absorption spectra of R6G-doped TiO_2 thin films heat annealed at 150 °C for various times

As the films are heated at 150 °C, the shape of the absorption spectra changes as the film condenses and dehydrates. The overall shape of the spectra displays a red shift, with both main peaks shifting to longer wavelengths and the ~540 nm monomer/J-type dimer peak displaying a higher prominence compared to the spectra of an unheated film. Without deconvoluting the spectrum, the exact peak shift for the H-type dimer peak is not known, but the distribution of the two peaks has clearly shifted. It is quite possible that as the pores shrink during the condensation process, some of the H-type dimer may be forced into the J-type dimer or monomer form. Encouragingly, there is significant dye retention, even after 15 hours at 150 °C. Unfortunately, the XRD difference spectra indicated no evidence of crystallization.

Despite the concern that the dye may degrade at higher temperatures, an attempt to crystallize the doped films at 400 °C was made. Dye doped thin films were heated at 400 °C for up to an hour

to determine whether the dye would still be protected by its encapsulation in the film at such a high temperature. The results of this experiment are shown in the UV-Vis spectrum in Figure 5.7.

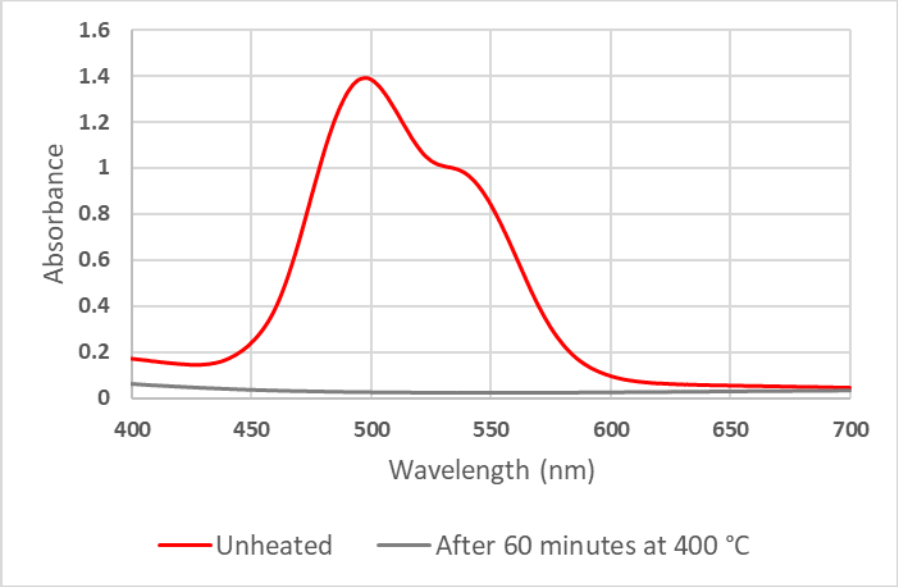

Figure 5.7 The UV-Vis absorption spectra of R6G-doped TiO_2 thin films before and after heat annealing at 400 °C for 1 hour

By comparing the spectrum before and after the annealing process, it is obvious that the dye degraded almost completely after only an hour of exposure at 400 °C. As a result, direct high temperature annealing of the films was not a viable option. A plan for a less destructive low-temperature annealing method based on the published work of Nishikiori et al was devised.[5]

5.4 Single-Layer Hydrothermal Annealing

The original intent on designing the anode material to be used for solar cells was to create a single, thin layer of anode material hyper-doped with dye that was in direct contact with the semiconducting TiO_2 material. This is illustrated by the schematic in Figure 5.8. Although the literature source indicated the use of an anatase template layer in hydrothermal annealing

experiments, it remained uncertain as to whether the template layer would prove essential to crystallize our TiO_2 thin films. If annealing could be induced without the template layer, the fabrication process would be more straightforward.

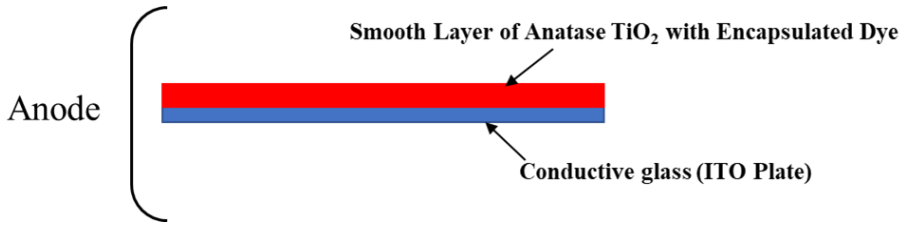

Figure 5.8 Schematic of desired anode material

An initial attempt was made by simply placing standard blank and R6G-doped single layer TiO_2 films into the hydrothermal annealing environment at 118 ±1 °C for 8 hours. As we had previously verified that trapped dye is protected up to 150 °C, it was expected to survive hydrothermal annealing at 118 °C. The encouraging news from this experiment is that the films visibly retained a significant portion of the original dye molecules. In addition, it is possible to retain an even greater fraction of the dye molecules by heating the films at 150 °C for an hour prior to hydrothermal annealing. The extra heat annealing step condenses the film, collapsing the pores. This is believed to be what prevents excessive dye leaching in the hydrothermal annealing environment.

While this method successfully eliminated comprehensive dye decomposition, the XRD diffraction spectra shown in Figure 5.9 did not display any noticeable anatase peaks, suggesting that no discernible crystallization took place upon hydrothermal annealing.

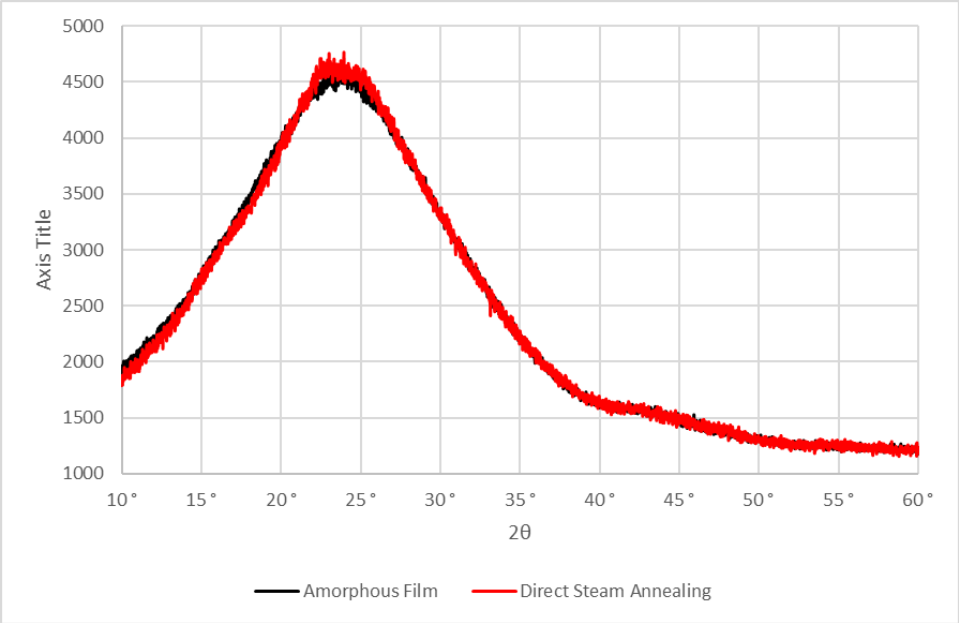

Figure 5.9 The XRD spectra of single-layer R6G-doped TiO_2 thin films before (black) and after (red) hydrothermal annealing

Direct hydrothermal annealing on a single layer dye-doped TiO_2 thin film proved untenable, so the avenue of providing an anatase template to induce crystallization was explored. Two approaches to introduce this anatase template were attempted. The first method was to spike the sol-gel at the time of reagent mixing with 0.0537 ± 0.0009 grams of either 5, 15, or 30 nm anatase nanoparticles. These anatase nanoparticles were purchased from US Research Nanomaterials, Inc. and used as received. The XRD spectra for both blank and R6G-doped films were measured for films that were hydrothermally annealed and compared to the spectrum of films that were heated at 400 °C for 8 hours. This method has the advantage that an anatase template could be added while maintaining the simplicity of the thin film fabrication process and retain dye doping throughout the entire anode layer. In the XRD spectra shown in Figures 5.10-5.12, the blue line is a dye-free nanoparticle spiked film that has been heated at 400 °C for 8 hours, the orange line is a dye-free nanoparticle spiked film that was hydrothermally annealed

for 8 hours, and the grey line is an R6G-doped, nanoparticle spiked film that was hydrothermally annealed for 8 hours.

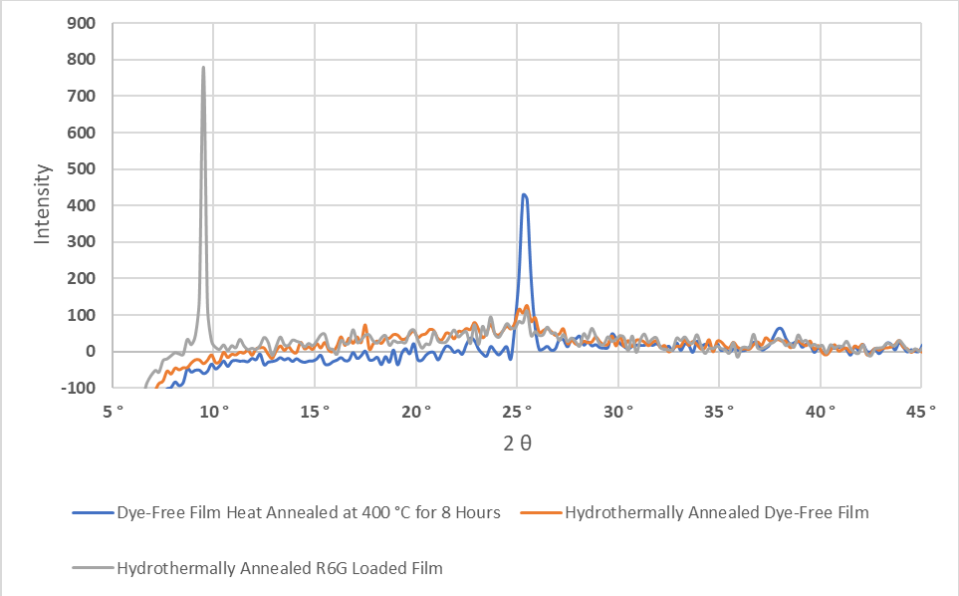

Figure 5.10 XRD difference spectra comparison for 5 nm anatase nanoparticle spiked TiO_2 thin films

In the 5 nm nanoparticle films in Figure 5.10, both the blank and R6G loaded films appear to increase slightly at the $2\theta = 25°$ anatase peak after hydrothermal annealing. Surprisingly, the R6G loaded film displayed a new peak at $2\theta = 9.5°$ that is not associated with anatase TiO_2. It is highly likely that this peak is associated with H-titanate, $H_2Ti_3O_7$, a different polymorph of titanium oxide.[9, 10]

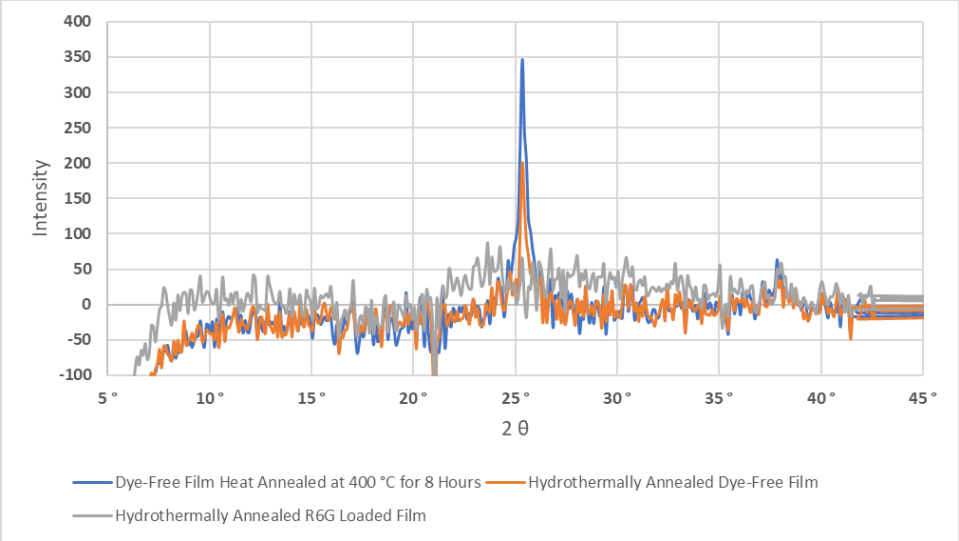

Figure 5.11 XRD difference spectra comparison for 15 nm anatase nanoparticle spiked TiO_2 thin films

In the 15 nm nanoparticle films in Figure 5.11, the undoped films displayed a noticeable increase in the main anatase peak at $2\theta = 25°$, but the R6G loaded films did not display any clear peak intensities. It is unclear why the nanoparticle-spiked blank film would crystallize but the dye loaded film spiked with the same nanoparticles would not even under identical hydrothermal annealing conditions.

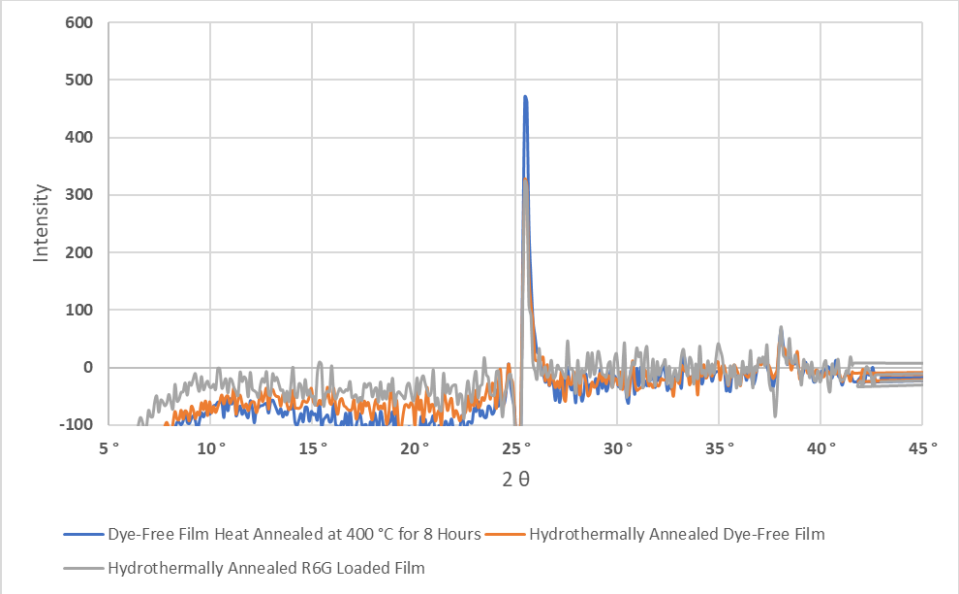

Figure 5.12 XRD difference spectra comparison for 30 nm anatase nanoparticle spiked TiO_2 thin films

In the 30 nm nanoparticle films in Figure 5.12, although both the average R6G loaded and blank films displayed an increase in the main anatase peak at $2\theta = 25°$, they displayed no noticeable increase in the minor anatase peaks. While there may be something at $2\theta = 38°$, the noise is significant enough that it is not distinguishable on this set of spectra. Since the nanoparticles should be randomly distributed, it is expected that all main anatase peaks be present. It was somewhat concerning that the minor peaks at 38, 48, and 54 did not show up in the XRD spectrum with a proportional intensity relative to the 25° peak. Moreover, the XRD difference spectra peak intensity appeared to vary wildly from film-to-film in an identically prepared triplicated sample set, indicating that perhaps the level of crystallization was inconsistent using the nanoparticle spiking method. Even though films spiked with nanoparticles were ultimately not selected for the solar cell anode material in this work, our preliminary results suggest that the 30 nm nanoparticle spiked sol-gels could have potential to produce films that could be consistently crystallized under hydrothermal annealing conditions.

5.5 Hydrothermal Annealing with an Anatase Template Layer.

The second method to introduce anatase to the kinetically doped TiO_2 thin film is to insert a full underlying template of anatase.[5] Thus, a dual-layer film system was developed for the anode material. This anode structure involved first spinning a blank TiO_2 thin film and heat annealing it at 400 °C for 24 hours to create the anatase template layer. Afterwards, a second amorphous layer of TiO_2 was then spun onto the anatase template film and then kinetically doped. A schematic of the intended anode structure is displayed in Figure 5.13.

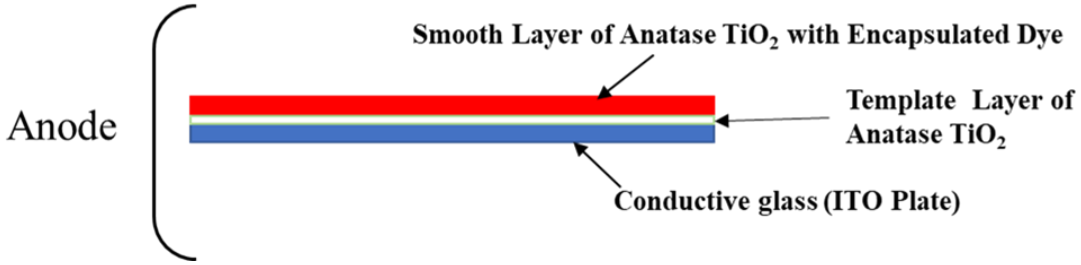

Figure 5.13 Schematic of anode material with an anatase template layer

5.5.1 XRD Analysis of Dual-Layer Films

When the dual-layer films were subjected to hydrothermal annealing, noticeable anatase peak growth was observed in both the blank and R6G loaded films at the two major peaks at 2θ = 25° and 38°. The blank films in Figure 5.14 also appear to display the minor anatase peaks at 2θ = 48° and 54°, but they are more difficult to distinguish from the noise.

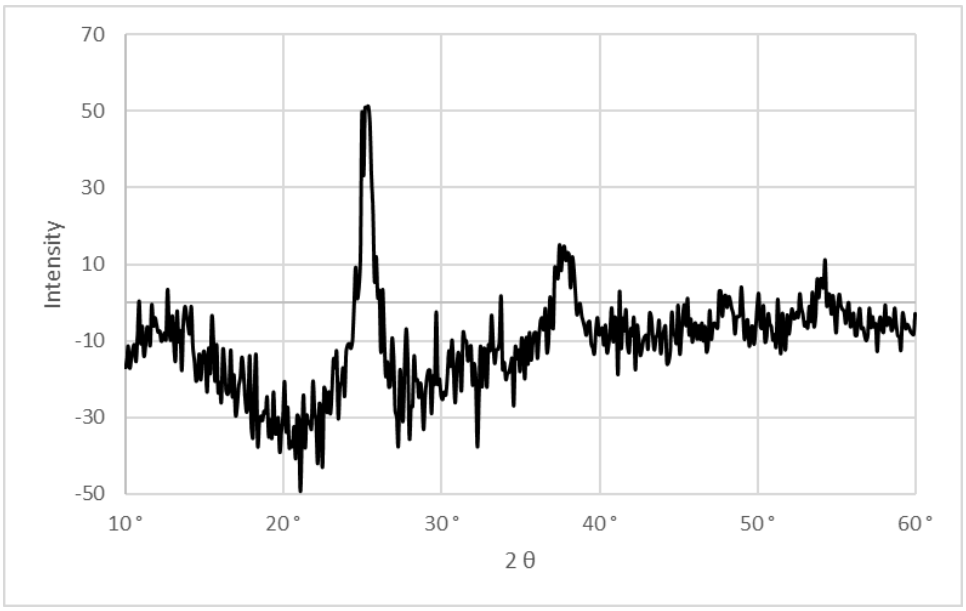

Figure 5.14 Difference spectra of blank dual-layer TiO_2 thin films after 8 hours of hydrothermal annealing

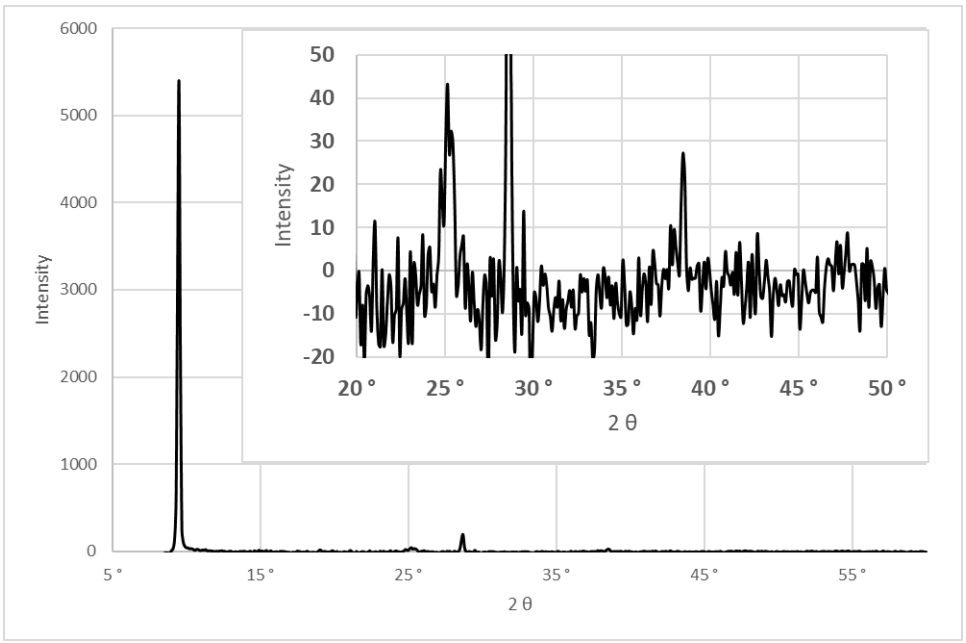

Figure 5.15 Difference spectra of R6G-doped dual-layer TiO_2 thin films after 8 hours of hydrothermal annealing

As seen in Figure 5.15, the R6G loaded dual layer films also display two very prominent peaks at $2\theta = 9.5°$ and $2\theta = 28.6°$ after hydrothermal annealing. These two new peaks vary in intensity from film to film but are always so strong that the anatase peaks require scaling in the graph to display them clearly (shown in the inset of Figure 5.15). The 9.5° peak appears to be the same as the one in Figure 5.1, and based on the literature, these two extra peaks indicate that the final doped film crystallization is most likely a mixture of anatase and H-titanate ($H_2Ti_3O_7$). Since these new peaks are not present in the blank film, it is quite possible that the presence of the dye dopants disrupted crystal organization and induce H-titanate formation during hydrothermal annealing.[9, 10] Since the peaks are consistent in location but of variable intensity, it is preferable to have a second method of confirmation to determine whether the film crystallization was taking place throughout the entire thickness.

5.5.2 SEM Analysis of Dual-Layer Film Morphology

SEM imaging was used to both monitor the change in grain morphology and determine the thickness of the films before and after hydrothermal annealing. Figure 5.16 displays the SEM images of several stages of development for single and dual-layer films from which the XRD spectra were collected. When comparing the SEM images, there is a noticeably clear difference in film thickness and grain size between the amorphous TiO_2 and crystalline TiO_2. The blank amorphous TiO_2 is 106 ± 3 nm thick (Figure 5.16a), while the R6G loaded amorphous film is 250 ± 30 nm thick (Figure 5.16b), likely due to swelling that takes place in the loading solution. Since the blank films are not placed in a loading solution, they should experience no swelling. Regardless, both amorphous films appear to have a fine, homogenous grain size. After high-temperature annealing at 400 °C, the blank anatase TiO_2 film is significantly condensed in comparison to the amorphous film (Figure 5.16c-d). The anatase films are 79 ± 2 nm thick,

approximately 27 nm thinner than the amorphous film. In addition, there is clearly a much coarser grain size in the heat annealed films compared to the amorphous films. Figure 5.16d is a magnified image of the area in the red rectangle in Figure 5.16c, showing the change in film texture more clearly. Figure 5.16e-f represent an undoped dual layer film before and after hydrothermal annealing for 8 hours, demonstrating the change in morphology for the amorphous layer. In Figure 5.16e, there is an obvious distinction between the fine grain amorphous top layer and the coarse grain heat-annealed anatase template layer. In Figure 5.16f, after hydrothermal annealing, the top layer of the film has clearly changed structure. The once amorphous film has crystallized and is now coarse grained, matching the grain texture of the underlying anatase template layer prepared from 400 ˚C annealing. This same observation is mirrored in the R6G loaded dual-layer film shown in Figure 5.16g-h.

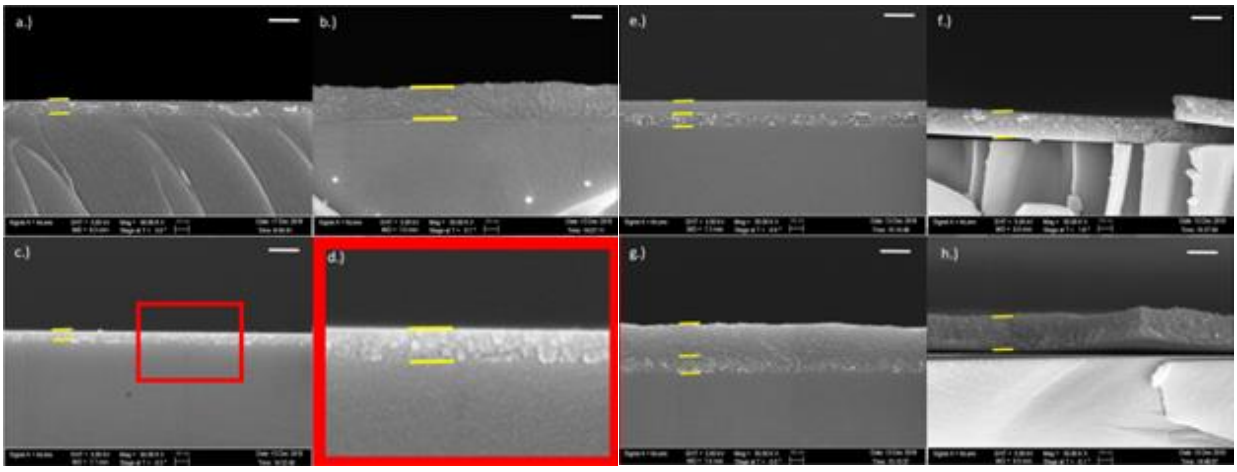

Figure 5.16 SEM Images of TiO_2 thin films at various stages of the hydrothermal annealing process. a) amorphous undoped film, b) amorphous R6G-doped film, c) undoped film heat annealed for 24 hours, d) magnified image of the indicated area in c), e) dual-layer undoped film before hydrothermal annealing, f) dual-layer undoped film after hydrothermal annealing, g) dual-layer R6G-doped film before hydrothermal annealing, h) dual-layer R6G-doped film after hydrothermal annealing. The white scale bars shown in the top right corners of the images represent a 200 nm length at this 50K magnification.

When combined with XRD spectra, the visual difference in grain size between the amorphous and crystallized TiO_2 films in the SEM images helps confirm the complete crystal transformation of the hydrothermally annealed films.

5.6 Concentration of R6G in Hydrothermally Annealed Films

Figure 5.17 Replicate hydrothermally annealed R6G-doped TiO_2 thin films

While some dye is removed during the hydrothermal annealing process, Figure 5.17 displays the visibly high R6G retention of hydrothermally annealed thin films. The average UV-Vis absorption spectrum was taken for these films and is displayed in Figure 5.18. The absorption spectrum was then deconvoluted into assignable gaussian peaks, which are also illustrated in Figure 5.18. Deconvolution was performed from 450 – 700 nm. The amplitudes of the gaussian peaks were then used to calculate the concentration of R6G within the final film.

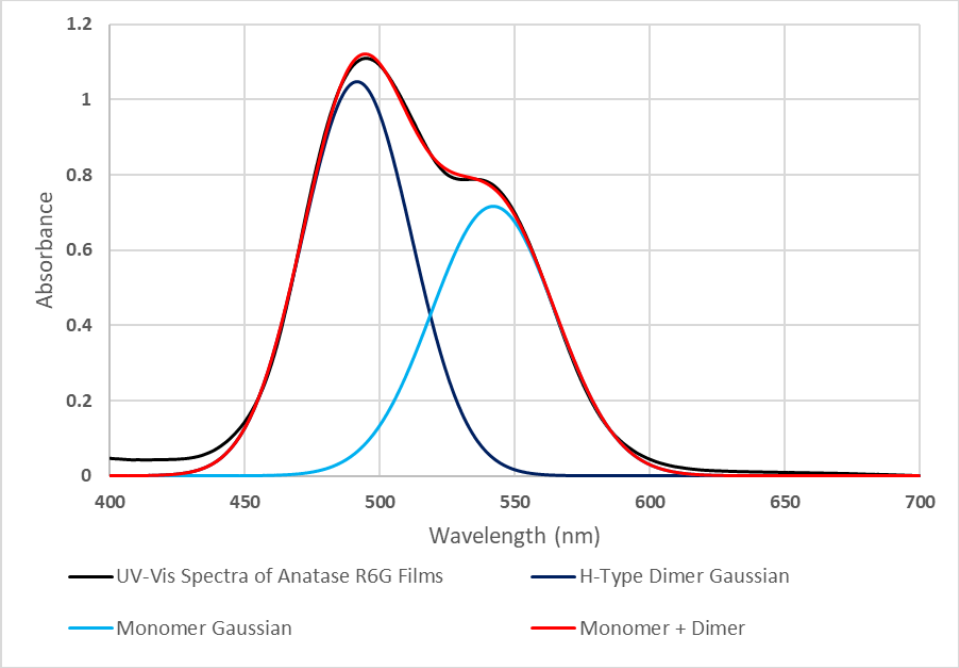

Figure 5.18 UV-Vis spectrum of dual-layer hydrothermally annealed R6G-doped TiO_2 thin film

SEM imaging was used to determine the thickness of the dual-layer film while evaluating the film morphology. Thickness of the dye-containing layer was determined by subtracting the average measured thickness of an undoped film heat annealed at 400 °C for 24 hours. This is done to remove the approximate thickness of the template anatase layer, which contains no dye, from the overall thickness of the crystalline hydrothermally annealed film.

Table 5-1: Summary of the key parameters for determining concentration in the hydrothermally annealed layer of R6G-doped thin film

Monomer Peak Values		Dimer Peak Values	
$\lambda_{monomer}$	542 nm	λ_{dimer}	491.6 nm
$A_{monomer}$	0.72 ± 0.01	A_{dimer}	1.05 ± 0.01
$\varepsilon_{monomer\ (531)}$[11]	78000 ± 1000 $cm^{-1}M^{-1}$	$\varepsilon_{dimer(500)}$[11]	94000 ± 1000 $cm^{-1}M^{-1}$
b	170 ± 20 nm	b	170 ± 20 nm

$$c_{monomer} = \frac{A}{\varepsilon b} = \frac{0.72}{(78000\ M^{-1}cm^{-1})(1.7*10^{-5}cm)} = 0.54 \pm 0.09\ \text{M}$$

$$c_{dimer} = \frac{A}{\varepsilon b} = \frac{1.05}{(94000\ M^{-1}cm^{-1})(1.7*10^{-5}cm)} = 0.66 \pm 0.07\ \text{M}$$

$$c_{total} = c_{monomer} + 2c_{dimer} = 0.54\ \text{M} + 2(0.66\ \text{M}) = 1.9 \pm 0.2\ \text{M}$$

With the condensed state of the crystallized layer at 170 nm, this results in a dye concentration of 1.9 M in the dye containing layer, as opposed to the 1.5 M in the 250 nm thick amorphous films. The increased dye concentration observed is the direct result of a thinner film upon hydrothermal annealing. These values can then be back calculated to determine an 85% dye retention rate. This high retention of dye molecules in a fully crystallized thin film means kinetic doping can be a viable loading method to achieve high dopant loading density within a crystalline matrix.

5.7 Crystallization of Films Loaded with Other Dyes

To create an anode material that absorbs across the solar spectrum, the crystallization process needs to work when the film contains more than just R6G as a dopant. Therefore, films doped with other dyes or even a mixture of multiple dyes were also hydrothermally annealed and assessed with XRD and SEM analysis. Two types of dye mixtures were examined. The first contains 1 mM each of AO, Ru2, and R6G, whereas the second contains 1 mM each of Ru2, R6G, and Nile blue. Figure 5.19 shows the absorption spectrum of films containing the AO, Ru2, and R6G dye mixture before and after hydrothermal annealing. As illustrated in the figure, thin films containing AO did not retain the AO absorbance peak near 430 nm after undergoing the hydrothermal annealing process. It is quite possible that AO degraded or leached out under hydrothermal annealing conditions. As a result, films that initially contained the dye mixture with AO were not tested further.

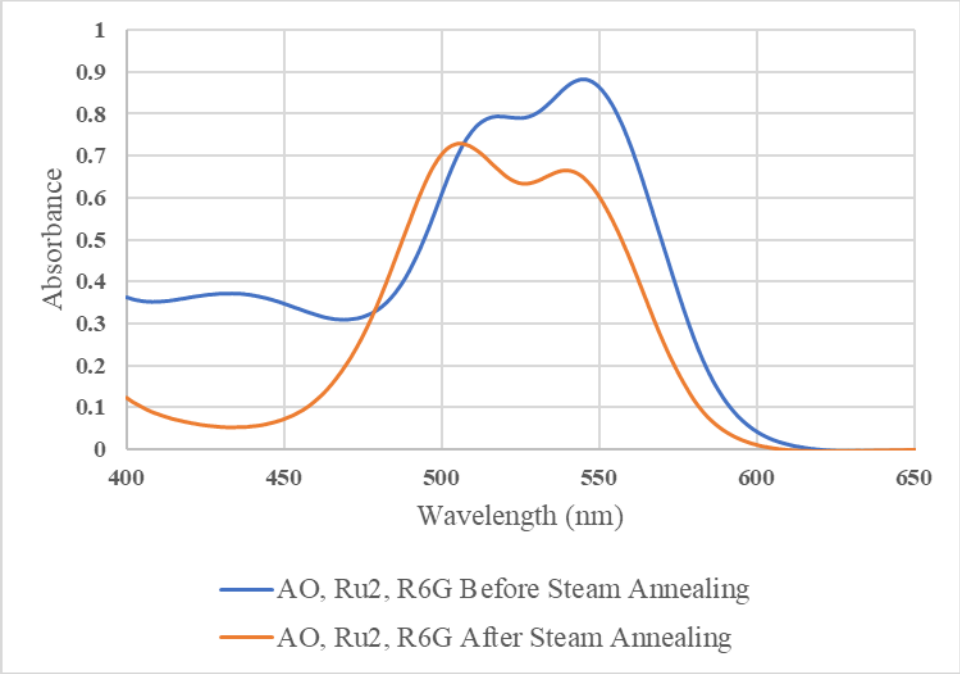

Figure 5.19 The UV-Vis absorption spectra for films containing AO, Ru2, and R6G before (blue) and after (orange) hydrothermal annealing

After hydrothermal annealing, XRD analysis was performed on both the individually doped Ru2 films and the films containing a mixture of Ru2, R6G, and Nile blue. The average XRD difference spectrum of the hydrothermally annealed Ru2 films is shown in Figure 5.20. In this spectrum, the main anatase peaks at $2\theta = 25°$ and $2\theta = 38°$ are clear, and there seems to also be a small increase in the minor anatase peaks at $2\theta = 48°$ and $2\theta = 54°$. Surprisingly, the H-titanate peaks are not present. Instead, there are two currently unidentified crystal peaks at $2\theta = 7.7°$ and $2\theta = 15.5°$. This indicates that similar to R6G, hydrothermal annealing also works for the Ru2 dye.

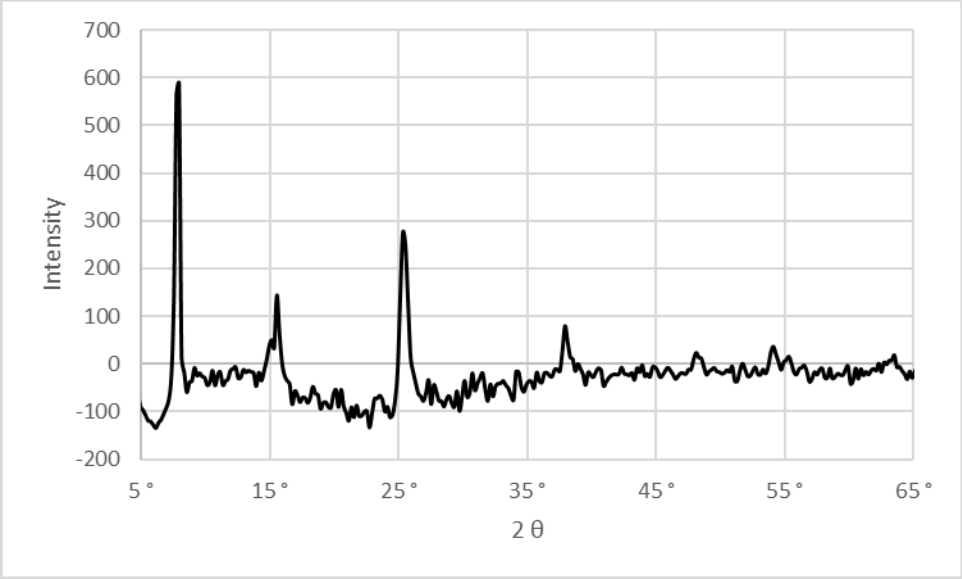

Figure 5.20 XRD difference spectrum for an Ru2-doped TiO_2 thin film

The average difference spectrum of the film containing a mixture of Ru2, R6G, and Nile blue is displayed in Figure 5.21. In the three-dye film, one of the strong peaks is the main H-titanate peak at $2\theta = 9.5°$, and the minor H-titanate peak at $2\theta = 28.6°$ is also visible. The same unknown peak observed in the Ru2 film at $2\theta = 7.7°$ is also present here, and there is a new strong unknown peak at $2\theta = 12.9°$. While there may be an increase at $2\theta = 25°$, the location of the main anatase peak, its present is difficult to distinguish from the other new peaks at $2\theta = 24.1°$ and $2\theta = 26.1°$. It appears that the presence of a mixture of dye could induce the formation of other crystalline forms of titania oxides, demonstrating the extensive interactions between the encapsulated dye molecules and the titania oxide matrix surrounding them during hydrothermal annealing.

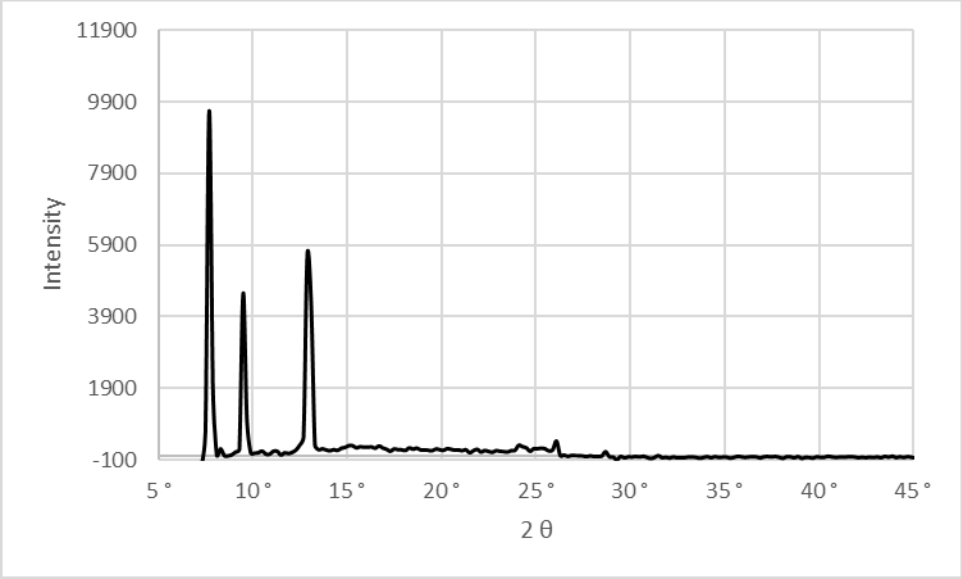

Figure 5.21 XRD difference spectrum for a TiO_2 thin film loaded with a mixture of R6G, Ru2, and Nile blue

Again, SEM analysis was necessary to evaluate the overall change in morphology of the films. SEM images of the amorphous and hydrothermally annealed films containing Ru2, R6G, and Nile blue are displayed in Figure 5.22.

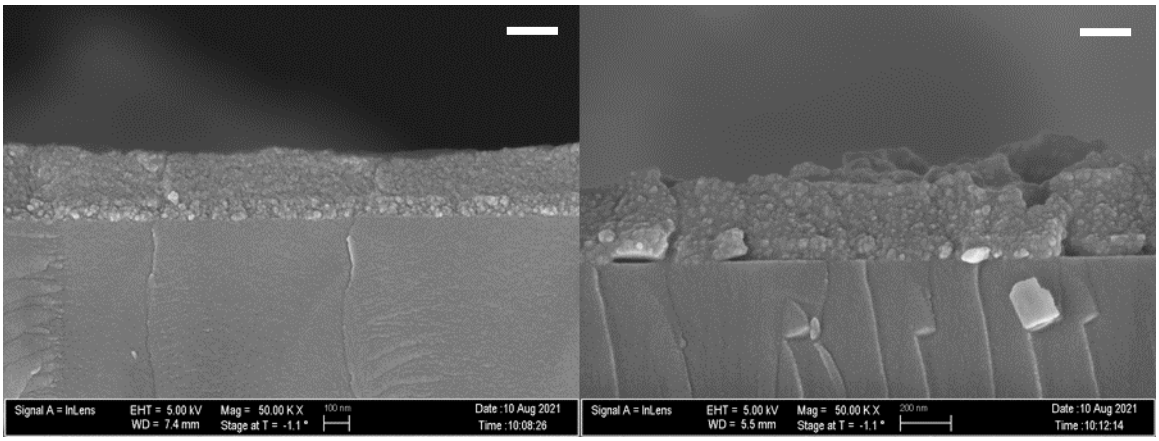

Figure 5.22 SEM imaging of (a) amorphous and (b) hydrothermally annealed dual-layer TiO_2 thin films containing a mixture of Ru2, Nile blue, and R6G. The white scale bar in the top right corner of the images represents a 200 nanometer length.

Even though there are some unidentified crystallization peaks in the annealed multi-dye film, the SEM imaging in Figure 5.22 does confirm the complete transition to a crystalline structure upon

hydrothermal annealing. The transition in texture displayed from Figure 5.22a to Figure 5.22b appears to be very similar to that of the annealed R6G loaded thin films. The fine-grain amorphous texture in the top layer of film that has not been hydrothermally annealed on the left transitions into a course-grain texture that matches the template layer after hydrothermal annealing, exactly as expected. While the crystalline form of multi-dye films may not be pure anatase, crystallization is sufficiently established in dye-loaded films to proceed with solar cell fabrication from thin films kinetically doped with multiple dyes.

5.8 Crystallization of Multi-Layered Films

Another goal as we begin to consider the final structure of the anode material is the ability to tune the thickness of the material. A single layer of the anode material detailed in this work so far is approximately 0.2 μm, while the anode layer in a typical DSSC reported in the literature can be as thick as 20 μm.[12-15] Very thick anode layers enhance solar energy absorption but do so at the expense of a longer electron diffusion length. A longer diffusion length will naturally result in additional electron loss due to scattering and recombination. Because these opposing influences must be balanced for optimum efficiency in different anode material, the kinetic doping approach offers a unique opportunity to optimize solar cell performance.[13, 16, 17] The spin-coating deposition method enables our amorphous material to increase the thickness reliably by set amounts. This presents an exceptional opportunity to fine tune the thickness of the anode materials with relative ease, giving us an added advantage in the optimization of power conversion efficiency in a finished solar cell. To establish the realistic attainability of an optimized anode by varying the anode thickness, thin films with 5, 10, 15, and 20 layers of amorphous, kinetically doped TiO_2 thin films were created and put through the hydrothermal annealing process.

To accomplish this, each multi-layered film began with a single blank template layer of heat-annealed anatase titania. After these template layers were cooled, on each subsequent day an individual layer of thin film was deposited, kinetically doped, rinsed, dried, and heated in a furnace at 150 °C for an hour. This process took place each day until the requisite number of layers of doped film had been achieved. The flowchart in Figure 5.23 illustrates the full process.

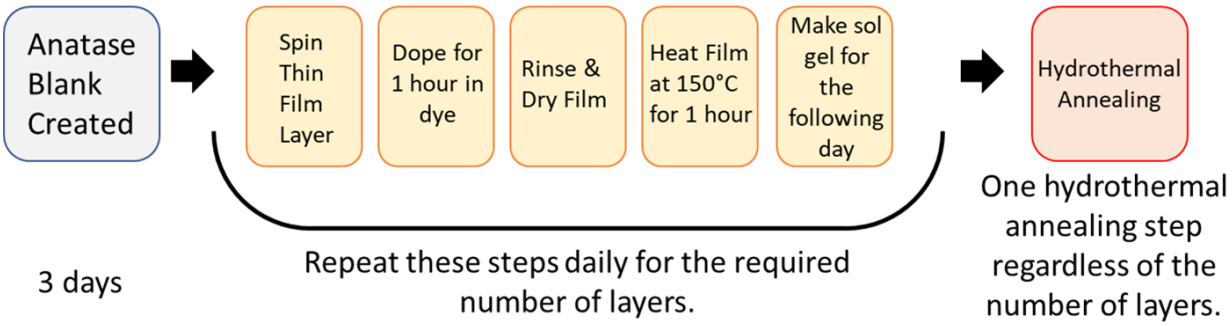

Figure 5.23 Flowchart of the multi-layered thin film creation process

The first layer of kinetically doped film can be created with static deposition (the sol-gel is deposited on the coverslip before the spinning process begins) as was done for all previous film deposition. However, because the sol-gel solvent is ethanol, static deposition of subsequent layers caused excessive dye leaching from the amorphous layer underneath due to high solubility of the dyes in ethanol. To minimize dye leaching, subsequent doped layers had to be created through dynamic deposition. Since dynamic deposition begins the spin cycle prior to the deposition of the liquid sol-gel, the individual layers created by dynamic deposition will be thinner than those created by static deposition. Once the amorphous multi-layer films were created, a few samples of the amorphous films were kept for XRD and SEM measurements, while others were hydrothermally annealed for 8 hours. Figure 5.24 displays the XRD analysis of

the multi-layer thin films after hydrothermal annealing. Regardless of the number of layers, all multi-layer films displayed intensity growth in the main anatase peak at $2\theta = 25°$, and most displayed significant intensity growth in the main H-titanate peak at $2\theta = 9.5°$ as well.

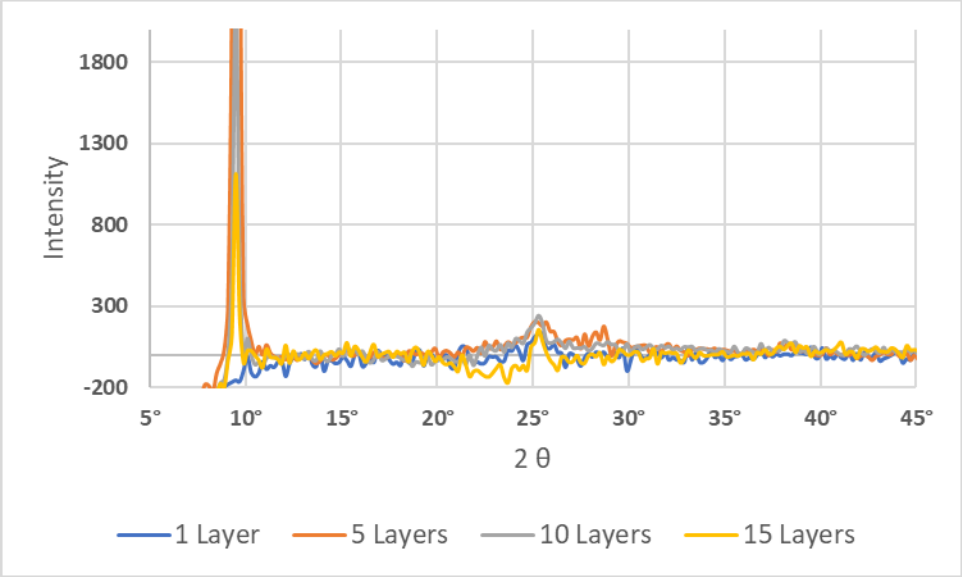

Figure 5.24 XRD difference spectra of the multi-layer thin films

In addition to XRD measurements, the sample films were examined using SEM imaging to assess the grain texture differences and to obtain the overall thickness. Results of the SEM measurements are summarized in Table 5-2.

Table 5-2 Thickness of multi-layered thin films determined by SEM analysis

Film Description	Average Total Thickness (nm)	Amorphous Layer Thickness	Average Dynamic Layer Thickness
1 undoped template layer, 5 doped amorphous layers	650 ± 30	561 nm	78 nm
1 undoped template layer, 5 doped annealed layers	770 ± 30		
1 undoped template layer, 10 doped amorphous layers	1210 ± 20	1119 nm	97 nm
1 undoped template layer, 10 doped annealed layers	1280 ± 50		
1 undoped template layer, 15 doped amorphous layers	1880 ± 20	1753 nm	107 nm
1 undoped template layer, 15 doped annealed layers	1290 ± 60		
1 undoped template layer, 20 doped amorphous layers	2380 ± 20	2266 nm	106 nm
1 undoped template layer, 20 doped annealed layers	2140 ± 30		

Examining the average thicknesses of the amorphous multi-layer films can provide insight into the average deposition thickness of films spun by dynamic deposition. An average single amorphous doped layer created by static deposition is approximately 250 nanometers. Subtracting that from the average thickness of the amorphous layer in the multi-layer film (column 3) allows for calculation of the average thickness of the dynamically deposited layers (column 4). The 10-, 15-, and 20-layer films all indicate an average dynamic deposition thickness near 100 nm, but the 5-layer films indicate a thickness of approximately 80 nm only. The 100 nm thickness is likely more reliable, as the 5-layer amorphous film sample is also thinner than the 5-layer annealed sample. This is inconsistent with the expectation that the thin films condense after crystallization, indicating that this sample may be an anomaly. It is worth pointing that the annealed 15-layer film is also drastically thinner than the amorphous 15-layer film in comparison to the general difference observed from other multi-layer films before and after hydrothermal annealing. As the 15-layer annealed film is much closer in thickness to the 10-layer films, there is a significant chance that there was an error with sample preparation. As

the samples may be taken from different locations on the coverslip substrate, a test may need to be performed to evaluate whether the thickness of the film is expected to be even across the entire expanse of the film. If films are consistently thicker in the center and thinner at the edge, the location of the measured section may matter significantly more than expected.

The SEM imaging of all multi-layered films displayed a grain texture change that represented crystallization throughout the entire film. In the 5-layer films, which are pictured at the same magnification as the single layer films, the change in texture is very apparent in a single set of SEM images. As can be seen below in Figure 5.25, the amorphous 5-layer film in Figure 5.25a has a very fine texture above the template layer, and the hydrothermally annealed film in Figure 5.25b has a uniform coarse texture which matches the template layer.

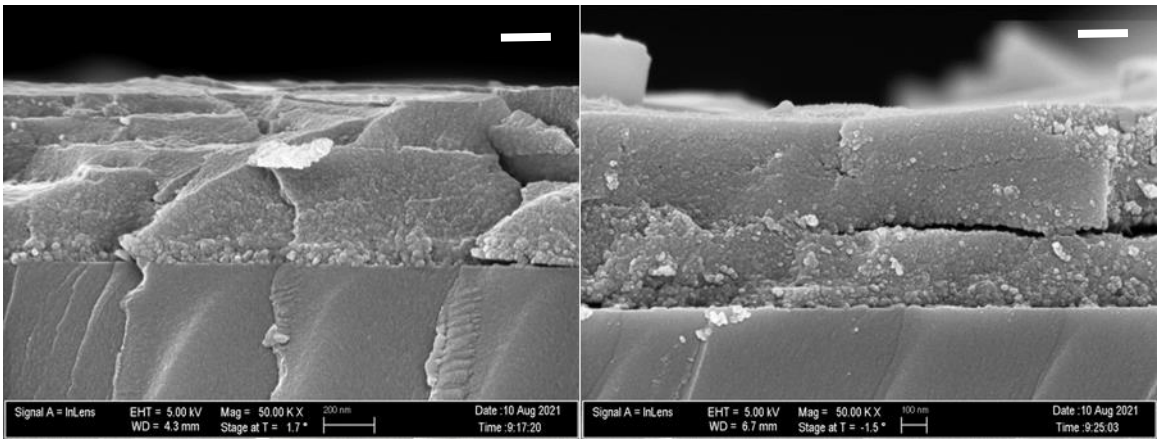

Figure 5.25 SEM images of a) amorphous and b) annealed 5-layer thin films. The white scale bars in the top right corner of the images represents a length of 200 nanometers.

The thicker multi-layer films were also analyzed via SEM imaging, to establish that full crystallization took place at each stage. While the textural difference is slightly more difficult to see at the lower magnifications necessary to view the full cross-section of the films, it does become clear when the magnification is increased to 50K×, the magnification used for the single

and 5-layer thin films. Figures 5.26 and 5.27 show the SEM imaging for the 10-layer TiO_2 thin films. Figure 5.26 shows the full cross-section of the 10-layer films before and after hydrothermal annealing at a 25K magnification. Figure 5.27 shows the top of the annealed 10-layer film at a 50K magnification.

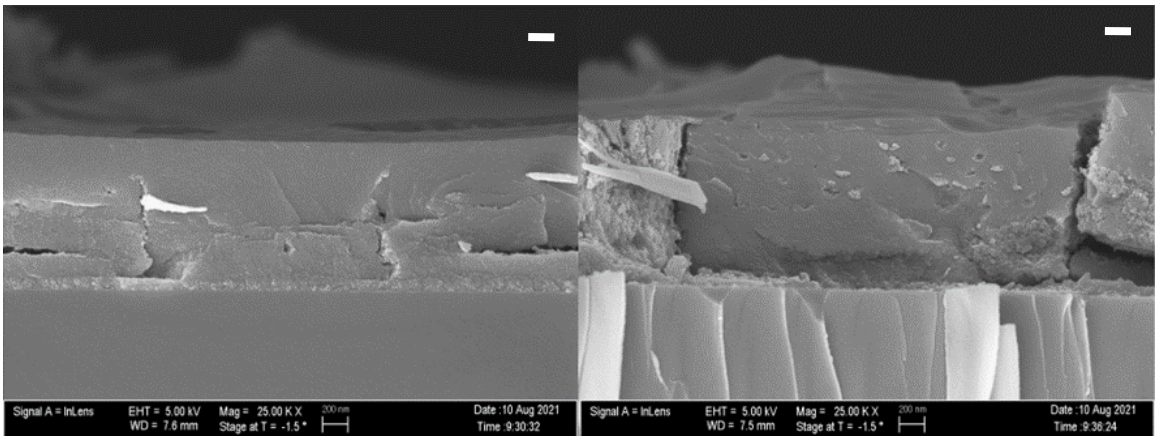

Figure 5.26 SEM images of a) amorphous and b) annealed 10-layer thin films. The white scale bars in the top right corner of the images represent a length of 200 nanometers.

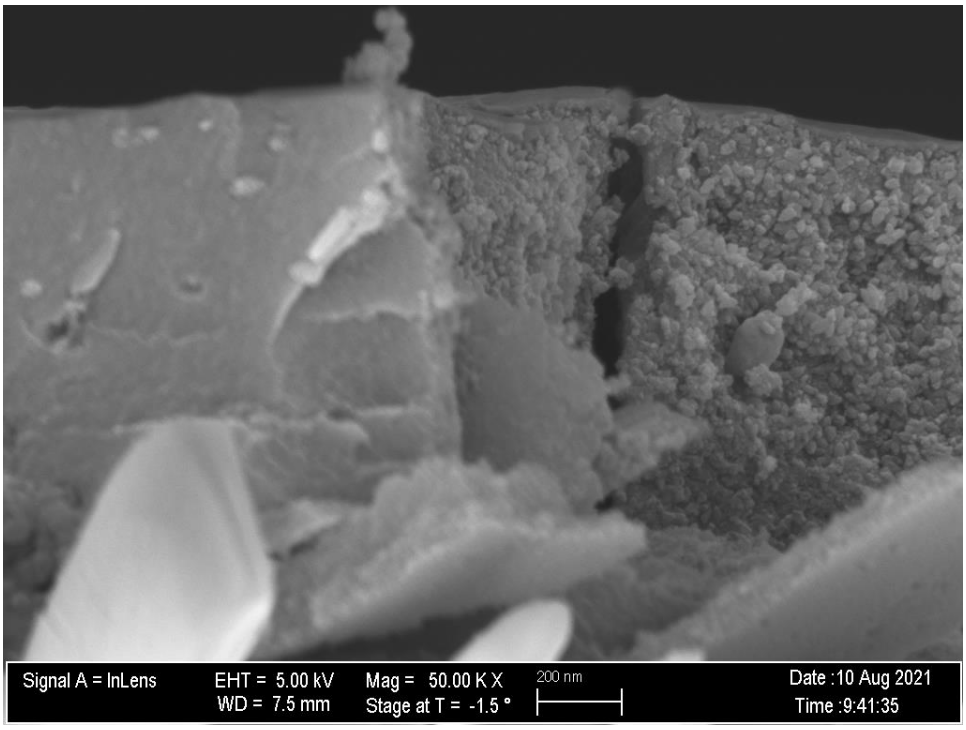

Figure 5.27 Texture of the top of the 10-layer annealed film at a 50K magnification.

At 50K magnification, it is clear that even at the top of the film, the film has taken on the coarse-grain texture distinctive of a crystalline film. Therefore, single-step hydrothermal annealing was successful for the 10-layer thin films.

15-layer thin films were also hydrothermally annealed in a single step and assessed with SEM imaging. Figure 5.28 displays 15-layer R6G-doped thin films before and after hydrothermal annealing at 25K magnification.

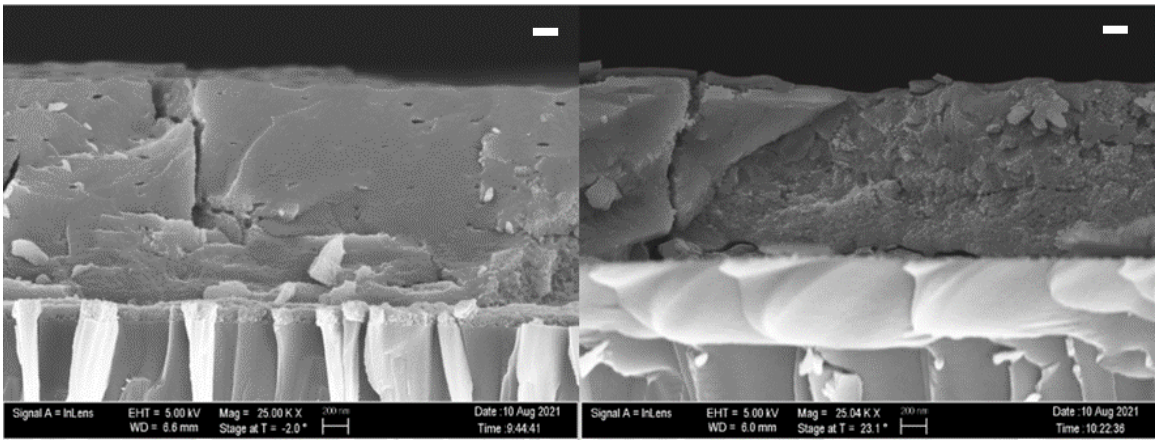

Figure 5.28 SEM images of a) amorphous and b) annealed 15-layer thin films at 25 K magnification. The white scale bars in the top right corner of the images represent a length of 200 nanometers.

Finally, 20-layer thin films were hydrothermally annealed in a single step and assessed with SEM imaging. Figure 5.29 displays the side-to side comparison of 20-layer R6G-doped thin films before and after hydrothermal annealing at a 20K magnification.

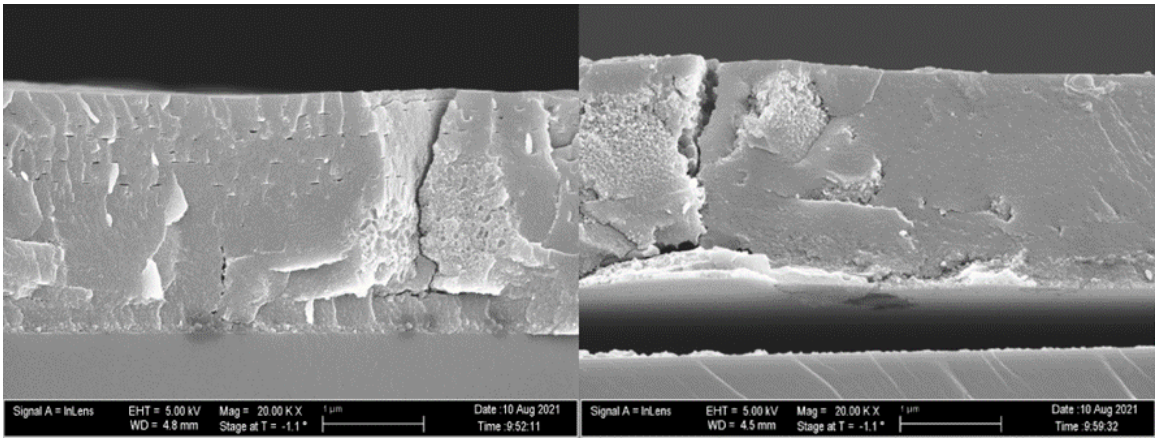

Figure 5.29 SEM images of a) amorphous and b) annealed 20-layer thin films at 20 K magnification. The scale bars displayed below the images represent a length of 1 μm.

As can be seen in Figure 5.30, the texture of the material has changed even in the very top of the 20-layer thin film, which has the same coarse grain size as the single-layer annealed films, even at nearly 2 μm away from the template layer.

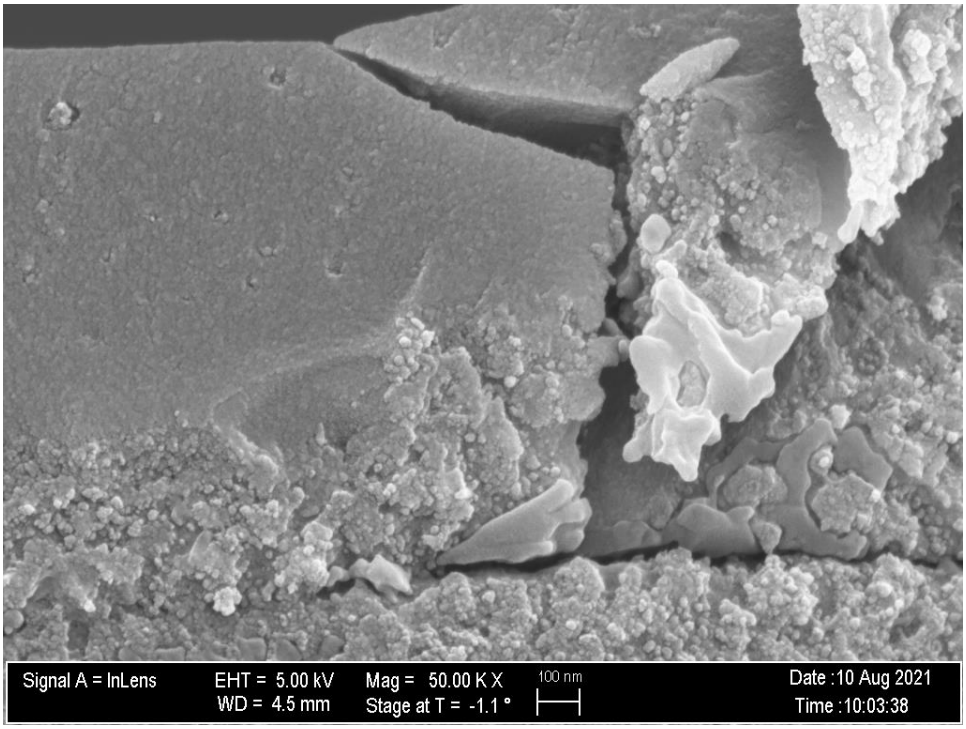

Figure 5.30 SEM image of the annealed 20-layer thin film at 50K magnification

Based on the XRD and SEM analysis, all thicknesses of anode material we created crystallized fully under the exact same hydrothermal annealing conditions. It is therefore confirmed that, for up to 20 layers, all hydrothermal processing can take place in a single step.

5.9 The Effect of Annealing Time in Hydrothermal Annealing

To establish a minimum hydrothermal annealing time for the complete crystallization of amorphous films, and to examine whether annealing time has any effect on the purity of crystal organization of the thin films, sets of 3 amorphous R6G loaded thin films with anatase template

layers were hydrothermal annealed for 1-8 hours under otherwise standard hydrothermal annealing conditions. Figures 5.31-5.33 detail the results of this experiment.

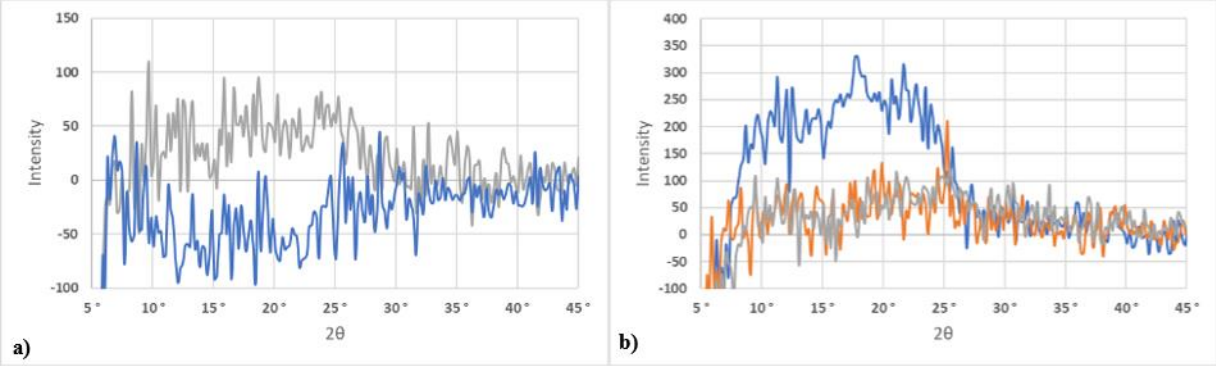

Figure 5.31 XRD difference spectra of replicate TiO_2 thin films that have undergone either a) 1 hour or b) 2 hours of hydrothermal annealing

As displayed in Figure 5.31, 1 and 2 hours of hydrothermal annealing did not produce any significant anatase peak at $2\theta = 25°$ in the difference spectra, indicating that no significant crystallization has yet occurred in the first two hours.

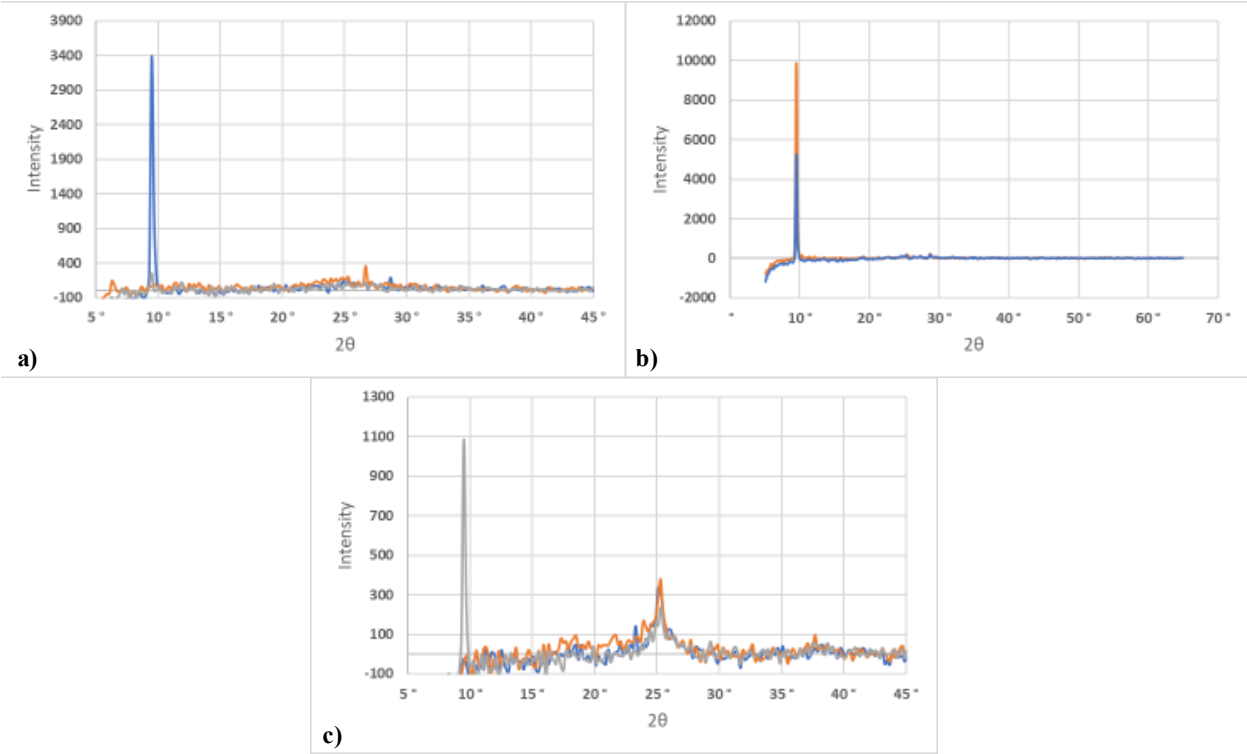

Figure 5.32 XRD difference spectra of replicate TiO_2 thin films that have undergone a) 3 hours, b) 4 hours, or c) 5 hours of hydrothermal annealing

Figure 5.32 displays the difference spectra for films that were hydrothermally annealed for 3-5 hours. These three tests each had at least one of the films display a noticeable main anatase peak intensity at $2\theta = 25°$ and the main H-titanate peak at $2\theta = 9.5°$, despite the strong variation in peak intensity between identically prepared samples. On the other hand, the second largest anatase peak at $2\theta = 38°$ is not discernable in these films. Therefore, while crystallization has begun, the variations in the crystallinity of films hydrothermally annealed for up to 5 hours is less than desirable.

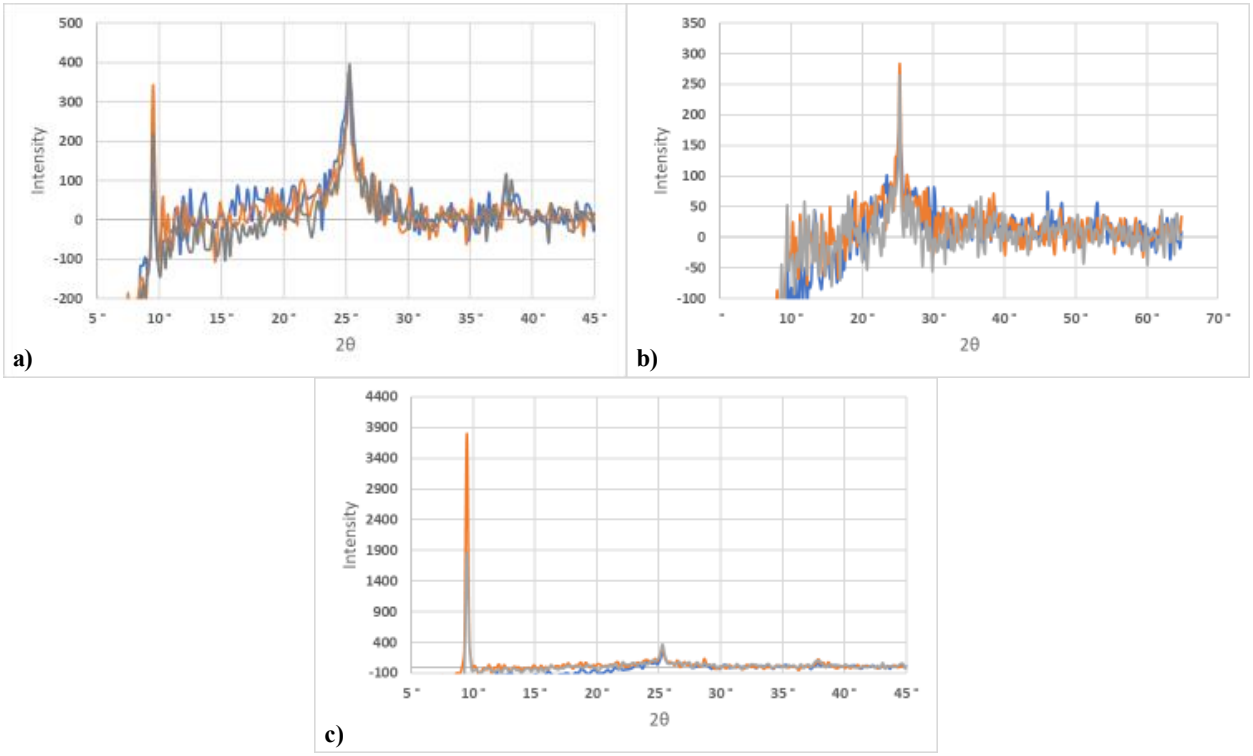

Figure 5.33 XRD difference spectra of replicate TiO_2 thin films that have undergone a) 6 hours, b) 7 hours, or c) 8 hours of hydrothermal annealing

The hydrothermal annealing times which resulted in more consistent crystallization are displayed in Figure 5.33. Six hours of hydrothermal annealing brought the H-titanate peaks down to the same scale as the anatase peaks, with very consistent intensity in the main anatase peak at 2θ = 25°. If the H-titanate peak intensity did not vary per film, 6 hours of hydrothermal annealing would have had the most consistent level of crystallinity across the annealing times tested. The films hydrothermally annealed for 7 hours all displayed both of the major anatase peaks at 2θ = 25° and 2θ = 38°. This set of samples may also display the minor anatase peaks at 2θ = 48° and 2θ = 54°, but the smaller peaks are difficult to distinguish from the noise. None of them display any other distinguishable peaks, indicating a pure anatase crystal organization for these three TiO_2 thin films. Films hydrothermally annealed at 8 hours displayed a strong H-titanate peak of

variable intensity at $2\theta = 9.5°$, along with a smaller, but more consistent anatase peak at $2\theta = 25°$. Even though the 25° anatase peak for the 8-hour films is more consistent than the H-titanate peak, both the 6-hour and 7-hour replicates had a tighter distribution. The average intensity of the $2\theta = 25°$ peak was 389 ± 6 for the 6-hour films, 260 ± 30 for the 7-hour films, and 310 ±70 for the 8-hour films.

8 hours of hydrothermal annealing was originally chosen due to being the maximum time allowed by the device. An 8-hour annealing time consistently displayed crystallization at the same peak locations, and no further crystallization appeared to take place after an additional 8-hour hydrothermal annealing time for a total of 16 hours of hydrothermal annealing. This specific trial of hydrothermal annealing three identically prepared films at once indicates that 6 or 7 hours of hydrothermal annealing may work as well or better. 6 hours of hydrothermal annealing resulted in the most consistent crystallinity across all films, with the highest intensity value at 25°. The 7-hour hydrothermally annealed films had a slightly lower intensity at 25°, and all three films exclusively display anatase titania diffraction peaks with relative consistency. If this representative crystal structure purity can be repeated, 7 hours may be the ideal hydrothermal annealing time for future experiments.

5.10 Conclusions

In this chapter, kinetically doped amorphous thin films are successfully transformed into crystallized thin films utilizing hydrothermal annealing when a single template layer of anatase titania is deposited first. The condensed thickness of this crystallized film retained 85% of the absorbed dye, resulting in a total concentration of 1.9 M R6G in the dye-containing layer of the dual-layer thin film. Crystallization is also achieved in films containing multiple dyes, though it is clear the presence of different dyes (R6G, Ru2, Nile blue) alters the distribution of crystal

forms within the film after hydrothermal annealing. Multi-layer samples of as many as 20 layers of amorphous film displayed relative consistency in film thicknesses for individual layers deposited, demonstrating that the thickness of anode can be tuned as needed. It is also observed that these multi-layer films can be crystallized in a single hydrothermal annealing step, simplifying the fabrication process. While multi-layered, kinetically doped films currently require a longer manufacturing time than other anode development methods, the low cost and environmentally friendly hyper-doped film fabrication method demonstrated here still make it an attractive potential anode material.

5.11 References

1. Park, N. G.; van de Lagemaat, J.; Frank, A. J., Comparison of Dye-Sensitized Rutile- and Anatase-Based TiO2 Solar Cells. *The Journal of Physical Chemistry B* **2000,** *104* (38), 8989-8994.

2. Sharma, S.; Bulkesh, S.; Ghoshal, S. K.; Mohan, D., Dye sensitized solar cells: From genesis to recent drifts. *Renewable and Sustainable Energy Reviews* **2017,** *70*, 529-537.

3. Khan, M. I.; Bhatti, K. A.; Qindeel, R.; Althobaiti, H. S.; Alonizan, N., Structural, electrical and optical properties of multilayer TiO2 thin films deposited by sol–gel spin coating. *Results in Physics* **2017,** *7*, 1437-1439.

4. Kumar, A.; Mondal, S.; Kumar, S. G.; Koteswara Rao, K. S. R., High performance sol–gel spin-coated titanium dioxide dielectric based MOS structures. *Materials Science in Semiconductor Processing* **2015,** *40*, 77-83.

5. Nishikiori, H.; Uesugi, Y.; Takami, S.; Setiawan, R. A.; Fujii, T.; Qian, W.; El-Sayed, M. A., Influence of Steam Treatment on Dye−Titania Complex Formation and Photoelectric Conversion Property of Dye-Doped Titania Gel. *The Journal of Physical Chemistry C* **2011,** *115* (6), 2880-2887.

6. Nishikiori, H.; Setiawan, R. A.; Kawamoto, S.; Takagi, S.; Teshima, K.; Fujii, T., Dimerization of xanthene dyes in sol–gel titania films. *Catalysis Science & Technology* **2013,** *3* (10), 2786-2792.

7. Sankapal, B. R.; Lux-Steiner, M. C.; Ennaoui, A., Synthesis and characterization of anatase-TiO2 thin films. *Applied Surface Science* **2005,** *239* (2), 165-170.

8. Taleb, A.; Mesguich, F.; Hérissan, A.; Colbeau-Justin, C.; Yanpeng, X.; Dubot, P., Optimized TiO2 nanoparticle packing for DSSC photovoltaic applications. *Solar Energy Materials and Solar Cells* **2016,** *148*, 52-59.

9. Germán, E.; Faccio, R.; Mombrú, A., A DFT + U study on structural, electronic, vibrational and thermodynamic properties of TiO 2 polymorphs and hydrogen titanate: tuning the Hubbard ' U -term'. *Journal of Physics Communications* **2017,** *1*, 055006.

10. Lu, S.-x.; Zhong, H.; Mo, D.-m.; Hu, Z.; Zhou, H.-l.; Yao, Y., A H-titanate nanotube with superior oxidative desulfurization selectivity. *Green Chemistry* **2017,** *19* (5), 1371-1377.

11. Avnir, D.; Kaufman, V. R.; Reisfeld, R., Organic fluorescent dyes trapped in silica and silica-titania thin films by the sol-gel method. Photophysical, film and cage properties. *Journal of Non-Crystalline Solids* **1985,** *74* (2), 395-406.

12. Domtau, D. L.; Simiyu, J.; Ayieta, E. O.; Nyakiti, L. O.; Muthoka, B.; Mwabora, J. M., Effects of TiO₂ Film Thickness and Electrolyte Concentration on Photovoltaic Performance of Dye-Sensitized Solar Cell. *Surface Review and Letters* **2017,** *24*, 1750065.

13. Kumari, K.; Sanjeevadharshini, N.; Dissanayake, L.; Senadeera, G. K. R.; Thotawatthage, C., The effect of TiO2 photo anode film thickness on photovoltaic properties of dye-sensitized solar cells. *Ceylon Journal of Science* **2016,** *45*, 33.

14. Jose, R.; Kumar, A.; Thavasi, V.; Ramakrishna, S., Conversion efficiency versus sensitizer for electrospun TiO₂nanorod electrodes in dye-sensitized solar cells. *Nanotechnology* **2008,** *19* (42), 424004.

15. Galliano, S.; Bella, F.; Gerbaldi, C.; Falco, M.; Viscardi, G.; Grätzel, M.; Barolo, C., Photoanode/Electrolyte Interface Stability in Aqueous Dye-Sensitized Solar Cells. *Energy Technology* **2017,** *5* (2), 300-311.

6. The Performance of Prototype Dye Sensitized Solar Cells

In this chapter, prototype DSSC anodes are created by creating the hyper-doped anode material established in chapters 3-5 on ITO plates instead of the coverslips used to establish the protocols. These were paired with a carbon-coated ITO plate cathode and an aqueous I^-/I_3^- electrolyte to create a complete prototype DSSC. The PCE of each of these devices is measured and the potential of the results discussed.

6.1 Anode Fabrication

The active anode material should not cover the entirety of the surface area of the ITO plates in order to provide a clean overhang which could be attached to the electrical leads. The anode also needed to be clean of the TiO_2 material on the sides, as the exact location and area covered by the spacers that prevent short circuiting is less quantifiable than having a clean edge with a defined active area. To create a specifically defined active area, the sides of the ITO plates were covered with masking tape prior to spin-coating to prevent sol-gel from condensing to that portion of the ITO plate. A 6 mm crafting tape was used to ensure a well-defined edge for the three sides which needed the ITO plate to be free of the TiO_2 film. A 3 mm crafting tape was used on the fourth side to confine the last edge of the active area. An even layer of tape across each side was used to ensure an even thickness across the film. With the reduced film area, the aliquot of aged sol-gel (See section 3.5 for recipe) also needed to be reduced. Instead of 120 μL, 80 μL aliquots were used for spin-coating each layer of film. The tape was applied immediately before spin-coating and removed immediately afterwards. Tape removal was performed while the ITO plate was still firmly secured inside the spin-coater by vacuum, resulting in a few

seconds of post spin-coat delay. Otherwise, anode material preparation followed the protocols laid out in Chapters 3-5. An image of the four types of 20-layer anodes is shown below in Figure 6.1.

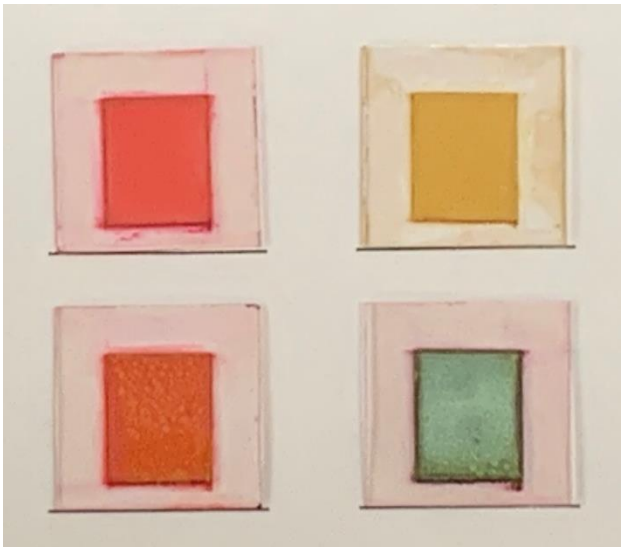

Figure 6.1 20-layer thin film anodes on ITO plates. R6G loaded on the top left, Ru2 loaded on the top right, Ru2/R6G loaded on the bottom left, and Ru2/R6G/Nile Blue on the bottom right.

6.2 DSSC Cell Construction

The parallel 6 mm clean edges of the anode were wrapped with thin strips of parafilm as a spacer to prevent short circuiting between ITO plates. The ITO plates used as cathodes were coated with carbon using a 2B pure-graphite woodless pencil. Binder clips were placed hold the anode and cathode ITO plates together where the pressure would fall on the parafilm edges. The 3 mm clean edge of the anode was the edge that overlapped the cathode ITO plate, with the larger 6 mm clean edge extending out as an overhang from the device. Figure 6.2 displays schematics of the top-down and cross-sectional diagrams of the prepared DSSC.

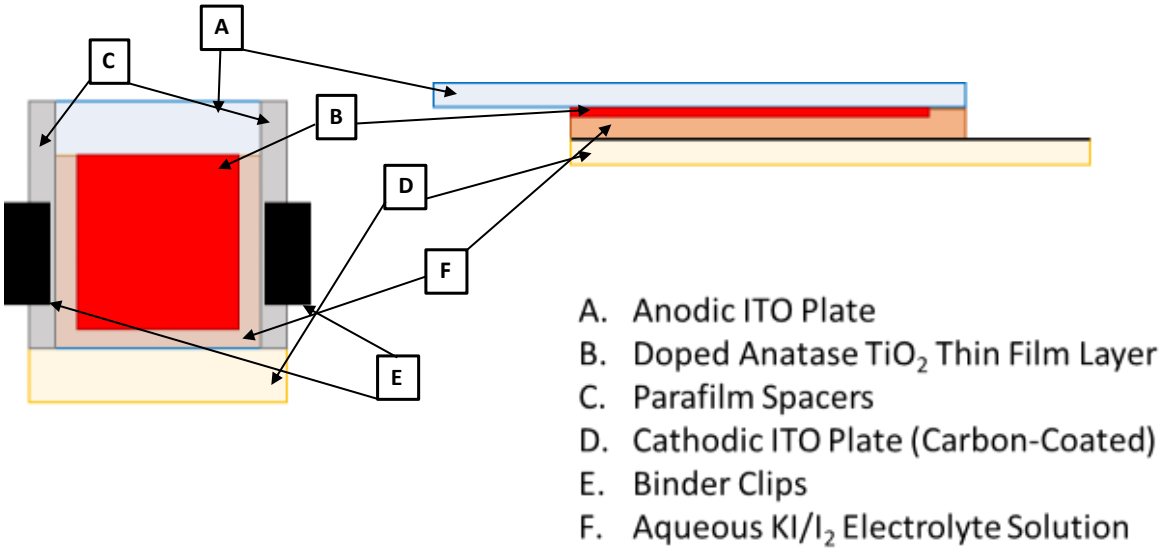

Figure 6.2 Schematics of prototype DSSCs. Top-down view on the left, cross-sectional view on the right.

Directly before measurement of the individual cell, the channel between the anode and cathode was filled with a redox electrolyte solution created from an aqueous mixture of 0.55M KI and 5 mM I_2. A micropipette was used to fill the channel between the two ITO plates. Kimwipes and cotton swabs were utilized to clean up any spillage before attaching the leads to take the measurement.

6.3 Efficiency Measurements of Prototype DSSCs

Anodes with 1-, 5-, 10-, 15-, and 20- layers of doped TiO_2 were prepared with the following dye solutions: 1 mM R6G, 1 mM Ru2, and a 1 mM Ru2/R6G mixture. A 20-layer anode was also prepared with a 1 mM Ru2/R6G/Nile blue mixture. Since exposure to the I^-/I_3^- electrolyte is

destructive to TiO_2 over time, the anodes were rinsed with water to remove the electrolyte and dried carefully after measurements.

Initial tests to qualitatively determine whether the prototype DSSCs would produce a measurable voltage were performed by taking the prototype cells outdoors and exposing them to direct sunlight. After using a multimeter to determine that the output of the DSSC was directly responsive to sunlight, the prototype DSSCs were subjected to quantitative power conversion efficiency (PCE) measurements.

PCE measurements were performed using a Kiethly source meter and a Newport Solar Simulator. The Newport Solar Simulator was set to produce irradiance according to the AM1.5 spectrum at a power density of 1000 $\frac{W}{m^2}$, and *I-V* data was taken for all prototype DSSCs. Figure 6.3 displays the *I-V* curve for the 20-layer R6G-loaded DSSC prototype. The black line shows the current measured as voltage increases, the grey line represents the power directly calculated

from the product of the voltage and current, and the red data point in the figure represents the P_{max}, which is used to determine the I_{max} and V_{max} for the calculation of PCE.

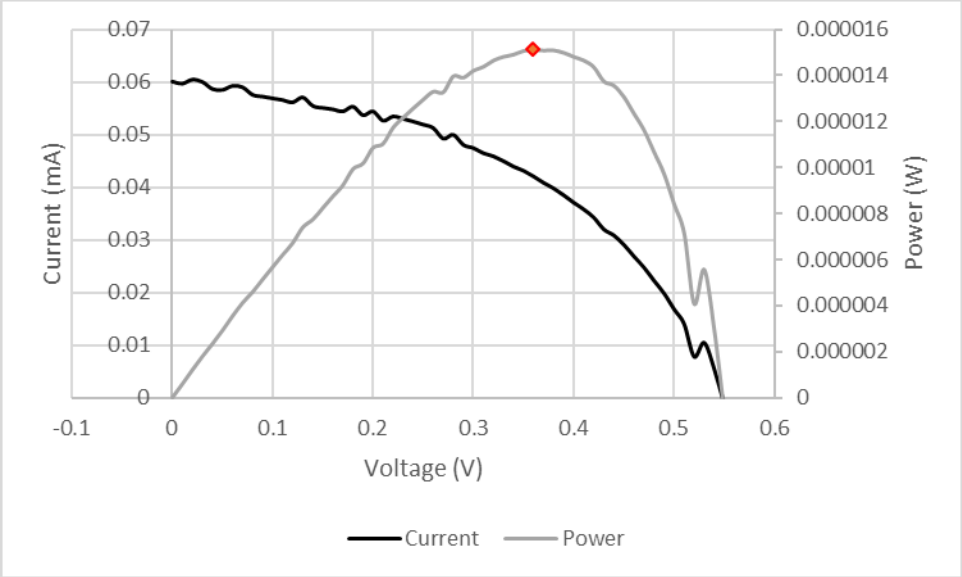

Figure 6.3 ***I-V*** Curve of R6G-Doped 20-layer prototype solar cell. The black line is current in mA, the grey line is the power output, and the red diamond is the P_{max} used to determine the V_{max} and I_{max}.

Using the following equations, previously seen in chapter 2, the PCE for each DSSC prototype was determined. The results of this calculation and the other data needed to calculate the PCE are summarized in Tables 6-1 to 6-4. The dimensions of the active area of each anode were approximately 16 mm ×13 mm, resulting in a 0.000208 m^2 active surface area and an illumination power (P_{in}) of 0.208 W.

$$FF(\%) = \left(\frac{V_{max} \times I_{max}}{V_{oc} \times I_{sc}}\right) \times 100\% \rightarrow \frac{FF(\%)}{100\%} = \frac{V_{max} \times I_{max}}{V_{oc} \times I_{sc}}$$

$$\rightarrow FF \times V_{oc} \times I_{sc} = V_{max} \times I_{max}$$

$$\eta(\%) = \left(\frac{V_{max} \times I_{max}}{P_{in}}\right) \times 100\% = \left(\frac{P_{out}}{P_{in}}\right) \times 100\%$$

The primary goal of testing anodes of the same material with multiple thicknesses was to determine whether the efficiency of the prototype DSSCs could be increased by increasing thickness. The literature makes clear that up until a certain threshold thickness, increasing the thickness will increase the efficiency because it increases the number of light-harvesting molecules.[1, 2] As most DSSCs range from 2-20 μm thick, it was hypothesized that for the thicknesses in use from 0.25-2.1 μm, the prototype DSSCs efficiency would increase with increasing thickness. Therefore, the first area of focus is to establish whether that proves to be the case for each set of films containing different dopants.

Table 6-1 *I-V* curve data and power conversion efficiencies of prototype solar cells containing only R6G.

Anode Description	V_{max}(V)	I_{max} (A)	P_{out} (W)	P_{in} (W)	η(%)
1 Layer	0.29	1.248E-05	3.620E-06	0.208	0.00174
5 Layers	0.34	2.244E-05	7.628E-06	0.208	0.00367
10 Layers	0.28	1.968E-05	5.511E-06	0.208	0.00265
15 Layers	0.25	2.077E-05	5.193E-06	0.208	0.00250
20 Layers	0.36	4.201E-05	1.512E-05	0.208	0.00727

Examining the R6G-doped anode data in Table 6-1, there is not a direct increase across each increasing thickness. All multi-layer anodes are significantly more efficient than the single-layer anode. Unfortunately, the 10- and 15- layer anodes are lower than the 5-layer anode without any clear explanation as to why.

Table 6-2 *I-V* curve data and power conversion efficiencies of prototype solar cells containing only Ru2. A * by the film description indicates that the shape of the *I-V* curve is very irregular.

Anode Description	V_{max}(V)	I_{max} (A)	P_{out} (W)	P_{in} (W)	η(%)
1 Layer	0.16	1.451E-05	2.322E-06	0.208	0.00112
5 Layers*	0.13	1.050E-05	1.365E-06	0.208	0.00066
10 Layers	0.28	1.968E-05	5.511E-06	0.208	0.00265
15 Layers*	0.1	1.029E-05	1.029E-06	0.208	0.00049
20 Layers*	0.23	1.047E-05	2.409E-06	0.208	0.00116

The Ru2 loaded films did not align with the expectation that efficiency would increase with increasing thickness, if the efficiency data in the table was the only information provided. This data would lead to the belief that the Ru2 anode had reached the point where scattering loss begins to outpace the gain in electron injection at 10 layers. However, only the 1- and 10- layer anodes are considered to have reliable data.

When the films containing Ru2 alone were analyzed, most of the *I-V* curves had very irregular shapes. The *I-V* curve in Figure 6.4 for the 20-layer Ru2 prototype DSSC demonstrates the irregularity that the Ru2 DSSCs display. Due to these irregularities in their *I-V* curves, the efficiencies for the 5-, 15- and 20- layer films containing only Ru2 are considered less trustworthy.

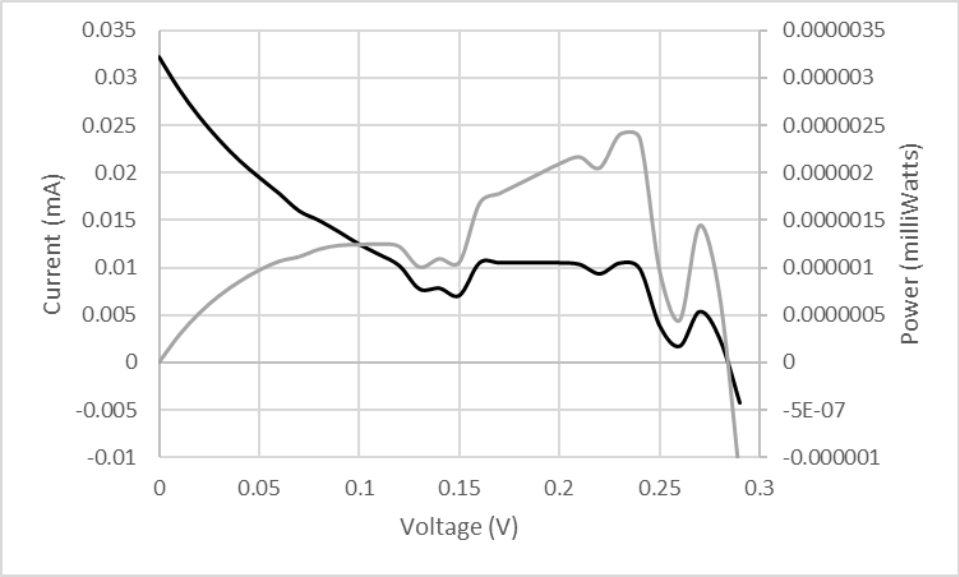

Figure 6.4 *I-V* curve for the 20-layer Ru2-doped prototype solar cell. The black line is current in mA, and the grey line is the power output.

Examining just the 1- and 10- layer anodes containing Ru2, which had more standard *I-V* curves, the increase in efficiency is similar to what is seen in the R6G-loaded anodes. However, based on the irregularities of the rest of the Ru2 film *I-V* curves, no strong conclusions can be drawn for the efficiency correlation with thickness based on the Ru2 anodes. It is worth pointing out that films containing Ru2 alone exhibit poor mechanical stability. Thus, it is quite possible that the irregular device performance may stem from the poor mechanical stability of the anode material.

Table 6-3 *I-V* curve data and power conversion efficiencies of prototype solar cells containing an Ru2/R6G mixture.

Anode Description	V_{max}(V)	I_{max} (A)	P_{out} (W)	P_{in} (W)	η(%)
1 Layer	0.17	1.281E-05	2.177E-06	0.208	0.00105
5 Layers	0.22	1.823E-05	4.011E-06	0.208	0.00193
10 Layers	0.28	2.449E-05	6.858E-06	0.208	0.00330
15 Layers	0.3	2.715E-05	8.145E-06	0.208	0.00392
20 Layers Sample 1	0.31	2.504E-05	7.763E-06	0.208	0.00373
20 Layers Sample 2	0.45	3.820E-05	1.719E-05	0.208	0.00826

The prototype anodes containing a mixture of R6G and Ru2, presented in Table 6-3, display a more consistent generally upward trend in PCE with increasing thickness, moving from 0.00105% for a 1-layer anode to an average of 0.005995% for the 20-layer anode prototypes. However, the only sample with two prototypes, the 20-layer Ru2/R6G loaded anodes, differed in a final efficiency by more than a factor of two. This clear inconsistency in device performance when the devices were constructed from otherwise identically prepared anodes displays a need to significantly change one step of DSSC fabrication in future experimentation. The current cathode preparation procedure utilizes a graphite pencil on the ITO plate, which made it impossible to be certain of equivalent preparation. While further tests have not been performed using the solar simulator, tests using direct sunlight and a multimeter have displayed improved consistency when using a graphite sheet as the cathode. A second method to insure a consistent cathode for future experiments would be to utilize the spin-coating method of covering an ITO plate in carbon black as described by Liu.[3]

Table 6-4 I-V curve data and power conversion efficiencies of prototype solar cells containing an Ru2/R6G/Nile blue mixture.

Anode Loaded with Ru2/R6G/Nile Blue Mixture					
20 Layers	0.27	2.856E-05	7.710E-06	0.208	0.00371

As shown in Table 6-4, the anode loaded with R6G, Ru2, and Nile blue at once still displayed a higher efficiency than any of the single-layer anodes but is lower than what was achieved by the R6G-doped 20-layer sample and the more efficient R6G/Ru2-doped 20-layer sample. Although there is only one three-dye sample, this additional lower efficiency value for a 20-layer sample may well be due to inconsistency in cathode preparation, supporting the conclusion that a more reliable cathode preparation method is needed to improve device performance in future.

6.4 Possible Reasons for the Overall Low Power Conversion Efficiency

After discussing the consistency of the values in the tables above, it is important to acknowledge the absolute values of the efficiency numbers in the table. It is obvious that all of the efficiencies are rather low. The very highest PCE achieved in this work was 0.00826%, which was found in one of the Ru2/R6G loaded 20-layer films. At first glance, these seem to be disappointing results when compared to the high efficiencies of 7-13.6% found in literature as listed in chapter 2. However, because many other components in the prototype DSSCs were not optimized, the results are far less disappointing than they appear.

6.4.1 The Effect of the Aqueous Redox Electrolyte

The redox electrolyte used in these prototype solar cells is an aqueous I^-/I_3^- electrolyte, as the kinetically doped films are known to resist dye leaching in water for up to several hours. Examining the literature, the highest efficiencies produced using a primarily aqueous electrolyte

solution are still under 4%.[4, 5] In fact, the majority of DSSCs utilizing aqueous electrolytes have much lower efficiencies, ranging from 0.5% to 2%.[4] The efficiency of a TiO_2 DSSC using an aqueous 5.5 M KI and 50 mM I_2 solution that is similar to our electrolyte solution, had a PCE of 0.73% in a 2016 study with even lower PCE measured at lower I_2 concentrations.[6] In a separate study in 2017, an aqueous electrolyte solution created from 0.5 M NaI and 25 mM I_2 resulted in 0.004-0.2% efficiency, depending on the dye sensitizer used.[7] The redox electrolyte solution used in this work was an aqueous solution containing 0.55 M KI and 5 mM I_2 with no other additives. Even with high efficiency sensitizers, the expectation for the prototype DSSC should not be higher than 0.1%, the efficiency of most of the high-efficiency dyes in the 2017 study. While 0.00826% is still an order of magnitude smaller, the limitations of the redox electrolyte chosen in this work starts to put the apparently poor efficiencies attained by the prototype into a more realistic perspective.

6.4.2 The Effect of Dyes Chosen for Light Sensitizers on PCE

Even taking the redox electrolyte into account, the highest efficiency produced by these prototypes is still an order of magnitude lower than those accomplished in the literature. Other factors are certainly at play. Once such factor that is critical to DSSC performance is the choice of dye sensitizer. The dyes loaded into TiO_2 thin films were selected based on likely initial success with kinetic doping and some prior usage in DSSCs. As such, they are unlikely to be among the most efficient dyes used for DSSCs. D131, the dye that reached a 0.2% efficiency in the aqueous electrolyte study using 0.5 M NaI and 25 mM I_2, can reach up to 5% efficiency in an acetonitrile I^-/I_3^- electrolyte in the presence of other additives.[7, 8] The reported literature efficiency for a 5 μm thick anode loaded with Ru2 with an ethylene glycol based I^-/I_3^- electrolyte is only 0.25%.[9] As for R6G, although a comparable use of R6G in a TiO_2 anode could not be

found, an efficiency of 4% for R6G-doped Fe_2O_3 anodes with an I^-/I_3^- electrolyte DSSC was reported.[10] With these limitations of the dyes chosen, our prototype being within an order of magnitude of known moderately efficient dyes in the same electrolyte we used is very encouraging.

6.4.3 The Effect of Anode Thickness

The thickness of the anode is likely also influencing the final measured efficiency. In the two D131 doped anodes discussed before, the 0.2% efficient anodes with an aqueous solvent were approximately 6 μm thick, and the 5% efficient anodes with an acetonitrile solvent were approximately 20 μm thick. The anode with the highest efficiency anode in this work was only 2 μm thick. While our study does not demonstrate a firm correlation between increased thickness and final efficiency, the 2 μm thick 20-layer films were consistently more efficient than the approximately 0.25 μm thick 1-layer anodes. There is a significant possibility that the efficiency may continue to increase even further in anodes consisting of even more layers.

6.4.4 The Effect of Cathode Materials on PCE

While the focus of this work was not on the cathode, the efficiency of the prototype DSSCs could certainly be improved with a more efficient and reliable cathode material. Based on the literature previously discussed in chapter 2, the expectation is that changing the cathode to a spin-deposited carbon black electrode would also raise the PCE significantly even without changing anything else.[3] More importantly, it would allow for a far more consistent cathode than the graphite pencil technique used in the prototype DSSC fabrication process reported here. In principle, a more consistent cathode material may not improve PCE, but would almost certainly

allow for a more reliable comparison of the anode efficiencies. Therefore, this alteration is worth making in future studies even if it does not end up increasing the overall DSSC efficiency.

6.5 Dye Leaching Study

While a more consistent cathode will help with consistency between samples, the breakdown of factors hampering the efficiency discussed in section 6.4 also clearly indicate that the redox electrolyte needs updating. Based on the literature, acetonitrile and ethylene glycol are both more effective electrolyte solvents than water.[4] However, for these solvents to be a viable alternative for our anode materials, there needs to be minimal dye leaching from the thin film to the redox electrolyte.

To this end, films loaded with R6G were used to evaluate the level of dye leaching over time. This was done by placing the films into 5 mL of solvent and sampling the absorbance of the solvent at set time intervals. Amorphous R6G-doped films and R6G-doped films that were hydrothermally annealed and subsequently heated at 150°C for 1 hour were tested simultaneously in separate solutions. The first leaching experiment was done with Millipore water as a control, to establish the level of dye leaching in the electrolyte solvent currently in use. Figure 6.5 displays the absorbance of the aqueous solution at 519 nm at various time intervals, with the black data points representing the solution containing the amorphous film and the red data points representing the solution containing the annealed film.

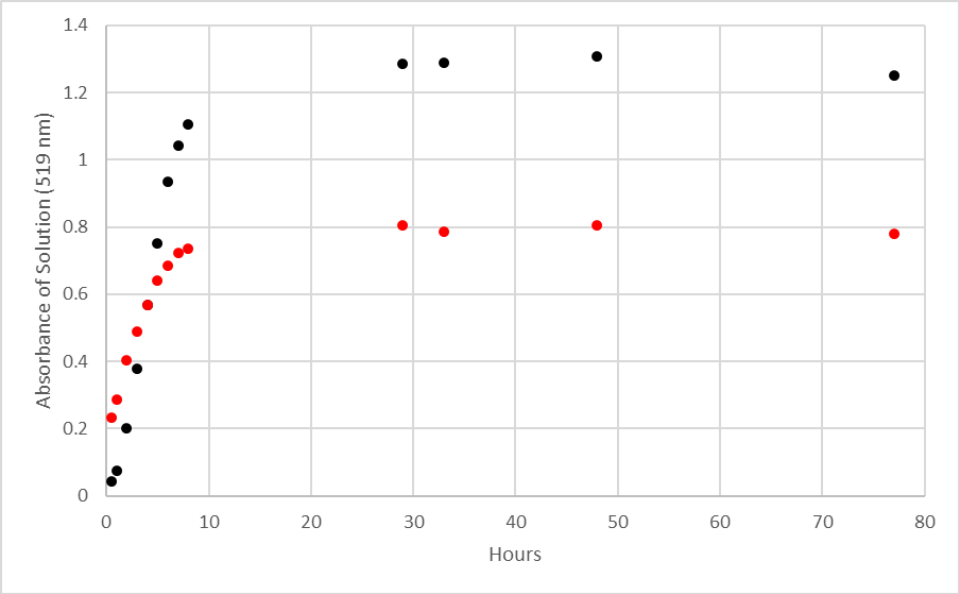

Figure 6.5 Absorbance of aqueous solution used to leach dye from the film at 519 nm vs. time. Black data points belong to the solution containing an amorphous R6G-doped TiO_2 film, red data points belong to the solution containing an annealed R6G loaded TiO_2 film.

While there was some dye leaching even at the beginning, it took over eight hours for the majority of the removable dye to enter the solution. As time went on, the absorbance of the solution leveled off, indicating that after approximately 24 hours, the overwhelming majority of the dye leaching that would occur had taken place. The overall level of dye leaching was evaluated by taking the UV-Vis spectrum of the thin films before and after the dye leaching experiment. This set of spectra is displayed in Figure 6.6.

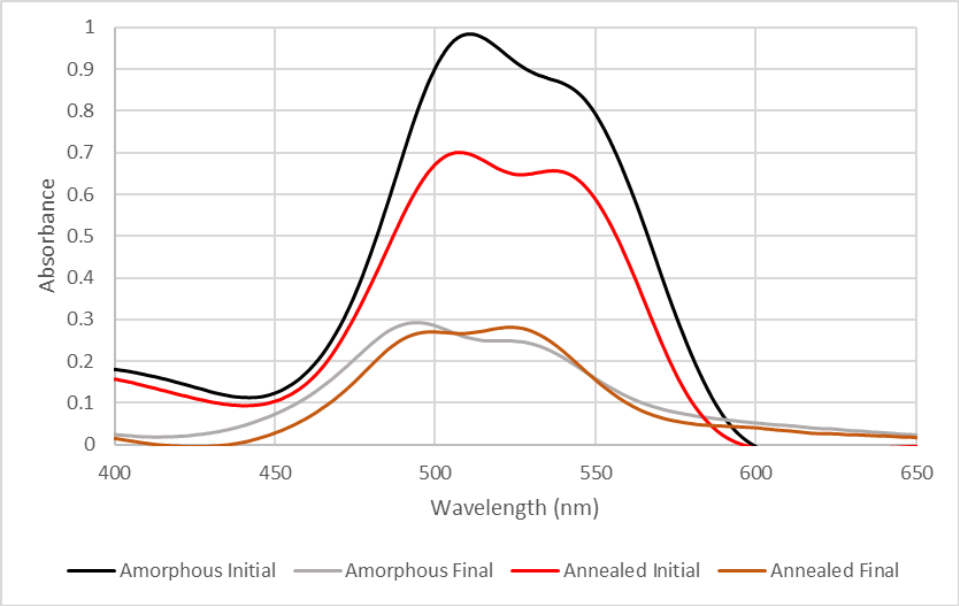

Figure 6.6 UV-Vis absorbance spectra of the amorphous and annealed R6G-doped TiO_2 thin films that were submerged in 5 mL of Millipore water for 77 hours. The black line is the amorphous film before extraction, and the grey line is the same amorphous film after extraction. The red line is the annealed film before extraction, and the brown line is the same annealed film after extraction.

As seen in Figure 6.6, after three days submerged in water, both the amorphous R6G-doped film and the hydrothermally annealed R6G-doped film had released significant amounts of dye. Yet, both retained sufficient dye to have an absorbance of approximately 0.3. This indicates that while dye is leached from the film, there is still a considerable amount of dye permanently trapped inside the film.

A second set of films identically prepared was submerged in ethylene glycol for 28 hours. Figure 6.7 shows that the absorbance of these solutions. While the amorphous film lost dye at a

relatively steady rate, the annealed film lost a significant majority of the dye within the first hour in solution.

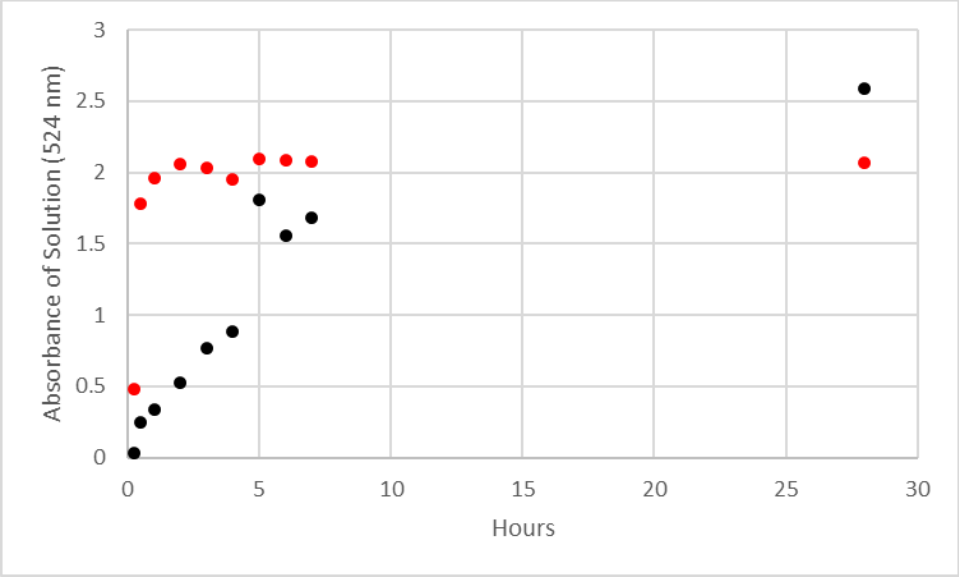

Figure 6.7 Absorbance of ethylene glycol solution used to leach the dyes from the films at 524 nm vs. time. Black data points belong to the solution containing an amorphous R6G loaded TiO_2 film, red data points belong to the solution containing an annealed R6G loaded TiO_2 film.

Based on the UV-Vis absorbance spectra of the amorphous and annealed films before and after the dye leaching study in Figure 6.8, it is likely that the absorbance of the ethylene glycol solution would have leveled off after the first day, if only because most of the dye had already been extracted from the films. After one day in ethylene glycol, the final absorbance of the R6G-doped films has dropped to 0.1, in comparison to the 0.3 for aqueous dye leaching. These results indicate that ethylene glycol is not a realistic replacement solvent for our anode materials.

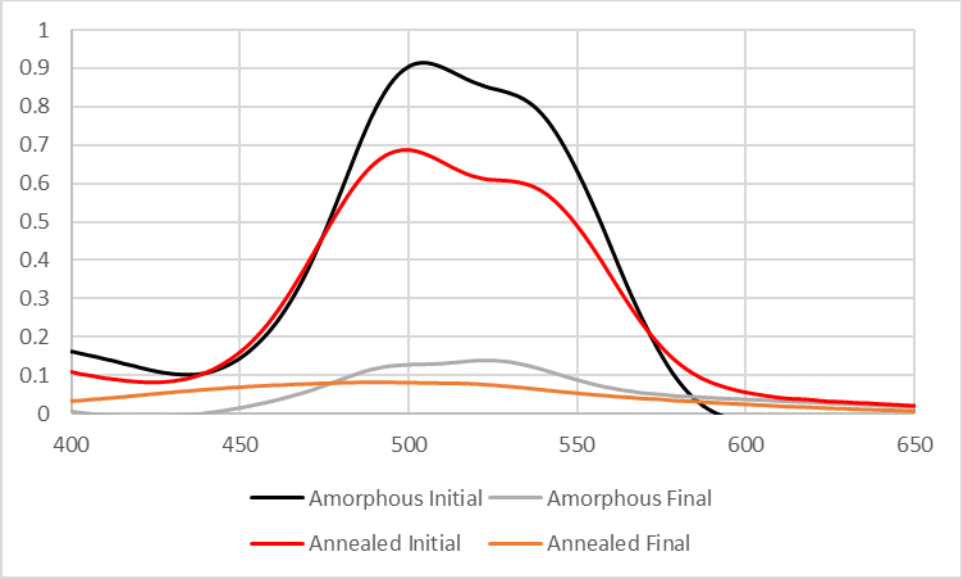

Figure 6.8 UV-Vis absorbance spectra of the amorphous and annealed R6G-doped TiO_2 thin films that were submerged in 5 mL of ethylene glycol for 28 hours. The black line is the amorphous film before extraction, and the grey line is the same amorphous film after extraction. The red line is the annealed film before extraction, and the brown line is the same annealed film after extraction.

Acetonitrile was also tested as a potential replacement solvent. Figure 6.9 displays the absorbance vs. time data for the acetonitrile solutions containing amorphous and annealed R6G loaded films. Both solutions displayed more rapid leaching than water, reaching the point where the majority of the removable dye was in solution in around 5 hours as opposed to 8. However, the overall absorbance of the solution for the amorphous film remained relatively low compared to the other tests, even after two days.

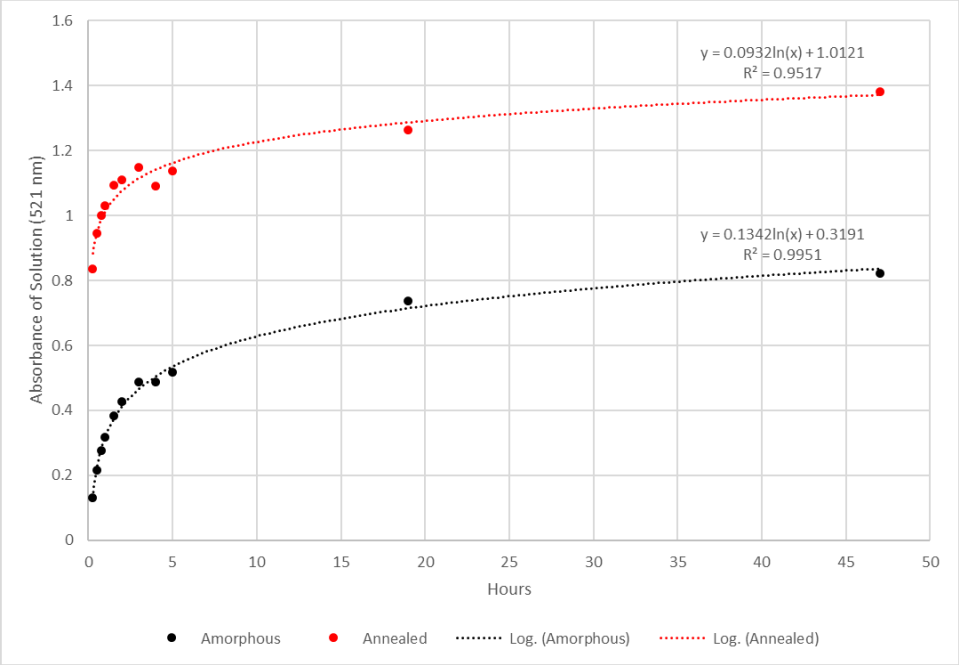

Figure 6.9 Absorbance of acetonitrile solution used to leach dye from the films at 521 nm vs. time. Black data points belong to the solution containing an amorphous R6G loaded TiO_2 film, red data points belong to the solution containing an annealed R6G-doped TiO_2 film.

In the UV-Vis spectra of the initial and final states of the thin films that were leached in acetonitrile, shown in Figure 6.10, it becomes clear why the absorbance of the amorphous solution is so low even after two days. Unlike the rest of the tests, the majority of the dye was still retained within the amorphous film, giving it a final absorbance of around 0.6 after two full days in acetonitrile. The annealed film retained an absorbance around 0.2, indicating more dye leaching in the annealed film, but less than what was seen in ethylene glycol.

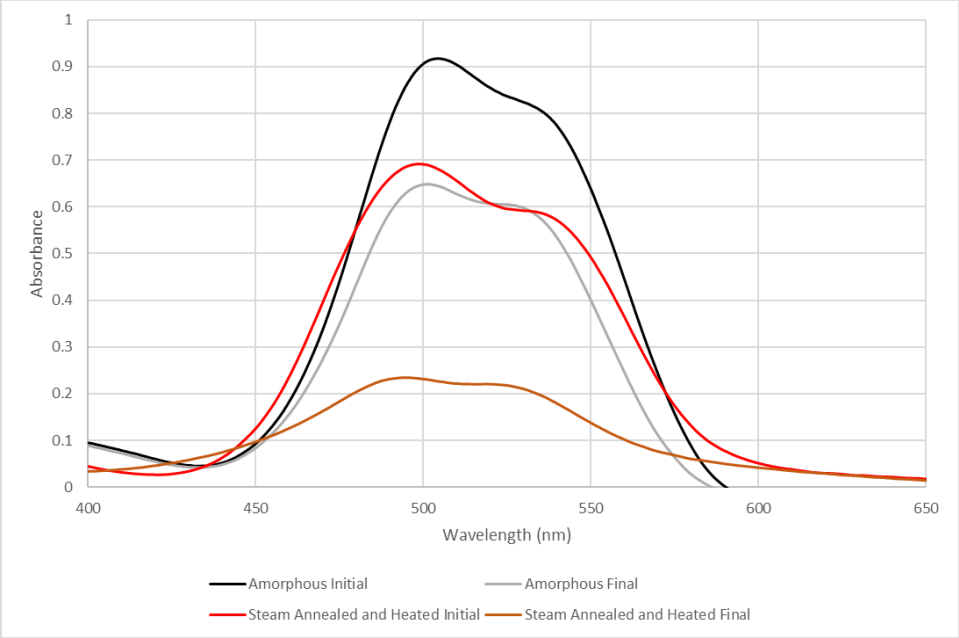

Figure 6.10 UV-Vis absorbance spectra of the amorphous and annealed R6G-doped TiO_2 thin films that were submerged in 5 mL of acetonitrile for 47 hours. The black line is the amorphous film before extraction, and the grey line is the same amorphous film after extraction. The red line is the annealed film before extraction, and the brown line is the same annealed film after extraction.

Based on these tests, it seems that water is still the best solvent from a dye-leaching perspective. Looking at literature based on relatively similar DSSCs to those in this work, the DSSC with aqueous electrolyte had a PCE of 0.2% and the DSSC using an acetonitrile electrolyte had a PCE of 5%.[7, 8] Because the acetonitrile solvent displayed significantly less dye leaching in the amorphous film, and the annealed film retained more dye than the film in ethylene glycol, it may be worth experimenting with acetonitrile solvents or a mixture of acetonitrile and water to see if the PCE can be improved without significantly increasing dye leaching.

6.6 Conclusions

The highest PCE achieved by the prototype DSSCs was 0.00826%, approximately an order of magnitude smaller than the highest PCE that could have been expected based on the aqueous electrolyte used. Alterations to the cathode preparation protocol would likely increase both the overall efficiency and consistency in PCE between samples. The recommended new protocol is

the deposition of carbon black via spin-coating. Experiments to determine dye leaching parameters in ethylene glycol and acetonitrile were performed. While the results of these experiments indicate that water is the best solvent to minimize dye leaching in the annealed films, there is a chance that an acetonitrile solvent or a solvent partially composed of acetonitrile may increase the PCE without overly increasing dye leaching. Overall, the DSSCs produced demonstrate a successful prototype anode material, though at a maximum thickness of ~2 μm we may not yet have reached the optimal thickness.

6.7 References

1. Lee, H.; Kim, J.; Kim, D. Y.; Seo, Y., Co-sensitization of metal free organic dyes in flexible dye sensitized solar cells. *Organic Electronics* **2018,** *52*, 103-109.

2. Domtau, D. L.; Simiyu, J.; Ayieta, E. O.; Nyakiti, L. O.; Muthoka, B.; Mwabora, J. M., Effects of TiO₂ Film Thickness and Electrolyte Concentration on Photovoltaic Performance of Dye-Sensitized Solar Cell. *Surface Review and Letters* **2017,** *24*, 1750065.

3. Liu, I. P.; Hou, Y.-C.; Li, C.-W.; Lee, Y.-L., Highly electrocatalytic counter electrodes based on carbon black for cobalt(iii)/(ii)-mediated dye-sensitized solar cells. *Journal of Materials Chemistry A* **2017,** *5* (1), 240-249.

4. Kim, J.-H.; Kim, D.-H.; So, J.-H.; Koo, H.-J., Toward Eco-Friendly Dye-Sensitized Solar Cells (DSSCs): Natural Dyes and Aqueous Electrolytes. *Energies* **2022,** *15* (1).

5. Vaghasiya, J. V.; Nandakumar, D. K.; Yaoxin, Z.; Tan, S. C., Low toxicity environmentally friendly single component aqueous organic ionic conductors for high efficiency photoelectrochemical solar cells. *Journal of Materials Chemistry A* **2018,** *6* (3), 1009-1016.

6. Bella, F.; Galliano, S.; Falco, M.; Viscardi, G.; Barolo, C.; Grätzel, M.; Gerbaldi, C., Unveiling iodine-based electrolytes chemistry in aqueous dye-sensitized solar cells. *Chemical Science* **2016,** *7* (8), 4880-4890.

7. Galliano, S.; Bella, F.; Gerbaldi, C.; Falco, M.; Viscardi, G.; Grätzel, M.; Barolo, C., Photoanode/Electrolyte Interface Stability in Aqueous Dye-Sensitized Solar Cells. *Energy Technology* **2017,** *5* (2), 300-311.

8. Jose, R.; Kumar, A.; Thavasi, V.; Ramakrishna, S., Conversion efficiency versus sensitizer for electrospun TiO₂nanorod electrodes in dye-sensitized solar cells. *Nanotechnology* **2008,** *19* (42), 424004.

9. Hurtado-Morales, M.; Pazos-Alonso, J. E.; Garcia-Fox, M. A.; Castarlenas, S.; Téllez, C.; Coronas, J. In *Structural characterization of Graphene Oxide and Reduced Graphene Oxide used as counter electrode in flexible DSSC*, 2018 IEEE 7th World Conference on Photovoltaic Energy Conversion (WCPEC) (A Joint Conference of 45th IEEE PVSC, 28th PVSEC & 34th EU PVSEC), 10-15 June 2018; 2018; pp 1116-1121.

10. Hussain, D. H.; Abdulah, H. I.; Rheima, A. M., Synthesis and characterization of ɣ-Fe2O3 nanoparticles photo anode by novel method for dye sensitized solar cell. *International Journal of Scientific and Research Publications* **2016,** *6* (10), 26-31.

Appendix I

I. Manuscript Submission Details

A manuscript containing the data previously expounded upon in chapters 4-6 was submitted to the *Journal of Sol-Gel Science and Technology*. While the JSGST ultimately rejected the manuscript, the reviewer comments were helpful to update and add details to both this work and a revised manuscript which is currently submitted to the *Journal of Electronic Materials*. The reviewer comments and how they were ultimately addressed in the resubmitted manuscript are summarized below.

Reviewer 1

This reviewer appeared to be supportive of the manuscript overall but felt the formatting of the figures needed to be improved. The exact comment is below:

"*Fig.2 and Fig. 4-10 should be improved. The letter and number in the figures should be clear, uniform, and enough large for being seen easily.*"

In order to address this, the labeling in all graphs was edited to make sure the text was easily legible.

Reviewer 5

This reviewer had more issues with the manuscript and strongly recommended against acceptance. Their comments on the manuscript were:

"*This manuscript describes that fabrication and solar cell application of dye(s)-doped titania thin films using hydrothermal annealing. Fabrication processes and characterization are described in detail very much, which are almost enough to reproduce the present materials.*

While, I think that solar cell performance using the present dye-doped titania materials are very low to discuss the effect of dye-doping. In addition, the discussion about photoelectric conversion properties are rough comparing with the fabrication and characterization parts of this manuscript. In future, if you plan to improve discussion about photoelectric conversion properties, irradiation wavelength dependence of photocurrent is mandatory.

I strongly recommend redesign the structure of the manuscript or improving photoelectric conversion performance enough to discuss, quantitatively. Moreover, quality of absorption spectra (no units are indicated) and SEM image (clear scale bars are needed) must be improved to publish as academic paper."

Reading through this review, the four primary issues the reviewer had with the manuscript were:

(i) the low numerical value of photoelectric conversion efficiency

(ii) limited detail in the discussion of the solar cell performance

(iii) the lack of irradiation wavelength dependent efficiency measurement

(iv) separate small issues with the figure formatting than Reviewer 1 had addressed

To address concern (i) there was not much that could be done. The PCE values of our device cannot be increased using the materials currently in the prototype solar cells. However, we added a significant explanation that was not previously in the manuscript which compares our values to DSSCs utilizing aqueous redox electrolytes similar to the one used in our prototypes. This section explains why our values, though numerically low, are still significant in the field.

Upon reflection, we agreed with Reviewer five on concern (ii), the solar cell efficiency section of the manuscript had the least amount of detail in the manuscript. We updated the manuscript that

was submitted to the Journal of Electronic Materials to include significantly more detail in both the setup of the prototype cell and elaborated on the discussion of our values and overall results. The detail in this portion of the manuscript is now much closer to that represented in the rest of the manuscript.

As for concern (iii), it is impossible for us to address the concern in the manner suggested by the reviewer given the low PCE values of our devices. There is now an explicit statement in the manuscript stating that while it would be ideal to measure irradiation-specific efficiency, it is not possible with these prototypes based on the low absolute value of the PCE.

Finally, to address concern (iv), the figure formatting was addressed. All graph axes were updated to include the necessary units and more visible scale bars were embedded into the SEM images.

II. Acknowledgements

Dr. Bayram Saparov allowed for the use of his Rigaku Miniflex600 Benchtop X-Ray Diffractometer and zero-background plate to collect the XRD spectra of thin films at various stages of crystallization. Dr. Rachel Roccanova and Tielyr Creason, members of his research group, were especially helpful in regard to answering countless scientific questions.

Dr. Preston Larson of the Samuel Roberts Noble Microscopy Laboratory at the University of Oklahoma did the necessary sputter-coat preparation of samples for SEM imaging and assisted with the collection of all SEM data.

Dr. Ian Sellers of the Physics department at the University of Oklahoma allowed for the use of his Kiethly source meter and Newport solar simulator to measure the PCE of the prototype solar cells. Dr. Vincent Whiteside, a member of Dr. Sellers' group, provided specific direction and advice on the use of that equipment.